

AN APPARATUS FOR THE MEASUREMENT OF THE SURFACE
RESISTANCE OF HIGH TEMPERATURE SUPERCONDUCTING THIN
FILMS

By

Robert Knobel

B.Sc. (Honours, Engineering Physics), Queen's University

A THESIS SUBMITTED IN PARTIAL FULFILLMENT OF
THE REQUIREMENTS FOR THE DEGREE OF
MASTER OF SCIENCE

in

THE FACULTY OF GRADUATE STUDIES
Department of PHYSICS

We accept this thesis as conforming
to the required standard

THE UNIVERSITY OF BRITISH COLUMBIA

1995

© Robert Knobel, 1995

In presenting this thesis in partial fulfilment of the requirements for an advanced degree at the University of British Columbia, I agree that the Library shall make it freely available for reference and study. I further agree that permission for extensive copying of this thesis for scholarly purposes may be granted by the head of my department or by his or her representatives. It is understood that copying or publication of this thesis for financial gain shall not be allowed without my written permission.

Department of Physics

The University of British Columbia
Vancouver, Canada

Date June 19 / 95

Abstract

An apparatus to measure the millimeter-wave surface resistance of thin films of high temperature superconductors has been built. The apparatus consists of a flow cryostat, an open resonator and a swept-frequency millimeter-wave source/detector pair.

The flow cryostat is used to cool the experiment to cryogenic temperatures (either 2 K with liquid helium, or 70 K with liquid nitrogen), while keeping a very short distance between the experiment and room temperature. The cryogenic fluid is drawn through the cryostat, and circulates through heat exchangers, absorbing incident heat.

The open resonator allows sensitive measurement of the surface resistance of the film at high frequency. The resonator built operates at 117 GHz, and has a Q for copper at 77 K of 39000. The millimeter-wave source and detector are taken from a fixed frequency apparatus, and were modified to provide a frequency sweep capability. The source and detector operate in a band between 116.8 and 117.6 GHz.

Measurements were performed on both metallic and superconducting samples. The metallic samples were used as calibration of the geometric factors of the resonator, in order to extract the value of the surface resistance. Four thin films of high temperature superconductors were measured, as a demonstration of the capabilities of the apparatus.

Table of Contents

Abstract	ii
List of Tables	vi
List of Figures	vii
Acknowledgement	ix
1 Introduction	1
1.1 Surface Impedance	3
1.2 Electrodynamics of Superconductors	6
1.3 Motivation	9
2 The Flow Cryostat	14
2.1 Introduction	14
2.2 Cryogenic Theory	17
2.3 Design	21
3 Theory of the Open Resonator	33
3.1 Introduction	33
3.2 History	33
3.3 Beam-Wave Theory	35
3.4 Cavity Losses	39
3.5 Beyond the Beam-Wave Theory	46

4	Millimeter-Wave System	50
4.1	Introduction	50
4.2	Millimeter-Wave System	50
4.3	Resonator Design	54
4.4	Coupling	56
4.5	Microwave measurements	59
5	Experimental Method	62
5.1	Introduction	62
5.2	Metallic Samples	63
5.3	Measurement Procedure	64
6	Data	76
6.1	Introduction	76
6.2	Data	77
6.2.1	Furukawa Electric $\text{Bi}_2\text{Sr}_2\text{Ca}_1\text{Cu}_2\text{O}_8$ Thick Film	77
6.2.2	U.B.C. $\text{YBa}_2\text{Cu}_3\text{O}_7$ film on LaAlO_3	79
6.2.3	U.B.C. $\text{YBa}_2\text{Cu}_3\text{O}_7$ film on SrTiO_3	80
6.2.4	McMaster $\text{YBa}_2\text{Cu}_3\text{O}_{7-\delta}$ 10000Å film on LaAlO_3	81
6.2.5	Comparison	84
6.3	Finite Thickness Effects	86
7	Conclusions and Discussion	91
7.1	Introduction	91
7.2	Equipment Performance	91
7.3	Surface Resistance Data	92
7.4	Future Work	93

List of Tables

2.1	Heats and temperatures for the numerical model of the final flow cryostat design. The flow of liquid helium is 0.5 L/hr, and the pressure is 0.1 atm.	29
5.1	Fitting parameters for various functions	73

List of Figures

2.1	Photograph of the flow cryostat	15
2.2	Photograph of the flow cryostat with shields removed	16
2.3	Schematic cut-away drawing of the flow cryostat.	20
2.4	Isometric cut-away drawing of the flow cryostat.	23
2.5	Heat conduction as a function of inner pipe length	25
2.6	Temperatures as functions of inner pipe length	26
2.7	Heat conduction as a function of outer pipe length	27
2.8	Temperatures as functions of outer pipe lengths	27
2.9	Temperature of inner pipes in final model	29
2.10	Temperature of gas in the exchanger in the final model	30
2.11	Temperature of gas in the outer pipes in the final model	30
3.1	Terminology and geometry of open resonators.	34
3.2	The semi-planar hemispherical geometry of the open resonator as used in the experiment.	38
3.3	Field amplitude numerical simulation	40
3.4	Relative intensities of the cartesian components of the electric field in the complex point-source theory	48
4.1	Block diagram of the millimeter-wave system	51
4.2	Schematic diagram of waveguide circuit	53
4.3	The design of the resonator and sample positioning apparatus	55
4.4	Mode chart for the resonator as built	57

4.5	Numerical simulation of Q for copper at 77K	58
4.6	Numerical simulation of the resonator Q as a function of sample loss . . .	59
4.7	Lumped-element equivalent circuit of a resonator connected between a generator and a detector.	60
5.1	Surface resistance of copper at 117 GHz calculated from d.c. resistivity data	64
5.2	Comparison of the detected signal amplitude for direct transmission (<i>ie.</i> no resonator) for standard flanges and choke flanges.	67
5.3	Q vs. temperature for brass and copper.	69
5.4	Resonant frequency as a function of temperature for brass and copper. .	70
5.5	Fitting of resonant peak	71
5.6	Fitted residuals for a sample resonant peak	72
5.7	Q vs. temperature for various fitting functions	74
5.8	R_S of copper and brass at 117 GHz as a function of temperature	75
6.1	Furukawa Electric BSCCO thick film surface resistance	77
6.2	U.B.C. YBCO on LaAlO substrate thin film surface resistance	79
6.3	U.B.C. YBCO on SrTiO substrate thin film surface resistance	81
6.4	McMaster YBCO on LaAlO substrate thin film surface resistance	82
6.5	Comparison of surface resistance measurements on two McMaster films at different frequencies.	83
6.6	Comparison of the surface resistance of superconducting films.	84
6.7	Comparison of the surface resistance of superconducting films from the literature.	89
6.8	Effective surface resistance for infinite substrate	90
6.9	Effective surface resistance for a 1mm thick substrate backed by copper. .	90

Acknowledgement

I would like to thank, first of all, my supervisor Walter Hardy. His guidance and expertise have made this project possible. I'm indebted to him for his patience and advice that have helped me grow as a scientist and a person. I would like to thank as well Doug Bonn, who has been a leader by example in the laboratory as well as a friend. The example of what a scientist should be presented by these two will be a goal to which I will strive.

The high temperature superconductivity group as a whole has helped me immensely, through encouragement, help and by making the lab an enjoyable place in which to work. Thanks go to Dave Morgan, Kuan Zhang and Saeid Kamal who have helped with friendship and scientific insight since I began, and to Chris Bidinosti, André Wong who have helped since they began. Thanks to Dave Baar, Ruixing Liang and Pinder Dosanjh who have shown me the entrepreneurial side of science – encouraging me to open my mind to opportunities. Q.Y. Ma and André Wong are to be thanked for developing the collaboration of film growth and film characterization which is the center of this project.

I am very much indebted to the U.B.C. physics machine shop. The whole staff have helped through advice and conscientious work. I owe a special debt of gratitude to George Babinger, who built most of the cryostat, and provided essential advice for the rest of the project. Thanks to Pinder Dosanjh for great technical help throughout the project, and (with Levi Waldron) for measuring the D.C. resistivity of metals.

I owe a huge thanks to Wendy Braham, whose support and faith in me never failed through the hard times. Thanks to Andrew Hill, who has been a good friend and roommate during the last year. Thanks to my parents and sisters who have always encouraged

me, and, despite the miles apart, I've always counted on them.

Thank you to the Natural Sciences and Engineering Research Council, for the financial support of the PGS scholarship. The U.B.C. physics department also gets my thanks, for financial support through scholarships and teaching assistantships.

Chapter 1

Introduction

In 1986, Bednorz and Müller discovered superconductivity in lanthanum barium copper oxide at 35 K [1]. This discovery opened a new chapter and renewed interest in the study of superconductivity. Kamerlingh Onnes in Leiden discovered the first superconductor, mercury, in 1911 shortly after he developed the techniques of liquifying helium [2]. Many other metals were subsequently found to undergo a transition to superconductivity within a few degrees of absolute zero. The phenomenon has been studied both theoretically and experimentally in the intervening years and was thought to be a well understood phenomenon until the recent discoveries of high temperature superconductivity and other exotic superconductors. The theory of superconductivity developed in 1957 by Bardeen Cooper and Schrieffer [3] (called the BCS theory) has been a remarkable success, both in terms of the intuitive understanding of the mechanism that it imparts, as well as in its predictions of experimental results. This theory, with extensions by many other researchers, explains very well the behaviour of so-called “conventional superconductors” (circularly defined as those materials that are well described by the theories).

The discovery of superconductivity in the LaBaCuO system was soon followed by the discovery of other cuprate compounds with superconducting transition temperatures (T_C) even higher (YBa₂Cu₃O₇ has a T_C of 93 K for example). With T_C 's higher than the boiling point of liquid nitrogen (77 K), the refrigeration needed to achieve superconductivity has become relatively inexpensive, compared to the cost of the liquid helium needed to cool conventional superconductors. This latter requirement has limited the

applications where superconductors can be cost effective. With high temperature superconductors, the possibility exists for many applications which, up until now, have been far too expensive to pursue. It may soon be possible to have magnetically levitated trains, low loss powerlines, and high speed superconducting computers.

However the new cuprate high temperature superconductors are not understood very well, and are difficult to fabricate due to the complicated chemical structure. The simplest method of fabrication, to simply mix and bake the ingredients, is capable of producing a superconductor, but the material is polycrystalline with very poor properties. The materials are brittle ceramics, which cannot be simply drawn to form wires. These material problems have limited the insight into the fundamental properties given by experiments, since many extrinsic effects mask the true intrinsic nature of the superconducting mechanism.

Single crystals of superconductors are being made successfully [4], but are small and difficult to grow. They are currently useful for determining the basic properties of the materials, but not for applications. Most applications of high T_C superconductors use thin films. These are made by depositing layers of the superconducting material (by various methods including sputtering, laser ablation, chemical vapour deposition, etc.) on a dielectric substrate material whose lattice parameters closely match those of the superconducting crystal. These films can be patterned using methods similar to those used in the semiconductor industry, and a variety of devices can be made. These processing methods are becoming very highly developed, and have enabled some very complicated devices to be envisioned. Many different types of transistor are being devised, and SQUID elements for magnetic sensing as well as Josephson junction switching elements have all been produced using thin films of superconducting materials.

Perhaps the most likely prospect for the first commercially successful applications of high T_C superconductors is in passive microwave devices [5]. These filters, delay lines,

interconnects, etc. all can be made to have superior properties if the conductors used have low loss. Good quality high T_C superconducting thin films at 77 K have lower loss than any standard conductor at microwave frequencies [6] (though not zero loss, *cf.* section 1.2). The quantity quoted most often for the electromagnetic loss at microwave frequencies is the surface resistance R_S . This quantity is an effective measure of the “quality” of the film, both in terms of its direct application in microwave use, as well as a general indication of the number of defects in the film (grain boundaries, lattice strain etc.). Such defects are common in films, and must be eliminated through tuning of the many parameters used in film growth.

The purpose of the project described in this thesis is to build an apparatus to measure the surface resistance of films of high temperature superconductors. Such measurements are very commonly made [6], and have been made in this laboratory. However, the plan for this project is to have a device which is particularly suitable for thin films, and allows rapid, non-destructive testing for film-growth optimization.

1.1 Surface Impedance

The concept of surface impedance is important for normal metals as well as superconductors. It will be instructive to outline where this quantity comes from in both cases. The microwave loss in the best normal metals and the best high temperature superconductors (at 77 K) is about the same at 100 GHz — though the mechanism is quite different. In this section I will define the concept and look at normal metals.

Consider a good conductor for which Ohm’s law applies (this derivation follows that in [7]):

$$\mathbf{J} = \sigma \mathbf{E}. \tag{1.1}$$

We can use Maxwell's equations (assuming harmonic time variation of the fields $e^{j\omega t}$):

$$\nabla \cdot \mathbf{D} = \rho \quad (1.2)$$

$$\nabla \cdot \mathbf{B} = 0 \quad (1.3)$$

$$\nabla \times \mathbf{E} = -j\omega\mathbf{B} \quad (1.4)$$

$$\nabla \times \mathbf{H} = \mathbf{J} + j\omega\mathbf{D}. \quad (1.5)$$

Inserting equation 1.1 into equation 1.5, we get

$$\nabla \times \mathbf{H} = (\sigma + j\omega\epsilon)\mathbf{E}. \quad (1.6)$$

Equations 1.3 and 1.1 imply $\rho = 0$. If we can neglect the displacement current ($\sigma \gg \omega\epsilon$, which is a good approximation up to optical frequencies in metals), then we can write (in various ways):

$$\nabla^2 \mathbf{E} = j\omega\mu\sigma\mathbf{E} \quad (1.7)$$

$$\nabla^2 \mathbf{H} = j\omega\mu\sigma\mathbf{H} \quad (1.8)$$

or

$$\nabla^2 \mathbf{J} = j\omega\mu\sigma\mathbf{J}. \quad (1.9)$$

The solutions to these equations depend on the particular boundary conditions, the simplest of which is to consider a semi-infinite slab of conductor of infinite depth ($z > 0$). This case, though artificial, is actually very important because at high frequencies most bodies are much larger than the depth of penetration of the electromagnetic fields. For a uniform field pointing along the plane of the conductor (say in the x direction), the differential equation becomes:

$$\frac{d^2 E_x}{dz^2} = j\omega\mu\sigma E_x = \beta^2 E_x \quad (1.10)$$

Which has the general solution

$$E_x = C_1 e^{-\beta z} + C_2 e^{\beta z} \quad (1.11)$$

Where the propagation constant β is most often written as

$$\beta = \frac{1+j}{\delta} \quad (1.12)$$

$$\delta = \sqrt{\frac{2}{\omega\mu\sigma}}. \quad (1.13)$$

For E_x to remain finite as $z \rightarrow \infty$, $C_2 = 0$. Writing C_1 as E_0 , the field at $z = 0$, we can write:

$$E_x = E_0 e^{-\beta z} = E_0 e^{-z/\delta} e^{-jz/\delta} \quad (1.14)$$

with similar equations for both the magnetic field H and current density J . The quantity δ is the *skin depth* in the material, and is in general a complex quantity (since σ is a complex quantity). However, in a normal metal the real part of the conductivity dominates at millimeter-wave frequencies, and thus δ is, to a very good approximation, real. The value of δ is the depth at which the fields have decayed to $1/e$ their value at the surface. This description is valid, and the quantity of the skin depth is appropriate, for the situations where: $\sigma \gg \omega\epsilon$; where the dimensions of the sample are large in comparison to the skin depth; and where the mean free path of the electrons in the conductor is short in comparison to the skin depth (*cf.* chapter 5).

The total amount of current carried in such a semi-infinite conductor (of unit width) is given by integrating the current density (given by the equivalent equation to 1.14):

$$I_x = \int_0^\infty J_x dz = \int_0^\infty J_0 e^{-(1+j)(z/\delta)} dz = \frac{J_0 \delta}{1+j}. \quad (1.15)$$

The *surface impedance* Z_S is defined as the ratio of the electric field on the surface to the current carried in the conductor (here for unit width):

$$Z_S = \frac{E_{x0}}{I_x} = \frac{J_0/\sigma}{(J_0 \delta)/(1+j)} = \frac{1+j}{\sigma \delta} \quad (1.16)$$

The surface impedance is often separated into its real and imaginary parts

$$Z_S \equiv R_S + jX_S \quad (1.17)$$

$$= \operatorname{Re} \left(\frac{1+j}{\sigma\delta} \right) + \operatorname{Im} \left(\frac{1+j}{\sigma\delta} \right) \quad (1.18)$$

which, for a normal metal where $\operatorname{Im}(\delta) \approx \operatorname{Im}(\sigma) \approx 0$, gives

$$Z_S = R_S + jX_S \approx \frac{1}{\sigma\delta} + j\frac{1}{\sigma\delta} = \sqrt{\frac{\omega\mu}{2\sigma}} + j\sqrt{\frac{\omega\mu}{2\sigma}} \quad (1.19)$$

where the real part R_S is the *surface resistance* and the imaginary part X_S is called the *surface reactance*. The surface resistance and surface reactance are measured in the same units as resistance (Ohms). The surface impedance measured across two opposing edges of a square is independent of the size of the square. For this reason, the units used for surface reactance and impedance are often Ω/\square , or Ohms per square.

For more general geometry, where the above definition isn't obvious, the surface impedance is defined as [8]

$$\hat{\mathbf{n}} \times \mathbf{E} \equiv Z_S \hat{\mathbf{n}} \times \mathbf{H} \times \hat{\mathbf{n}} \quad (1.20)$$

along a surface with normal $\hat{\mathbf{n}}$, where Z_S will in general be a complex-valued tensor for anisotropic materials (where σ is a tensor). The power dissipated in the conductor is proportional to the surface resistance

$$P = \frac{1}{2} R_S \iint_{\text{Surface}} |\hat{\mathbf{n}} \times \mathbf{H} \times \hat{\mathbf{n}}|^2 dS. \quad (1.21)$$

1.2 Electrodynamics of Superconductors

In this section a brief overview of the electrodynamics of superconductors will be given. This work has been the subject of much effort over the years. For a more complete discussion of particular points, see the references which will be cited throughout the

text. For more complete summaries, see the reviews of Tinkham, Waldram, or Klein ([9][6][10]).

There are a number of theoretical models used to describe the electrodynamic behaviour of superconductors, both microscopic and empirical [11] [12] [13]. The model described here is a “generalized two-fluid model”, based on a number of papers from this lab [14] [15], but the basic idea was originally proposed, in a more specific way, by Gorter and Casimir [16] and by London [17]. The basis of this model is that the conduction electrons in a superconducting material can be thought of as being in two types: the normal electrons and the superconducting electrons. The normal electrons behave like electrons do in a non-superconducting material: dissipating energy by scattering. The superconducting electrons (often referred to as the superfluid) however do not dissipate any energy. The dynamic behaviour of these two electron types can be described through transport equations [18]:

$$m \frac{d\mathbf{J}_n}{dt} + m \frac{\mathbf{J}_n}{\tau} = N_n e^2 \mathbf{E} \quad (1.22)$$

$$m \frac{d\mathbf{J}_s}{dt} = N_s e^2 \mathbf{E} \quad (1.23)$$

where N_n and N_s are the number density of normal and superconducting electrons respectively, τ the scattering time of the normal electrons, and $\mathbf{J}_n = N_n e \mathbf{v}_n$, $\mathbf{J}_s = N_s e \mathbf{v}_s$ are the current densities (for electron drift velocities \mathbf{v}_n and \mathbf{v}_s). The total electron density, $N = N_s + N_n$, is constant. When there is only a d.c. field, the superconducting electrons carry all the current. However, for an a.c. field, the inductive response of the superconducting electrons (caused by their inertia) allows some response by the normal electrons which dissipate energy. The conductivity can be derived from equation 1.22 and 1.23 to be:

$$\sigma = \sigma_n + \sigma_s$$

$$= \frac{N_n e^2 \tau}{m(1 + \omega^2 \tau^2)} - j \left(\frac{N_n e^2 \omega \tau^2}{m(1 + \omega^2 \tau^2)} + \frac{N_s e^2}{m\omega} \right) \quad (1.24)$$

$$\equiv \sigma_1 - j\sigma_2 \quad (1.25)$$

where σ_1 and σ_2 are the real and imaginary parts of the conductivity respectively, and are the fundamental quantities related to theories. The solution of the differential equation for the electric field given in equations 1.10 and 1.11 hold as well for a superconductor as for a normal metal. However, in this case, the approximation of real conductivity is no longer valid. The solution of the equation can thus be written as:

$$E_x = E_0 e^{-\beta z} \quad (1.26)$$

with $\beta = \sqrt{j\omega\mu\sigma}$, as before. Using the separation of the complex conductivity as $\sigma = \sigma_1 - j\sigma_2$, β can be rewritten as:

$$\beta = \sqrt{j\omega\mu\sigma_1 + \omega\mu\sigma_2}. \quad (1.27)$$

The *penetration depth* of a superconductor, λ , is defined through

$$\frac{1}{\lambda^2} \equiv \omega\mu\sigma_2 \equiv \text{Re} \left(\int_0^\infty \frac{H_{\parallel}(z)}{H_{\parallel}(0)} dz \right). \quad (1.28)$$

In a superconductor at millimeter-wave frequencies, $\sigma_2 \gg \sigma_1$ (*ie.* most of the current is carried by the superfluid). Thus the fields at the surface of the superconductor are suppressed over a length scale set by λ . At a depth of λ from the surface, the fields will be $1/e$ their value at the surface.

Thus the values for the surface resistance and reactance may be derived in this two-fluid model as:

$$R_S \approx \frac{1}{2} \omega^2 \mu^2 \sigma_1 \lambda^3 \quad (1.29)$$

$$X_S = \omega\mu\lambda. \quad (1.30)$$

This derivation assumes local electrodynamics, where the penetration depth (scale over which fields change in the material) is much greater than both the mean free path of the electrons, as well as their coherence length [9]. Both of these conditions are well satisfied for high temperature superconductors [6]. The surface resistance R_S is directly proportional to the real part of the conductivity, and to the cube of the penetration depth. The surface reactance is directly proportional to the penetration depth. The temperature dependence of the penetration depth is a very important quantity, since it can be related directly to the fraction of superconducting electrons [18]:

$$x_s = \frac{N_s}{N} = \frac{\lambda^2(0)}{\lambda^2(T)}. \quad (1.31)$$

In terms of practical uses for superconductors in the millimeter-wave regime, an important difference occurs between equations 1.19 and 1.29. For normal metals, the surface resistance increases with frequency according to $\omega^{1/2}$, whereas for superconductors it goes as ω^2 . There is therefore a crossover regime where the losses are comparable for metals and superconductors at the same temperature. For the high temperature superconductors currently used, this crossover frequency (at 77K) is approximately at 100-150 GHz.

1.3 Motivation

There are a number of ways of measuring the surface resistance of a conductor. The most common way of making these measurements is to form a resonant circuit, and measure the width of the resonance in frequency. The Q of the resonance

$$Q = \left(\frac{\text{Resonant frequency}}{\text{Full width at half maximum}} \right) \quad (1.32)$$

is related to the surface resistance of the material forming the resonator (*cf.* chapters 3 and 4).

There are three general ways in which the surface resistance of high temperature superconductors may be measured by resonant techniques:

- patterning a stripline resonator out of thin films of the material.
- creating a resonant cavity where some or all of the body is made from the material.
- inserting a piece of the material into the interior of a resonant cavity.

The first method [19] is of the most practical use, since it most resembles the final form of microwave circuit elements. A thin film of the material deposited on a substrate is patterned into a resonant structure, and the Q of the resonator is evaluated subject to other variables (*ie.* power, temperature, material properties). This is, however, a destructive technique, since the material must be patterned. It is not very useful as a diagnostic tool. As well, it is unclear what effects the patterning has on the materials. It would be better to measure the films non-destructively beforehand.

The third method is the one used most often in this laboratory [14][15][20][18]. Here a cavity resonator is constructed out of a material with low loss (a conventional superconductor such as lead for best results) with an opening through which the sample of interest is inserted. Again, the change in Q with various variables can be measured, giving the surface impedance of the material. This method can be very accurate, since the filling factor can be made quite high with proper choice of resonator geometry [14]. Although it is an appropriate technique for single crystals, it is not generally suitable for thin films. The films must be made of the correct size to fit in the resonator yet give high filling factor — which might mean breaking the film into small pieces. Thin films are grown on substrates whose electromagnetic properties (loss tangent and dielectric constant) will affect the measurement. Finally, at millimeter-wave frequencies, the resonant cavities become very small, and are difficult to fabricate and work with.

The most common way to implement the second method is to replace one wall of a resonant cavity (normally a cylindrical TE_{011} cavity) with a piece of the material ([21] [22] and many others). This is a convenient method, although the results obtained are not very accurate in general. This is because the loss due to the superconductor is only part of the loss in the cavity, and separation of the two terms can be difficult. The superconductor must be in close contact with the rest of the cavity, and so the cavity as a whole must be subject to changes in the same external variable(s) as the film (*ie.* temperature, magnetic field, etc.). The cavity material will have some dependence in its loss with temperature, and will be non-trivially included in the measurement. Forming the cavity body from conventional superconducting material would give no advantage in terms of resolution, since most measurements will be made above the T_C of any conventional superconductor. The film itself must be of the same size as the resonator, and the contact with the resonator may in itself damage the film.

A very successful technique is the parallel plate resonator [23]. This technique has yielded some of the most sensitive measurements of surface resistance around 10 GHz. Here two films of the material are pressed together, separated by a thin teflon sheet. The assembly forms a resonator, whose Q may be measured as a function of temperature. The difficulty with this technique is that two films are required, and their shape is quite important. For film characterization, it is desirable to have a technique not dependent on having two similar films. The objections raised for this method apply as well to dielectric resonators [24][25], where a bulk dielectric crystal forms the body of the resonator.

The method described in this thesis is the *open resonator*. This method is particularly appropriate for the measurement of surface resistance of thin films of high temperature superconductors at millimeter-wave frequencies. It is not a method invented here, it has been described in numerous papers [26] [27] [28], and it was the advantages of this method as described in these papers that first attracted our interest. The open resonator

technique will be described in detail further on in the thesis (*cf.* chapters 3 and 4), but a quick overview will be appropriate here. The open resonator consists of a spherical mirror separated from the sample under test by a distance less than the radius of curvature of the mirror (see figure 2.2). The electromagnetic field is focussed by the mirror on to the sample surface. The resonator is open to the environment, unlike conventional closed cavity resonators, this allows the resonator to be a larger size than would be possible for other geometries. As well, the sample is physically separated from the rest of the resonator, so the temperature of the sample can be varied independently of the rest of the apparatus.

This apparatus is ideally suited for the measurement of thin films because only the top surface is in contact with the electromagnetic field, avoiding dependence on the substrate material. As well there is no dependence on the shape of the superconducting sample (as long as it is larger than some minimum size), accommodating any shape of sample. In fact, the focus of the resonator can be scanned across the surface, giving information on the surface resistance over the area of the sample [28]. Such an apparatus (working at 77 K) is being sold commercially by Conductus[29]. The open resonator is the only method capable of doing this non-destructively.

Though this project has drawn on the ideas of other researchers in terms of using an open resonator, there are problems which have not been dealt with before in this context:

- The frequency used is quite high (117 GHz), involving complicated source and detector techniques (*cf.* chapter 4).
- The samples measured are quite small, forcing the resonator to be used at its limit in terms of spot size (*cf.* chapter 3).
- The temperature dependence is being investigated, and a novel cooling technique has been developed particularly for this apparatus (*cf.* chapter 2).

This thesis describes the development of the apparatus, as well as giving background on the theory. There is some data described, though it is secondary, since no exhaustive study has been done. Without systematic study of thin films under various growth conditions, subject to various variables, the information is more qualitative in nature.

Chapter 2

The Flow Cryostat

2.1 Introduction

The cooling of the experiment becomes problematic when one wishes to use millimeter-waves. At these frequencies, the signal is carried through waveguides, which consist of hollow rectangular tubes. Standard waveguides become quite lossy as the frequency increases, with losses of about 1.5 dB per foot near 100 GHz[30]. As well, the standing waves that arise from discontinuities in the circuit can seriously degrade measurement accuracy, especially for long transmission lines. Thus, one wants to have as short a length of waveguide as possible.

On the other hand, standard cryostats involve the lowering of the experimental apparatus into a long dewar filled with liquid helium. Here the heat conducted along the supports and electrical connections (wires, coaxial cable, waveguides, etc.) is reduced by having long lengths of material with low thermal conductivity. This is exactly the opposite of the ideal millimeter-wave system having short, highly conductive connections.

For this experiment, we have designed a flow cryostat that avoids the long transmission lines (figures 2.1 and 2.2). In this apparatus, cryogenic fluid (liquid helium or liquid nitrogen) is drawn up from a storage dewar and circulated through a series of heat exchangers, thus cooling the experiment. This contrasts with standard immersion cryostats, where the experiment is immersed in a large volume of liquid. The present design allows for a very short length of waveguide (~ 5 cm) to go from room temperature

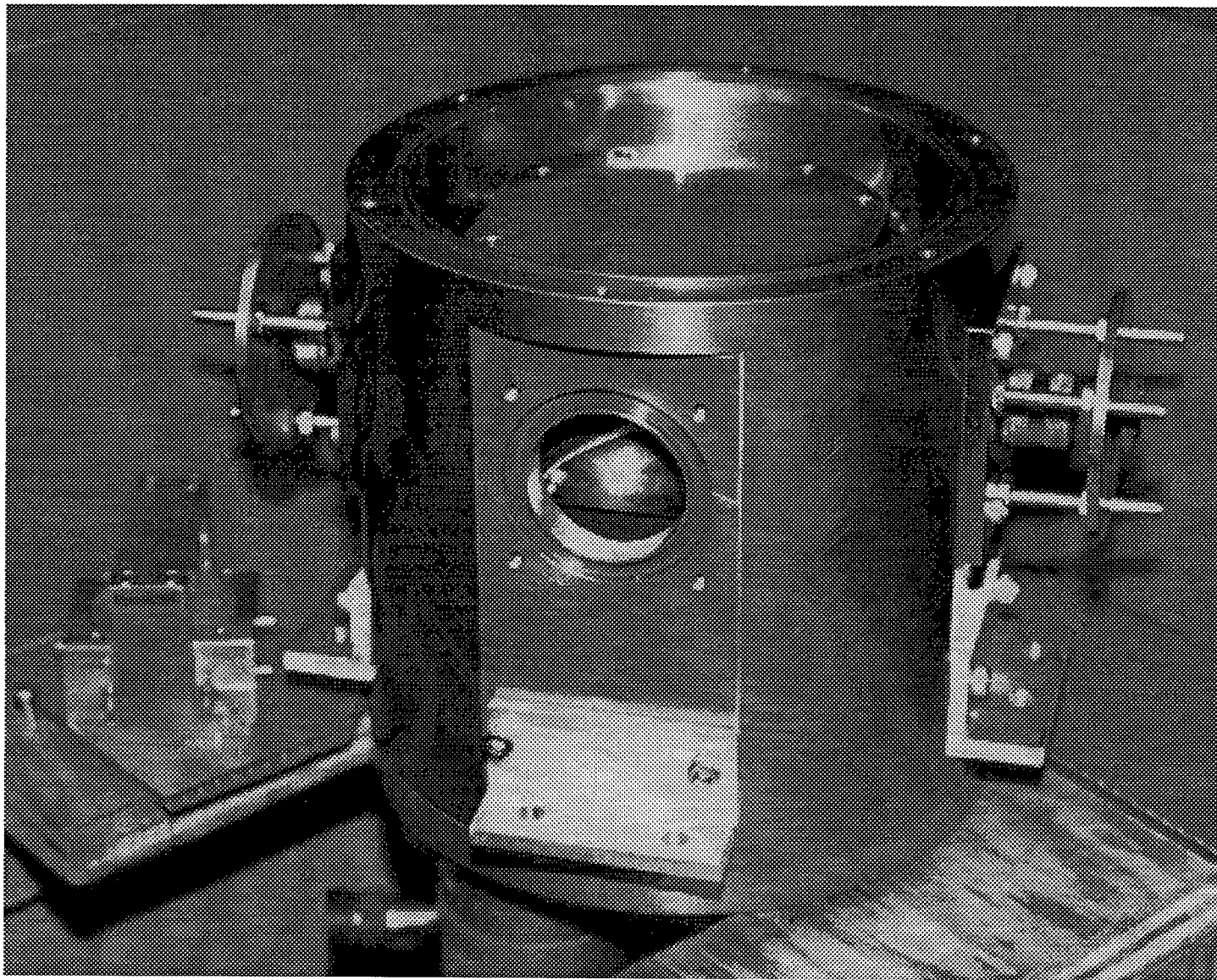


Figure 2.1: The outer view of the flow cryostat. The lid has been removed to show the heat shield. The plates on the sides are for adjusting the *choke flanges* (see chapter 4)

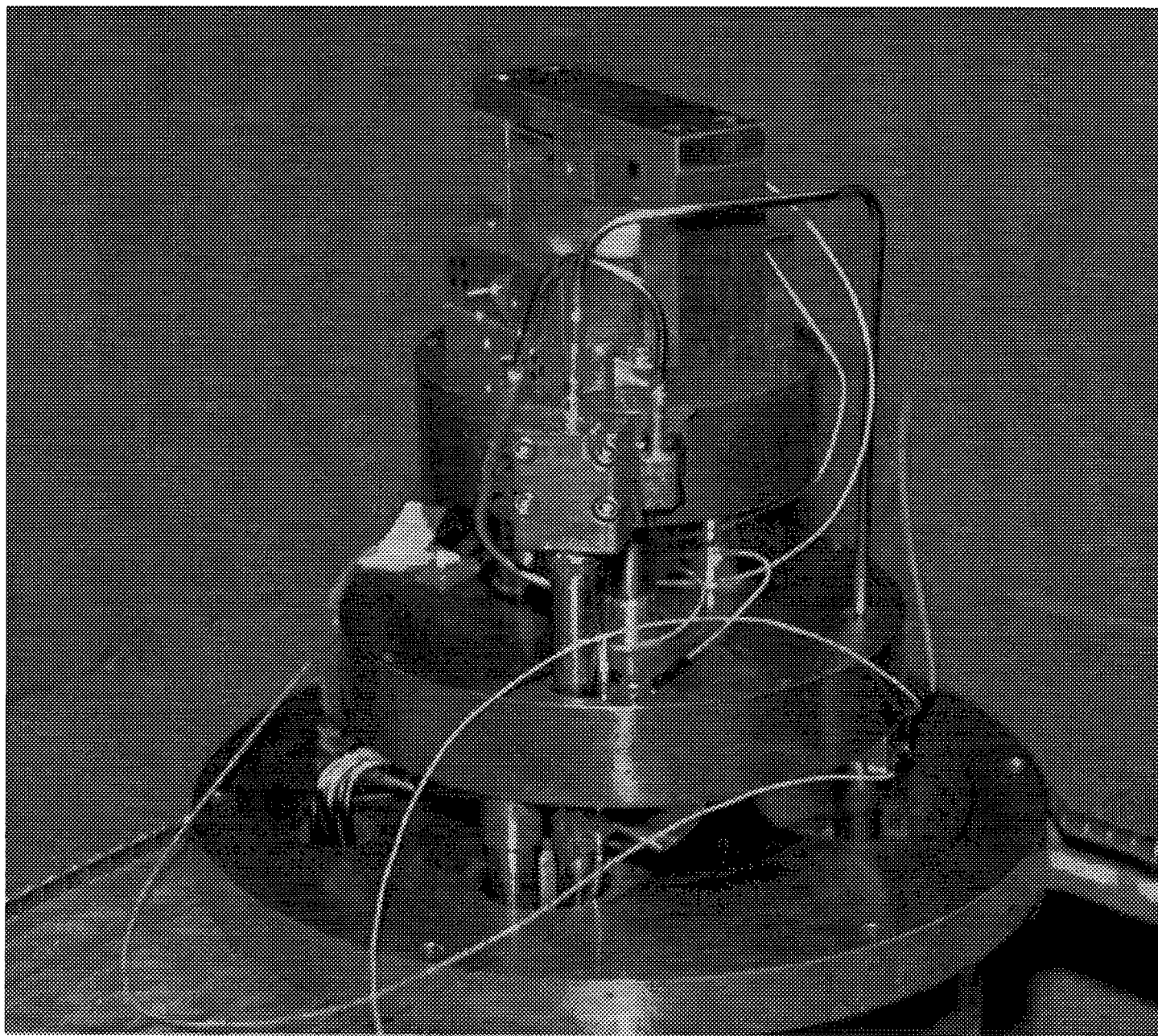


Figure 2.2: The flow cryostat with both the vacuum and heat shields removed. The two heat exchangers are clearly visible, with the resonator and sample-holder attached to the inner one.

to low temperature (~ 2 K with liquid helium, ~ 70 K with liquid nitrogen). As well, it allows rapid thermal cycling of the whole experiment ($\sim 1/2$ day) and can accommodate a variety of experiments. However, unlike the standard cryostat, where many researchers have refined the techniques [31], the design of the flow cryostat requires quite careful study and modeling. In this chapter I outline the basis for the design, and show the theoretical performance of the final setup.

2.2 Cryogenic Theory

In designing a cryostat, it is important to determine how the heat will be transferred to the experimental chamber. For a flow cryostat in an evacuated container, heat can be transferred to the experimental chamber by radiation across the vacuum, or by conduction along the solid materials either used for support of the apparatus, or used in the experiment (*eg.* wires, waveguides, adjusting screws, etc.). By minimizing the heat transfer through both of these mechanisms, the amount of cryogenic fluid needed can be reduced.

The rate at which a surface of area A at temperature T emits thermal radiation \dot{Q} is given by the Stefan-Boltzmann equation [32]:

$$\dot{Q} = \sigma eAT^4. \quad (2.1)$$

The value $\sigma = 5.67 \times 10^{-8} \text{Wm}^{-2}\text{K}^{-4}$ is the Stefan-Boltzmann constant. The emissivity e is the ratio of the radiative energy emitted by an object at temperature T divided by the radiative energy emitted by a black body at the same temperature. It is a simplified model, in which one uses an average of the frequency dependent emissivities that exist in real materials, but should be adequate for the present use. The net rate of radiant energy exchange between surface 1 of area A at temperature T_1 and surface 2 at the (hotter)

temperature T_2 is

$$\dot{Q}_{rad_{21}} = \sigma EA(T_2^4 - T_1^4) \quad (2.2)$$

where E is a factor involving the emissivities of the two surfaces, and depends upon whether the reflections are diffuse or specular. We have polished the surfaces to give specular reflection, since this gives lower transfer of heat. In this case

$$E = \frac{e_1 e_2}{e_2 + (1 - e_2)e_1}. \quad (2.3)$$

For the materials used in this apparatus (aluminum, copper and brass), the emissivities e_1 and e_2 are approximately 0.04–0.06 at room temperature and will decrease with decreasing temperature [32]. Thus $E = 0.025$ will give a conservative estimate for the rate of radiative heat transfer in the design.

To reduce heat transfer by radiation, one can insert radiation shields. By inserting a shield at an intermediate temperature T_s between T_1 and T_2 much of the radiation can be intercepted. This shield may be *floating*, *ie.* thermally disconnected, or actively cooled. Such shielding is very important in the flow cryostat, since the experiment will be surrounded by material at room temperature, not liquid nitrogen temperature as in a standard cryostat.

The rate of heat conduction \dot{Q}_{cond} along a solid material of thermal conductivity k and cross sectional area A with a temperature gradient $\frac{dT}{dx}$ is given by the relation [33]

$$\dot{Q}_{cond} = kA \frac{dT}{dx}. \quad (2.4)$$

By using materials with poor thermal conductivity and small cross-sectional area (*eg.* thin wall stainless steel) this conduction can be reduced. However, the thermal conduction can be further reduced, and perhaps made insignificant, by using the flowing gas to cool the supports. The rate of heat absorption by a warming gas of heat capacity C_p

flowing at a rate of \dot{n} moles/second is

$$d\dot{Q} = \dot{n}C_p dT_{gas} \quad (2.5)$$

or,

$$\frac{d\dot{Q}}{dx} = \dot{n}C_p \frac{dT_{gas}}{dx} \quad (2.6)$$

if one can use distance as the independent variable (as in gas traveling along a pipe). The approximation that C_p is constant with temperature will be used without significant reduction in accuracy.

Heat is transferred between the wall of the containing vessel and the gas it contains with a temperature difference of ΔT over an area \mathcal{A} according to

$$\dot{Q} = h\Delta T\mathcal{A}. \quad (2.7)$$

The value heat transfer coefficient, h , depends upon whether the flow of fluid is laminar or turbulent. The turbulence of a flow of fluid at velocity v with viscosity η and density ρ through a pipe of diameter d is described by a dimensionless quantity called the *Reynolds number* Re :

$$Re = \frac{\rho v d}{\eta}. \quad (2.8)$$

A flow with Reynolds number above 2300 is turbulent. For laminar flow, the heat transfer coefficient for a fluid of thermal conductivity k_{gas} is given by [34]:

$$h \propto k_{gas}/d. \quad (2.9)$$

For turbulent flow [35]

$$h \propto \frac{C_p G^{0.8} \eta^{0.2}}{(Pr)^{0.6} d^{0.2}}. \quad (2.10)$$

where the dimensionless Prandtl number is $Pr = \frac{\eta C_p}{k_{gas}}$ and $G = v\rho$.

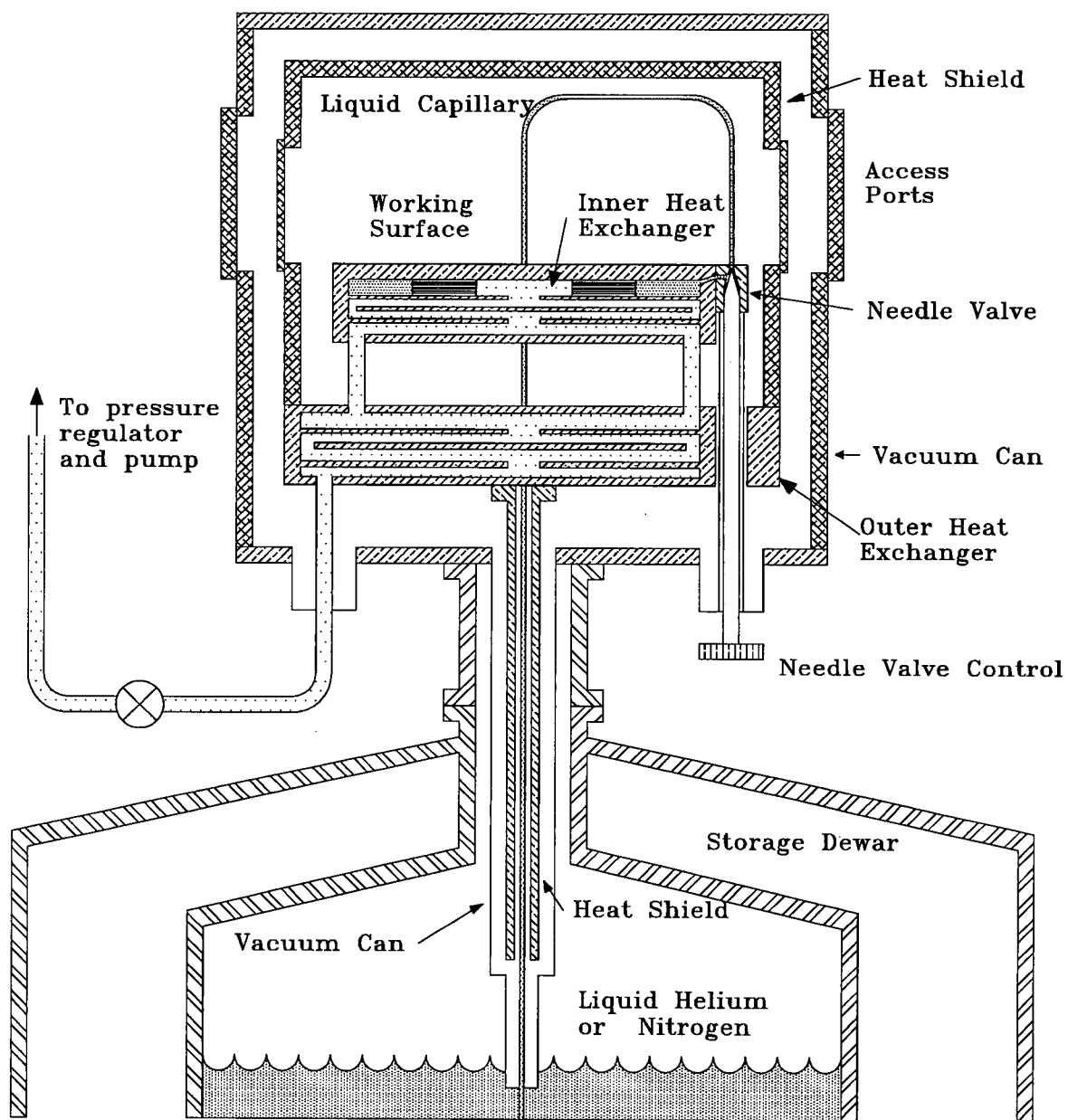


Figure 2.3: Schematic cut-away drawing of the flow cryostat.

2.3 Design

As described earlier, the flow cryostat, instead of using a large reservoir of cryogenic liquid surrounding the experiment, draws a small constant flow from a separate storage dewar. This flow of liquid, which rapidly becomes gas, is brought through a series of heat exchangers, absorbing incident heat through both the latent heat and the heat capacity of the gas. The chief advantage of this design is that it allows short distances from the cryogenic region to the outside. With a standard cryostat, this is difficult, and would contribute a large heat conduction path.

Extending into the storage dewar is a small capillary (of thin wall stainless steel) which enters into the flow cryostat (see figure 2.3). Cryogenic liquid is drawn up this line and enters a heat exchanger through the control of a needle valve. The heat exchanger consists of a hollow copper block, with copper plates arranged inside so that the fluid must take a circuitous path. Upon entering this chamber, the liquid boils — at the equilibrium temperature for the pressure set. By lowering the pressure (increasing the pumping rate on the gas lines), the temperature at which the liquid boils can be lowered. This temperature becomes the temperature of the experiment, since the experimental apparatus is attached to the top of this heat exchanger. It is important that as much of the liquid changes to gas here as possible, since small droplets of liquid are not as efficient in heat transfer as is the gas. To accomplish this, a finely corrugated disk of copper is inserted into the first stage of the exchanger, ensuring very good thermal contact immediately.

The gas, upon leaving the inner exchanger, is carried through three thin wall stainless steel tubes to another, larger exchanger (see figure 2.4). This heat exchanger, which works in a manner very similar to the first one, is connected to a radiative heat shield surrounding both the experiment and the inner exchanger. By cooling this exchanger with

the flowing gas, the radiative heat load on the experiment is reduced. As a compromise between simplicity of design and efficiency, it was decided to use only two heat exchangers (and one heat shield). The gas leaving the exchanger is carried through three more thin-wall stainless steel tubes, exiting the vacuum shield through ports on the underside. These tubes physically support the experiment, and since they conduct gas, give a reduced conductive heat load to the apparatus.

The base temperature of the experiment is controlled through two variables: the pumping rate on the exit tubes, and the flow impedance provided by the needle valve at the inner exchanger. By tuning these two variables, we attempt to minimize the amount of coolant required. This is of course dependent upon proper design of the heat exchangers and connecting tubes.

The flow cryostat was designed to be used with liquid helium as the coolant. However all of the work described in this thesis uses liquid nitrogen as the coolant. The design was based on the assumption of liquid helium both because it is quite expensive and because its low boiling temperature imposes more stringent design criteria. Liquid nitrogen, though it has different properties and thus the cryostat will not operate at peak efficiency, is relatively cheap.

Thus the design criteria for the flow cryostat are:

- It should have the ability to reach 2 K with 1 L/hr of liquid He flow.
- The experimental chamber should have a minimum volume of approximately 7cm diameter by 5cm high.
- The experimental chamber should have the ability to accommodate various experiments.
- The flow cryostat should work on top of a storage dewar (either liquid helium or

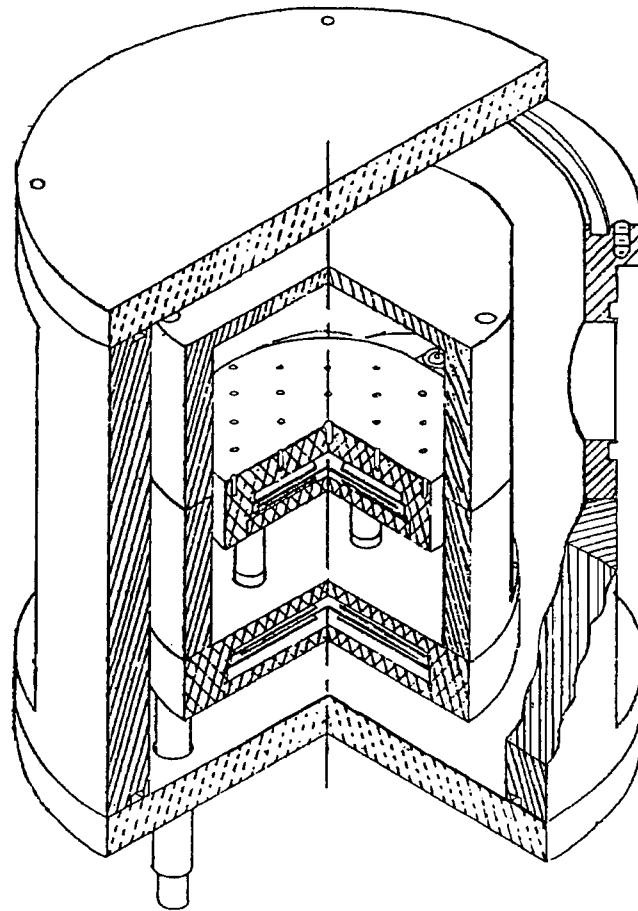


Figure 2.4: Isometric cut-away drawing of the flow cryostat.

liquid nitrogen).

- There should be only a short distance from room temperature to cryogenic temperature.

Computer modeling was used to determine the design of the cryostat. Initially, each portion of the design was examined separately, with assumed values for important parameters. Once the design was set (which was affected at least as much by utility and ease of fabrication as it was by efficiency of the design), a complete simulation was used to check the performance. Conservative values were used initially for the design, since it is difficult to predict what sort of experimental apparatus might eventually be used in this cryostat.

The modeling was done by numerically solving the coupled differential equations describing the flow of the gas, and the heat exchange associated with the gas. For the flow of gas through the pipes (between the exchangers and exiting the apparatus), the temperature of the two ends of the pipes, as well as the initial temperature of the gas, were assumed. The differential equations were integrated using a Runge-Kutta method until the computed final temperature of the pipe matched the set final temperature (essentially a “shooting method”[36]). The flow was assumed to be turbulent, and any pressure change along the length of the pipe was ignored (after assuring that both assumptions were justified). The heat capacity of the gas was assumed constant, and the heat exchange between the gas and the pipe was taken from equation 2.10.

In figures 2.5 and 2.6, the dependence of the heat conduction and temperature of the gas *vs.* the length of pipe connecting the two heat exchangers is shown. As can be clearly seen, the amount of heat transported down the pipes drops off strongly as the length is increased. It was decided that a length of 2–3 cm was sufficient to make the heat load along these pipes negligible. Similarly, in figures 2.7 and 2.8, the dependence on the length of pipes exiting the heat exchanger is shown. Here, any length of pipe longer than 5 cm gives essentially zero heat conducted to the outer exchanger. In fact, even at 5 cm, the heat load along the exit pipes should be even smaller than calculated here. This is due to fact that the outer tube temperature is much less than the assumed 300 K, and in fact becomes frosted with ice, even with a moderate flow rate.

The design of the heat exchangers involves maximizing the heat transfer between the gas and the body without imposing too large a pressure gradient. To increase the heat transfer, the surface area to which the gas is exposed should be maximized. The heat exchangers use plates of copper within a copper block to cause a circuitous flow: the first plate has a hole in the center; the next plate has no hole in the center but has a gap at its outside edge (see figure 2.3). This sequence is repeated, and provides a large increase

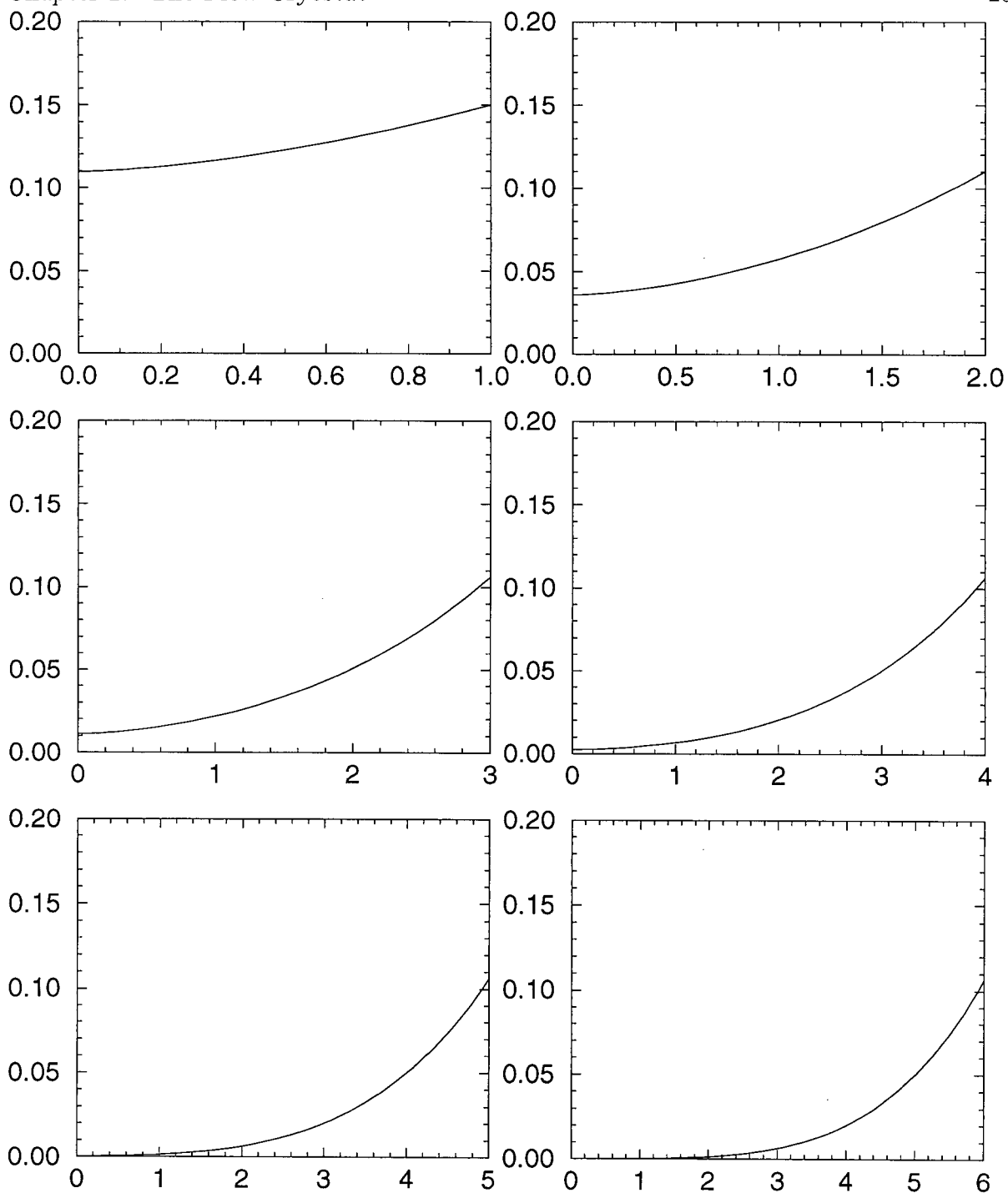


Figure 2.5: Heat conducted (in Watts) along the pipes joining the inner heat exchanger with the outer heat exchanger, as a function of the length of pipes (in cm). The 3 pipes are assumed to be 3/8" diameter, .012" wall thickness stainless steel. The inner exchanger temperature is assumed to be 4.2 K, and the outer exchanger temperature 30 K. The gas flow is set to be that corresponding to a flow of 1 L/hr of liquid helium.

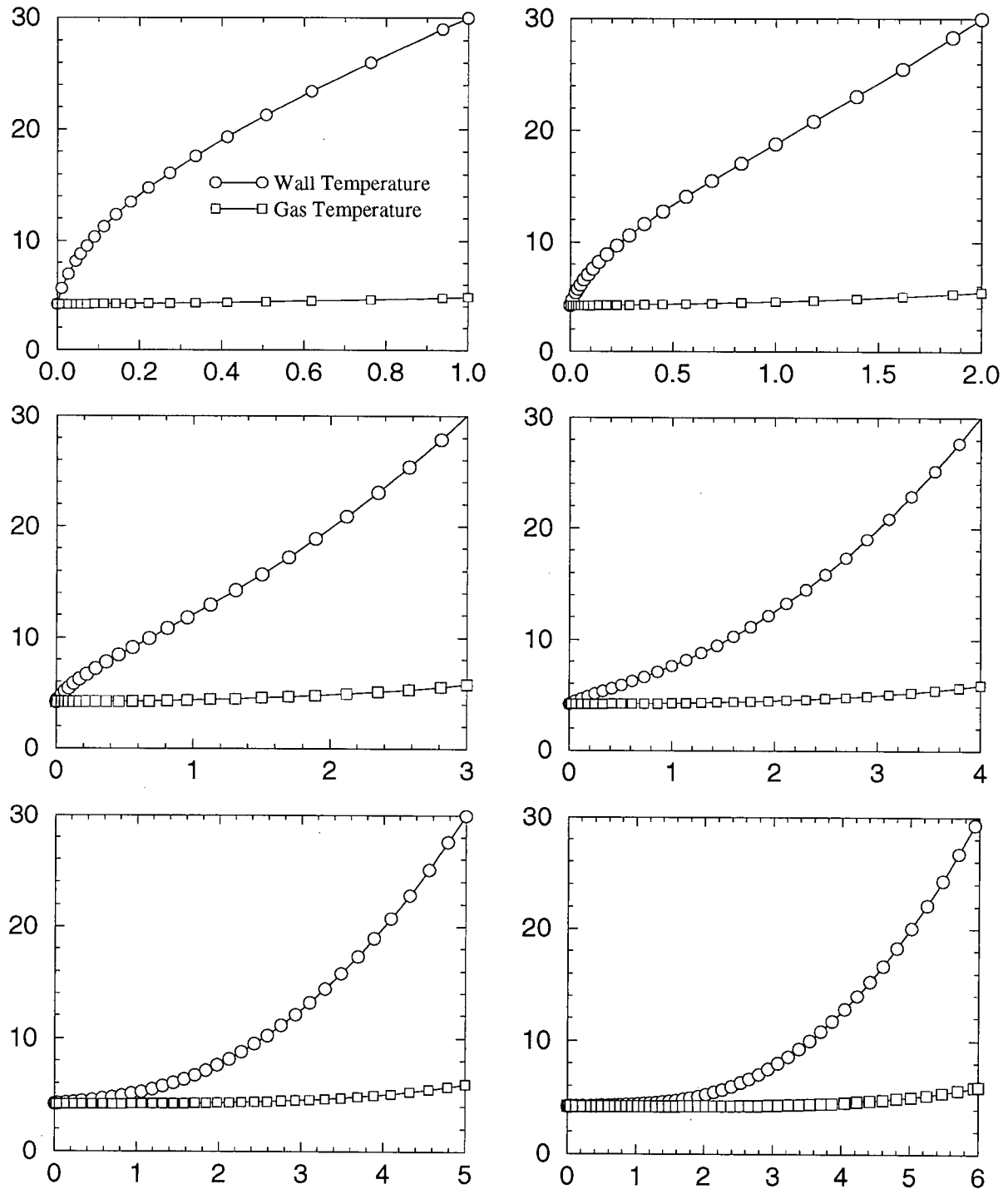


Figure 2.6: Temperature of the helium gas and the pipe wall in Kelvin as a function of pipe length in cm. All parameters are as assumed in the previous figure.

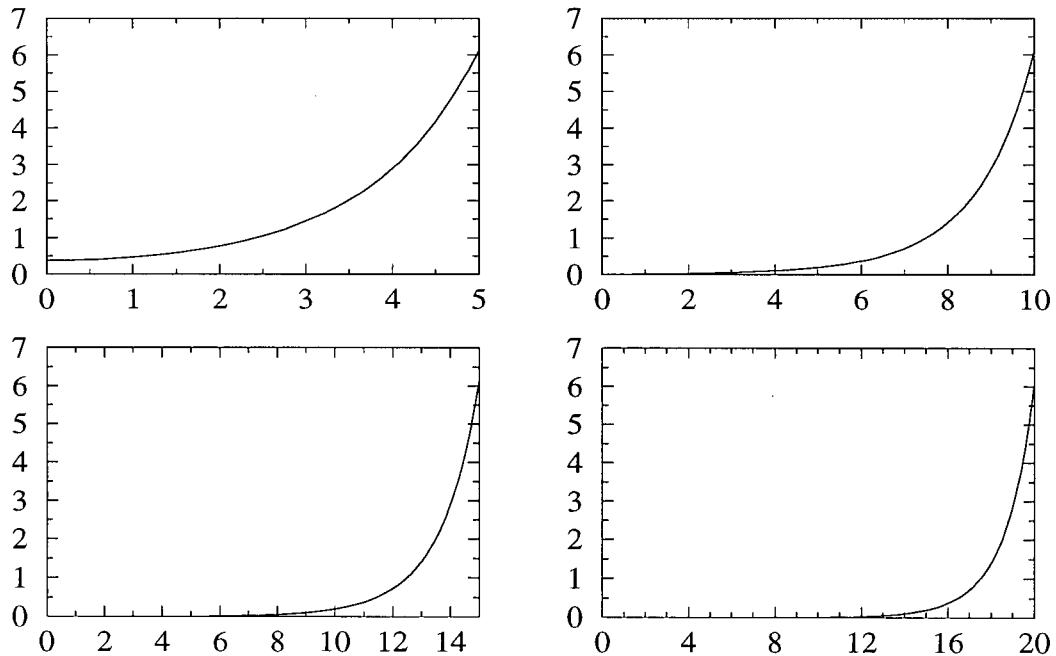


Figure 2.7: Heat conducted (in Watts) along the pipes joining the outer heat exchanger with the vacuum shield, as a function of the length of pipes. The 3 pipes are assumed to be 3/8" diameter, .012" wall thickness stainless steel. The heat exchanger temperature is assumed to be 30 K, and the outside temperature to be 300 K. The gas flow is set at 1 L/hr of liquid helium, starting at 30 K.

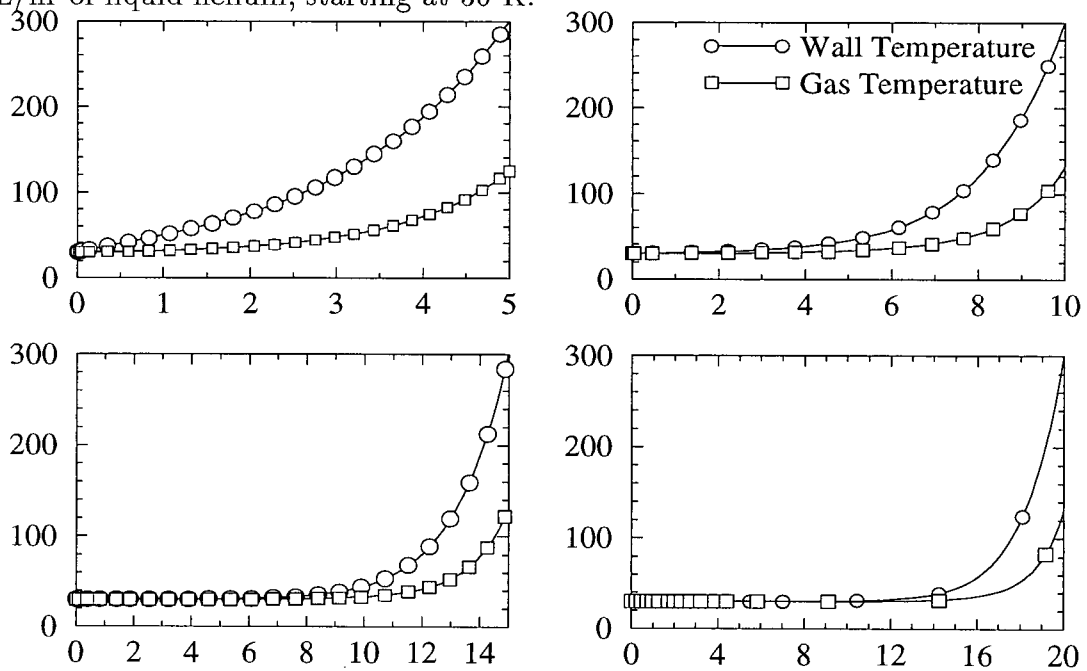


Figure 2.8: Temperature of the helium gas and the pipe wall as a function of pipe length. All parameters are as assumed in the previous figure.

in gas contact area over a simple pipe. Modeling of the heat exchangers proved to be simpler than for pipes, in that the thermal conductivity of copper is so high that even .020" thick copper plates are essentially a thermal "short" to the heat flows encountered.

Thus the problem reduces to determining the best design for the gas to absorb the required amount of heat while passing through a constant temperature body, which involves integrating a set of coupled differential equations. Unlike the pipe problem, there is no fixed end-point that must be satisfied, so no "shooting method" is required. The heat absorbed is maximized by having turbulent flow of the gas which is accomplished by throttling the gas at the plates. As well, the pressure must not drop significantly through the exchanger or we will not have good control over the temperature at the interior of the cryostat. In the end, it was determined that having three plates in the exchangers, separated by approximately 1/10" gives negligible pressure drop, and allows the gas to reach thermal equilibrium with the exchanger body before exiting (see figure 2.10). Note that a number of simplifying assumptions have been made here chiefly in terms of assuming symmetric geometry, and uniform turbulent flow.

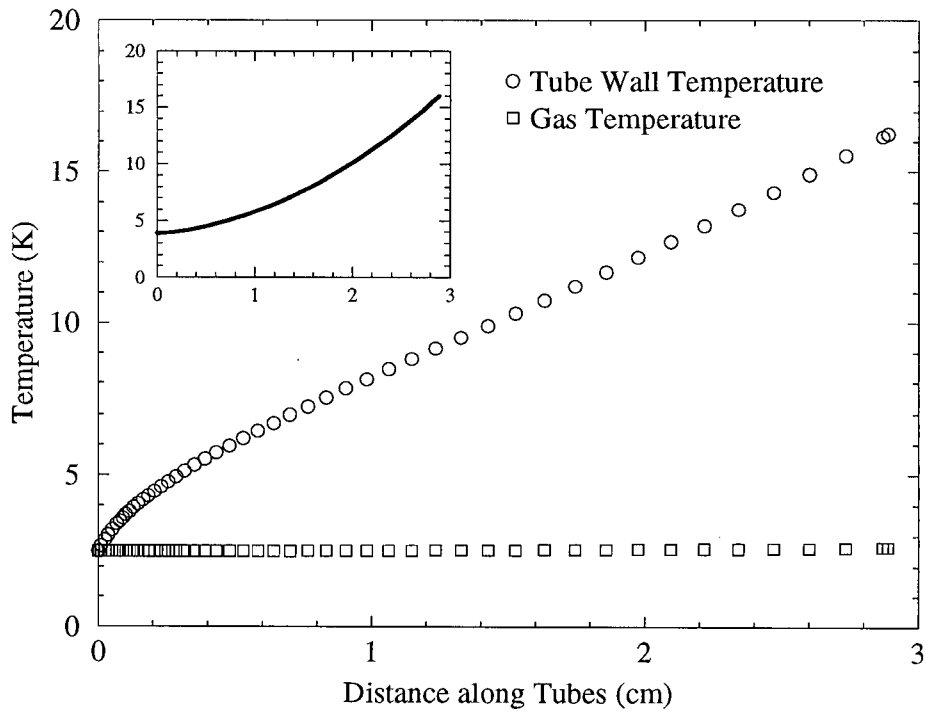


Figure 2.9: Temperature of gas and pipe for the inner pipes of the flow cryostat in a self-consistent numerical model. The pressure is 0.1 atm, and the flow rate 0.5 L/hr of liquid nitrogen. The inset shows the amount of heat (in mW) flowing along the pipes.

Temperatures	Inner exchanger	2.488 K
	Heat Shield	16.263 K
	Gas at inner exch.	2.488 K
	Gas at end of inner pipe	2.618 K
	Gas at beg. of outer pipe	16.262 K
	Gas at exit	39.985 K
Heats	Radiation on inner chamber	$9.7 \cdot 10^{-7}$ W
	Conduction to inner exch.	0.00961 W
	Radiation on shield	0.586 W
	Conduction to shield	0.709 W
	Absorption in inner exch.	0.00961 W
	Absorption in outer exch.	1.273 W

Table 2.1: Heats and temperatures for the numerical model of the final flow cryostat design. The flow of liquid helium is 0.5 L/hr, and the pressure is 0.1 atm.

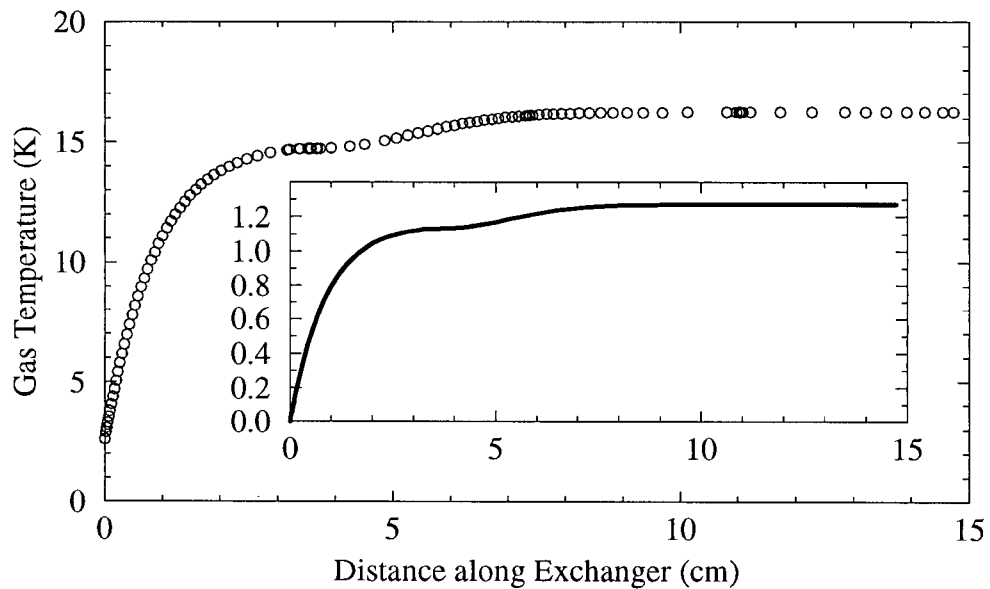


Figure 2.10: Temperature of the gas in the outer exchanger of the final design of the flow cryostat for pressure of 0.1 atm and flow rate of 0.5 L/hr, along the circuitous path inside the exchanger. The shield temperature reaches an equilibrium temperature of 16.26 K. The inset shows the integral of the heat absorbed by the gas (in W).

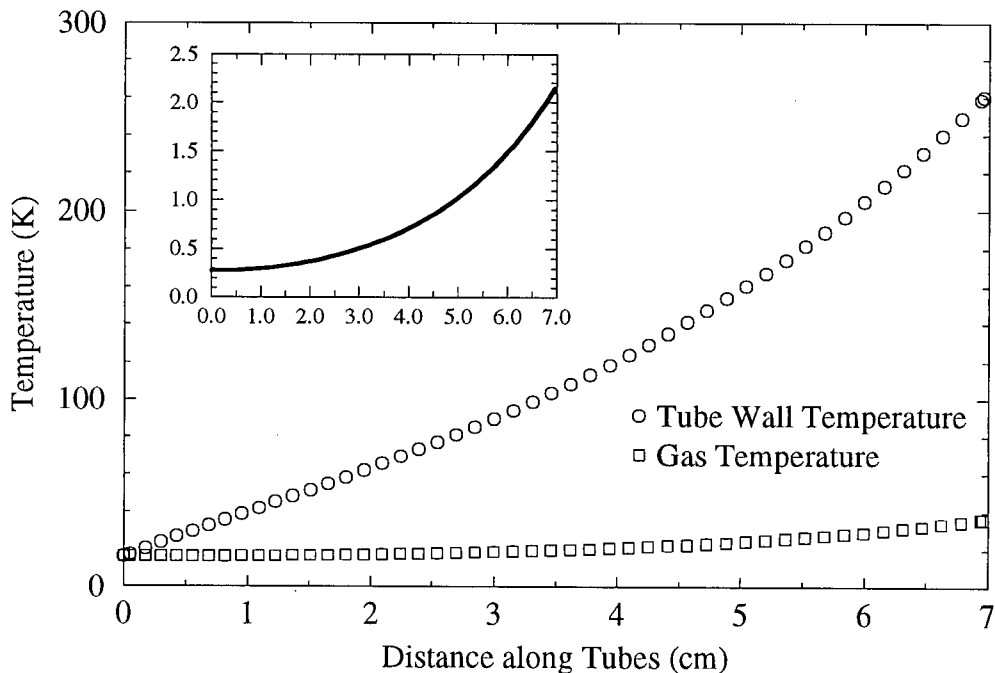


Figure 2.11: Temperature of the gas and pipe for the outer pipes of the flow cryostat in its final configuration. The inset shows the amount of heat conducted along the pipe (in W). See the previous two figures.

The final design of the cryostat is shown in the figures. The full performance of the set design was modeled in a self-consistent solution for various flow rates and pressures (figures 2.9 to 2.11 show a particular set of parameters). This modeling entailed setting the flow rate of liquid, pressure of the exit gas, and external temperature; unlike for the initial models, where each aspect of the cryostat was examined independently. The solution of these coupled differential equations was done iteratively, ending when a self-consistent solution was found. For the condition shown in the figures, 0.5 L/hr of liquid helium flow at 0.1 atm, the latent heat of the liquid is greater than the amount of heat incident on the inner exchanger, meaning that not all the liquid boils before leaving the exchanger. This neglects the heat conduction along waveguides, etc., and thus is an underestimate of the temperatures reached in various portions of the cryostat. To partially account for this, it was assumed that any remaining liquid is transformed into gas by the excess heat (a crude approximation).

As can be seen from figure 2.11, the exiting gas is still very cold (about 50 K). This suggests two things: first of all, that a slower flow of gas could probably be used. This is true up to the limit that the inner heat exchanger should reach a low enough temperature (as determined by the needs of the experiment). Secondly, that one would probably want to use another heat exchanger/heat shield combination. These exchangers are (theoretically) very efficient, as can be seen from figure 2.10, where the gas reaches equilibrium quite well. Unfortunately, another level in the cryostat would entail greater complication in both the use and fabrication of the apparatus, and was not included in the design for that reason.

The modeling done in this chapter has been solely for the steady state — once the experiment has reached operating temperature. In fact, a significant amount of cryogenic liquid would be needed to cool the apparatus to the operating point. For this reason, it is expected that in practice the cryostat will be pre-cooled with liquid nitrogen before

the liquid helium cooling is begun.

Chapter 3

Theory of the Open Resonator

3.1 Introduction

Unlike closed cavity resonators, which have been a key tool for microwave engineers and physicists for decades, open resonators have been exploited only relatively recently. While closed resonators can be regarded as an extension to higher frequency of lumped element RLC circuits, open resonators resemble more a scaling down in frequency of optical mirrors. In this chapter I will outline the theory pertaining to the existence and characteristics of stable resonant modes of such structures.

3.2 History

In the late 1950's, *Fabry-Perot* structures were shown to be useful as resonators at optical frequencies for use in lasers. The Fabry-Perot resonator consists of a pair of plane-parallel mirrors facing each other, between which light reflects over several passes, storing electromagnetic energy. These structures, initially analysed using optical techniques, were later studied in terms of the resonant modes of the electromagnetic field [37].

In related work, Goubau and Schwering showed that an electromagnetic field can be described in terms of a complete set of cylindrical waves. If these waves are propagating largely along one axis, then they can be resolved into an elementary set of beams. These beams can be confined along the axis through a repeated series of guiding structures (ie. lenses).[38]

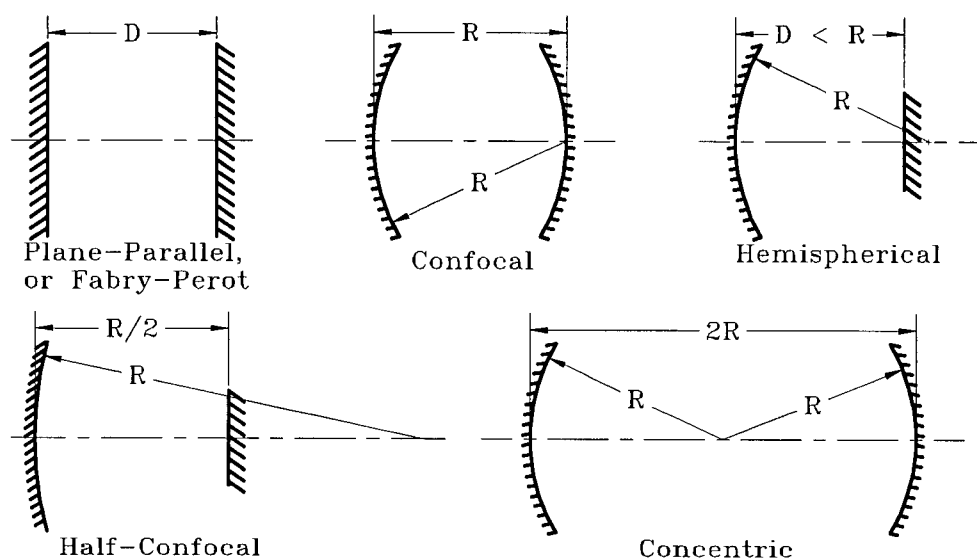


Figure 3.1: Terminology and geometry of open resonators.

Boyd and Gordon[39] developed the *confocal* resonator, in which the plane parallel mirrors are replaced by spherical mirrors separated by their common radius of curvature (figure 3.1). This geometry has the advantage of requiring less precision in the positioning and machining of the reflectors to give low loss. As well, the losses due to diffraction are significantly minimized. Subsequent work generalized the solutions to reflectors of different radius of curvature, and an arbitrary separation. In an important review paper, Kogelnik and Li[40] reviewed the properties of such resonators, incorporating the beam-wave theory of Goubau and Schwering. I will mainly follow their development of the theory in this chapter. As well, I will make use of the work of Bucci and Di Massa[8] who use the eigenvalue approach of Kurokawa[41].

These methods all involve approximations which may not be valid for the experiment described in this thesis. Cullen and coworkers, in a series of papers[42] [43] [44], have attempted to determine the accuracy of these approximations, as well as to develop a more precise theory. These aspects will be described later in this chapter.

3.3 Beam-Wave Theory

The behaviour of the electric and magnetic fields in a resonator can be obtained by solving the wave equation for the magnetic field \mathbf{H} or the electric field \mathbf{E}

$$\nabla^2 \mathbf{H} + k^2 \mathbf{H} = 0 \quad (3.1)$$

$$\nabla^2 \mathbf{E} + k^2 \mathbf{E} = 0 \quad (3.2)$$

subject to the particular boundary conditions of the problem. Here $k = 2\pi/\lambda$ is the propagation constant for wavelength λ in the medium, and is the eigenvalue of the differential equation. The field components in cartesian coordinates of such a coherent wave satisfy the scalar wave equation

$$\nabla^2 u + k^2 u = 0. \quad (3.3)$$

For a wave traveling in the positive z direction, with a harmonic time dependence, we can put

$$u(x, y, z) = \psi(x, y, z) e^{-jkz} e^{j\omega t} \quad (3.4)$$

where the function $\psi(x, y, z)$ represents all deviations from a plane wave. Substituting equation 3.4 in equation 3.3, we get

$$\frac{\partial^2 \psi}{\partial x^2} + \frac{\partial^2 \psi}{\partial y^2} + \frac{\partial^2 \psi}{\partial z^2} - 2jk \frac{\partial \psi}{\partial z} = 0. \quad (3.5)$$

If most of the variation of u with z is taken up by the exponential, ie. ψ is slowly varying in the z direction then we can neglect $\frac{\partial^2 \psi}{\partial z^2}$ in comparison with $k \frac{\partial \psi}{\partial z}$, and equation 3.5 becomes [8]

$$\frac{\partial^2 \psi}{\partial x^2} + \frac{\partial^2 \psi}{\partial y^2} - 2jk \frac{\partial \psi}{\partial z} \simeq 0. \quad (3.6)$$

This is the *parabolic* or *paraxial* approximation often used for the solution of the open resonator problem. The validity and accuracy of this approximation will be discussed later.

The differential equation 3.6 has a form similar to the time dependent Schroedinger equation, suggesting that one can try a solution in cartesian coordinates of the form [40]

$$\psi = g(x, z) h(y, z) \exp \left\{ -j \left[P(z) + \frac{k}{2\gamma(z)} (x^2 + y^2) \right] \right\} \quad (3.7)$$

where g is a function of x and z , h is a function of y and z . $P(z)$ represents a complex phase shift along the axis, and $\gamma(z)$ a complex beam parameter, which describes the intensity and curvature of the beam. Substituting we find that

$$\frac{d\gamma}{dz} = 1 \quad \text{and} \quad \frac{dP}{dz} = -\frac{-j}{\gamma}. \quad (3.8)$$

For convenience we define

$$\frac{1}{\gamma} = \frac{1}{R(z)} - j \frac{\lambda}{\pi w^2(z)} \quad (3.9)$$

where one can see that $R(z)$ is the radius of curvature of the wavefront (surface of constant phase) at z , and $w(z)$ is a measure of the decrease of the field amplitude with distance from the axis. Since this decrease is Gaussian in nature, $w(z)$ is the distance from the axis at which the amplitude is $1/e$ times that on the axis — often called the *beam radius* or *spot size*. At the point where the beam contracts to its minimum diameter, called the *beam waist*, the beam parameter is purely imaginary

$$\gamma_0 = jz_0 \quad (3.10)$$

where

$$z_0 \equiv \frac{\pi w_0^2}{\lambda} = \frac{k w_0^2}{2}. \quad (3.11)$$

Here w_0 is the minimum spot size, still to be determined. Measuring z from this point, we have

$$\gamma = jz_0 + z = \frac{j\pi w_0^2}{\lambda} + z. \quad (3.12)$$

Substituting equation 3.12 into equation 3.9, we get

$$w^2(z) = w_0^2 \left[1 + \left(\frac{z}{z_0} \right)^2 \right] \quad (3.13)$$

and

$$R(z) = z \left[1 + \left(\frac{z_0}{z} \right)^2 \right]. \quad (3.14)$$

Trying functions of the form $g\left(\frac{x}{w(z)}\right)$ and $h\left(\frac{y}{w(z)}\right)$ in the differential equation 3.6 gives equations of the following form for both functions

$$\frac{d^2g}{dx^2} - 2x \frac{g}{dx} + 2mg = 0 \quad (3.15)$$

which defines the Hermite polynomial of order m [45]

$$g \cdot h = H_m \left(\sqrt{2} \frac{x}{w(z)} \right) H_p \left(\sqrt{2} \frac{y}{w(z)} \right) \quad (3.16)$$

For the fundamental mode ($m = p = 0$), one can just integrate $\frac{dP(z)}{dz} = -j/\gamma$ to get the phase shift, although it is more complicated for the higher order modes, yielding

$$P(z) = (m + p + 1) \tan^{-1} \left(\frac{z}{z_0} \right) - j \ln \left(\frac{w_0}{w} \right). \quad (3.17)$$

Combining all these factors, and suppressing the time dependence, we get

$$\begin{aligned} u_{mp}(x, y, z) &= \frac{w_0}{w(z)} H_m \left(\sqrt{2} \frac{x}{w(z)} \right) H_p \left(\sqrt{2} \frac{y}{w(z)} \right) \\ &\exp \left(\frac{-\rho^2}{w^2(z)} \right) \exp \left\{ -j \left[kz - \Phi_{mp}(z) + \frac{k\rho^2}{2R(z)} \right] \right\} \end{aligned} \quad (3.18)$$

where we define

$$\Phi_{mp} \equiv (m + p + 1) \tan^{-1} \left(\frac{z}{z_0} \right) \quad (3.19)$$

$$\rho^2 \equiv x^2 + y^2. \quad (3.20)$$

Anticipating later normalization following Bucci and Di Massa[8], we write for mirror separation D (see figure 3.2)

$$\begin{aligned} u_{mp}(x, y, z) &= \frac{2}{w(z)} \sqrt{\frac{1}{D\pi 2^{m+p} m! p!}} H_m \left(\sqrt{2} \frac{x}{w(z)} \right) H_p \left(\sqrt{2} \frac{y}{w(z)} \right) \\ &\exp \left(\frac{-\rho^2}{w^2(z)} \right) \exp \left\{ -j \left[kz - \Phi_{mp}(z) + \frac{k\rho^2}{2R(z)} \right] \right\}. \end{aligned} \quad (3.21)$$

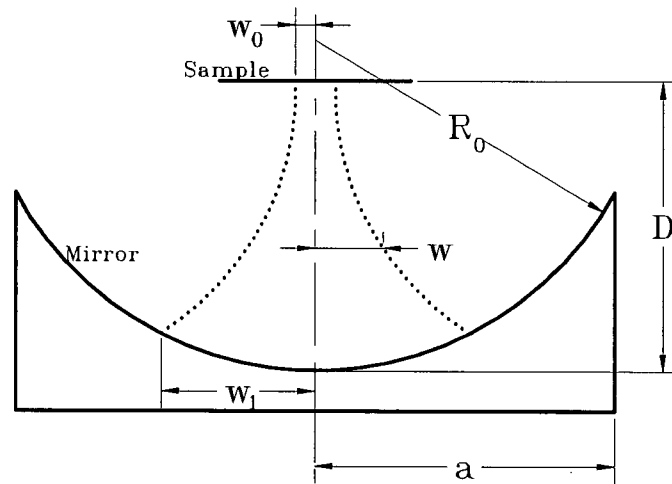


Figure 3.2: The semi-planar hemispherical geometry of the open resonator as used in the experiment.

For the semi-planar geometry used in this experiment (figure 3.2), the curvature of the beam at the spherical mirror is given by the curvature of the mirror.

$$R(z)|_{z=D} = R_0 \quad (3.22)$$

At the planar mirror (the sample), the beam should have no curvature $R(0) = \infty$. These geometrical constraints give the values for the constants z_0 and w_0^2 :

$$z_0 = \sqrt{D(R_0 - D)} \quad (3.23)$$

$$w_0^2 = \frac{2}{k} \sqrt{D(R_0 - D)}. \quad (3.24)$$

In a resonator, neglecting any losses due to the size of the mirrors or finite conductivities, a standing wave will be developed of the form

$$\Psi_{mpq} = u_{mpq}^{(+)} \pm u_{mpq}^{(-)} \quad (3.25)$$

where the (+) and (-) indicate waves traveling in the positive and negative z direction. If u is a transverse component of the electric field (say $u = e_y$), then the boundary

condition that must be satisfied for perfectly conducting mirrors is

$$u|_{\text{Mirror surface}} = 0. \quad (3.26)$$

This boundary condition is approximate, and corrections to it will be discussed in the following section. Using equations 3.25 and 3.21 this condition gives the propagation constant in the lossless case

$$k_{mpq} = \frac{m+p+1}{D} \tan^{-1} \left(\frac{D}{z_0} \right) + \frac{\pi(q+1)}{D} \quad (3.27)$$

where the label q refers to the number of nodes along the z axis. The standing wave field can thus be written

$$\begin{aligned} \Psi_{mpq}(x, y, z) = & \frac{2}{w(z)} \sqrt{\frac{1}{D\pi 2^{m+p} m! p!}} H_m \left(\sqrt{2} \frac{x}{w(z)} \right) H_p \left(\sqrt{2} \frac{y}{w(z)} \right) \exp \left(\frac{-\rho^2}{w^2(z)} \right) \\ & \sin \left[k_{mpq} z - \Phi_{mp} + \frac{k_{mpq} \rho^2}{2R(z)} + \frac{q\pi}{2} \right]. \end{aligned} \quad (3.28)$$

The multiplicative constants have been chosen such that, following Bucci and Di Massa, the eigenfunctions Ψ_{mpq} of the wave equation are normalized (to the same order as the approximation used in its derivation) with

$$\iiint_{\text{Cavity}} \Psi_{mpq} \Psi_{nst} dv = \begin{cases} 1 & \text{if } (mpq) \equiv (nst) \\ 0 & \text{otherwise.} \end{cases} \quad (3.29)$$

The mode of interest in this experiment is the mode Ψ_{00q} , often called TEM_{00q} since, to a first approximation, both the electric and magnetic fields are transverse.

3.4 Cavity Losses

The important quantities of the resonance for microwave measurements are the resonant frequency and the Q , or *quality factor* of the resonator. For the lossless case, as derived above, the resonant frequency of the mode mpq is given by

$$\omega_{mpq} = ck_{mpq} = c \left[\frac{m+p+1}{D} \tan^{-1} \left(\frac{D}{z_0} \right) + \frac{\pi}{D} (q+1) \right] \quad (3.30)$$

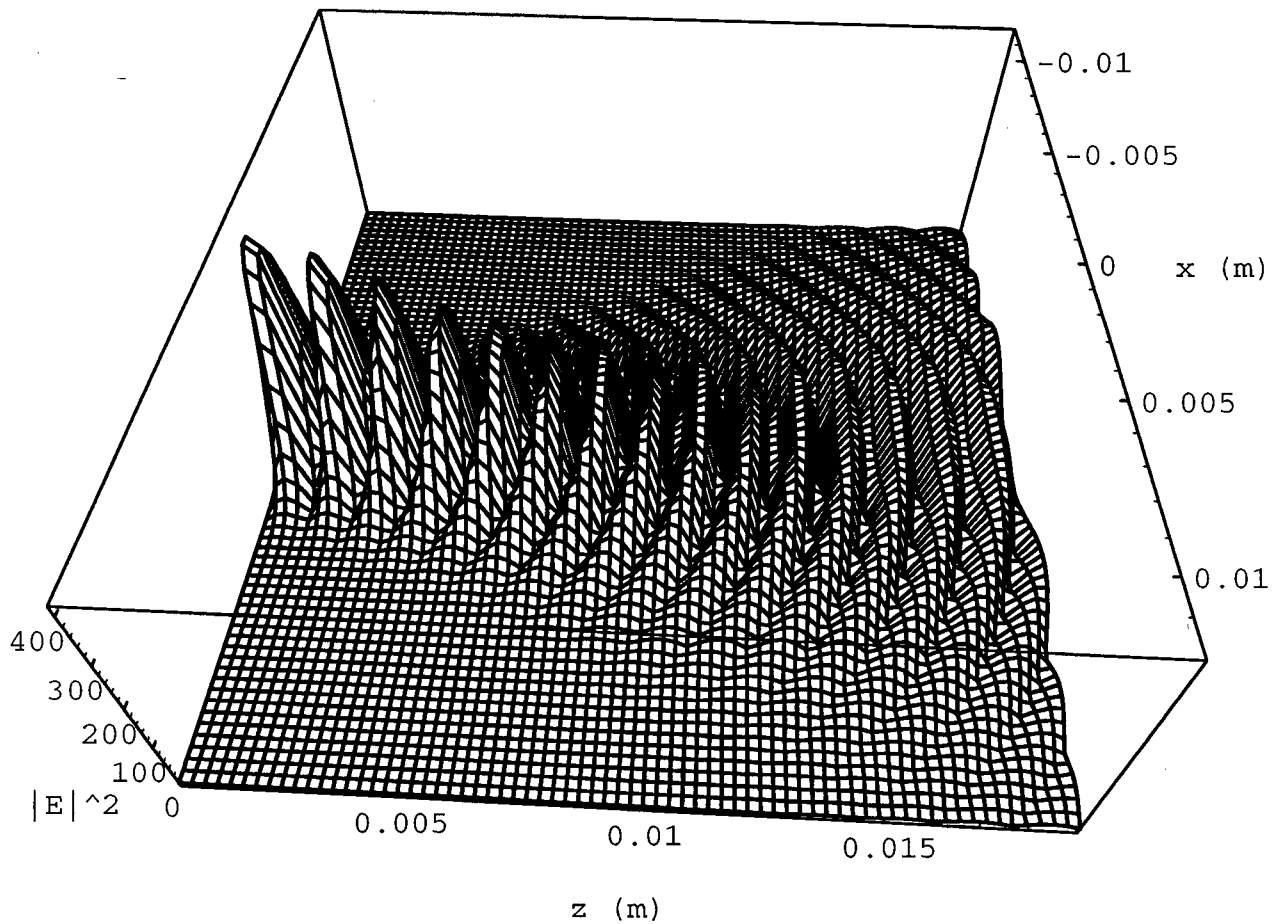


Figure 3.3: The amplitude of the transverse electric field (e_y) using the beam-wave approximation for the mode $[m, n, p] = [0, 0, 14]$ and dimensions as used in the experiment.

and the Q is infinite, since it is defined as

$$\frac{1}{Q} \equiv \frac{\text{Total Power Loss}}{\omega (\text{Total Stored Energy})} = \frac{P}{\omega U} \quad (3.31)$$

and we have neglected all power losses up to now. When the losses of the resonator are introduced, the resonant frequencies of the modes will shift, and the resonances will develop a finite width. These losses come from:

- finite conductivity of the mirror and sample surfaces.
- diffraction from having non-infinite mirrors (ie. some of the beam is radiated away).

- coupling between the resonator modes and the modes of the feeding waveguide.

$1/Q$ can be written as a sum of contributions to the total loss of the cavity:

$$\frac{1}{Q} = \frac{1}{Q_{mirror}} + \frac{1}{Q_{sample}} + \frac{1}{Q_{diffraction}} + \frac{1}{Q_{coupling}}. \quad (3.32)$$

Any electromagnetic field inside the cavity, including the losses, can be expressed as an eigenfunction expansion of the modes of the lossless case (except possibly at a finite number of points[41]):

$$\begin{aligned} \mathbf{E} &= \sum_{m,p,q} V_{mpq} \mathbf{e}_{mpq} \\ \mathbf{H} &= \sum_{m,p,q} I_{mpq} \mathbf{h}_{mpq}. \end{aligned} \quad (3.33)$$

For the y -polarized mode, let

$$\begin{aligned} \mathbf{e}_{mpq}(x, y, z) &= \frac{2}{w(z)} \sqrt{\frac{1}{D\pi 2^{m+p} m! p!}} H_m\left(\sqrt{2} \frac{x}{w(z)}\right) H_p\left(\sqrt{2} \frac{y}{w(z)}\right) \exp\left(\frac{-\rho^2}{w^2(z)}\right) \\ &\quad \sin\left[k_{mpq}z - \Phi_{mp} + \frac{k_{mpq}\rho^2}{2R(z)} + \frac{q\pi}{2}\right] \hat{j}. \end{aligned} \quad (3.34)$$

These modes form a complete orthogonal set. Since the differential equation used is scalar, there are two degenerate modes corresponding to the x and y polarisations. Any inhomogeneity without rotational symmetry in the xy plane of the resonator will tend to split the frequency of these modes. The resonator as designed has no method of distinguishing the two modes.

Following the argument of Kurokawa[41], $\nabla \times \mathbf{e}_{mpq}$ is a function similar to the magnetic field, since $\nabla \times \mathbf{E} = -j\omega\mu\mathbf{H}$. Let us define the functions \mathbf{h}_{mpq} such that

$$\nabla \times \mathbf{e}_{mpq} \equiv k_{mpq} \mathbf{h}_{mpq}. \quad (3.35)$$

This gives

$$\begin{aligned} \mathbf{h}_{mpq}(x, y, z) &= -\frac{2}{w(z)} \sqrt{\frac{1}{D\pi 2^{m+p} m! p!}} H_m\left(\sqrt{2} \frac{x}{w(z)}\right) H_p\left(\sqrt{2} \frac{y}{w(z)}\right) \exp\left(\frac{-\rho^2}{w^2(z)}\right) \\ &\quad \cos\left[k_{mpq}z - \Phi_{mp} + \frac{k_{mpq}\rho^2}{2R(z)} + \frac{q\pi}{2}\right] \hat{i} \end{aligned} \quad (3.36)$$

for the same polarization. By substituting equation 3.35 into $\nabla \times \mathbf{h}_{mpq}$ we get the symmetric result that

$$\nabla \times \mathbf{h}_{mpq} = k_{mpq} \mathbf{e}_{mpq}. \quad (3.37)$$

The constants I_{mpq} and V_{mpq} in the expansion are so named due to their similarity to the current and voltage in transmission line equations: [41]

$$V_{mpq} \equiv \iiint \mathbf{E} \cdot \mathbf{e}_{mpq} dv \quad (3.38)$$

$$I_{mpq} \equiv \iiint \mathbf{H} \cdot \mathbf{h}_{mpq} dv. \quad (3.39)$$

We can expand the function $\nabla \times \mathbf{E}$ in terms of the functions \mathbf{h}_{mpq} for the same reasons as given above,

$$\nabla \times \mathbf{E} = \sum_{m,p,q} \mathbf{h}_{mpq} \iiint (\nabla \times \mathbf{E}) \cdot \mathbf{h}_{mpq} dv. \quad (3.40)$$

Expanding the integral, using vector calculus identities and Gauss' theorem,

$$\begin{aligned} \nabla \times \mathbf{E} &= \sum_{m,p,q} \mathbf{h}_{mpq} \iiint (\nabla \cdot (\mathbf{E} \times \mathbf{h}_{mpq}) + \mathbf{E} \cdot (\nabla \times \mathbf{h}_{mpq})) dv \\ &= \sum_{m,p,q} \mathbf{h}_{mpq} \left(\iint \hat{\mathbf{n}} \cdot (\mathbf{E} \times \mathbf{h}_{mpq}) dS + k_{mpq} \iiint \mathbf{E} \cdot \mathbf{e}_{mpq} dv \right). \end{aligned} \quad (3.41)$$

Similarly, we can expand $\nabla \times \mathbf{H}$,

$$\nabla \times \mathbf{H} = \sum_{m,p,q} \mathbf{e}_{mpq} k_{mpq} \iiint \mathbf{H} \cdot \mathbf{e}_{mpq} dv \quad (3.42)$$

where the surface integral vanishes because $\hat{\mathbf{n}} \times \mathbf{e}_{mpq} = 0$ on the surfaces of the cavity.

These eigenfunction expansions can be then substituted into Maxwell's equations:

$$\begin{aligned} \nabla \times \mathbf{E} &= -j\omega\mu\mathbf{H} \\ \nabla \times \mathbf{H} &= j\omega\epsilon\mathbf{E} \end{aligned} \quad (3.43)$$

$$\begin{aligned} \sum_{m,p,q} \mathbf{h}_{mpq} \left(\iint \hat{\mathbf{n}} \cdot (\mathbf{E} \times \mathbf{h}_{mpq}) dS + k_{mpq} \iiint \mathbf{E} \cdot \mathbf{e}_{mpq} dv \right) \\ = -j\omega\mu \sum_{m,p,q} \mathbf{h}_{mpq} \iiint \mathbf{H} \cdot \mathbf{h}_{mpq} dv \end{aligned}$$

$$\sum_{m,p,q} \mathbf{e}_{mpq} k_{mpq} \iiint \mathbf{H} \cdot \mathbf{h}_{mpq} dv = j\omega\epsilon \sum_{m,p,q} \mathbf{e}_{mpq} \iiint \mathbf{E} \cdot \mathbf{e}_{mpq} dv. \quad (3.44)$$

Since the functions \mathbf{h}_{mpq} and \mathbf{e}_{mpq} are orthogonal, we can equate the coefficients of each vector, and solve for the constants I_{mpq} and V_{mpq} :

$$I_{mpq} = \frac{j\omega\epsilon}{k^2 - k_{mpq}^2} \iint \mathbf{h}_{mpq} \cdot (\hat{\mathbf{n}} \times \mathbf{E}) dS \quad (3.45)$$

$$V_{mpq} = \frac{k_{mpq}}{k^2 - k_{mpq}^2} \iint \mathbf{h}_{mpq} \cdot (\hat{\mathbf{n}} \times \mathbf{E}) dS. \quad (3.46)$$

Here k_{mpq} is the propagation constant for the lossless mode labeled (mpq) , and k is the propagation constant for the actual field. The surfaces over which the integration is done all have different boundary conditions on the field, so

$$\begin{aligned} \iint \mathbf{h}_{mpq} \cdot (\hat{\mathbf{n}} \times \mathbf{E}) dS &= \iint_{\text{Sample}} \mathbf{h}_{mpq} \cdot (\hat{\mathbf{n}} \times \mathbf{E}) dS \\ + \iint_{\text{Curved Mirror}} \mathbf{h}_{mpq} \cdot (\hat{\mathbf{n}} \times \mathbf{E}) dS &+ \iint_{\text{Coupling Apertures}} \mathbf{h}_{mpq} \cdot (\hat{\mathbf{n}} \times \mathbf{E}) dS + \iint_{\text{Everywhere Else}} \mathbf{h}_{mpq} \cdot (\hat{\mathbf{n}} \times \mathbf{E}) dS. \end{aligned} \quad (3.47)$$

Each of these contributions is related to the terms in the expansion of $\frac{1}{Q}$ in equation 3.32. The expression for the electric field in equation 3.33 is not correct up to the cavity boundary, since it forces the tangential component of \mathbf{E} to zero. For a conductor with finite conductivity, we can use the boundary condition of surface impedance (*cf.* Introduction) [8].

$$\hat{\mathbf{n}} \times \mathbf{E} = Z_S \hat{\mathbf{n}} \times \mathbf{H} \times \hat{\mathbf{n}}. \quad (3.48)$$

So for the mirror and sample surfaces,

$$\begin{aligned} \iint \mathbf{h}_{mpq} \cdot (\hat{\mathbf{n}} \times \mathbf{E}) dS &= Z_S \iint \mathbf{h}_{mpq} \cdot \hat{\mathbf{n}} \times \mathbf{H} \times \hat{\mathbf{n}} dS \\ &= \sum_{m'p'q'} I_{m'p'q'} Z_S \iint \mathbf{h}_{mpq} \cdot \mathbf{h}_{m'p'q'} dS. \end{aligned} \quad (3.49)$$

This total stored electromagnetic energy can be expressed in terms of either the electric or magnetic fields:

$$\begin{aligned} U &= \epsilon/2 \iiint \mathbf{E} \cdot \mathbf{E}^* dv = \mu/2 \iiint \mathbf{H} \cdot \mathbf{H}^* dv \\ &= \epsilon/2 \sum_{mpq} |V_{mpq}|^2 = \mu/2 \sum_{mpq} |I_{mpq}|^2. \end{aligned} \quad (3.50)$$

The power loss on the surface is

$$\begin{aligned} P &= \operatorname{Re} \left[Z_S \iint \mathbf{H} \cdot \mathbf{H}^* dS \right] \\ &= \operatorname{Re} \left[Z_S \sum_{m,p,q} \sum_{m',p',q'} I_{mpq} I_{m'p'q'}^* \iint \mathbf{h}_{mpq} \cdot \mathbf{h}_{m'p'q'} dS \right]. \end{aligned} \quad (3.51)$$

If losses are low, then we would expect the field present in the cavity to be similar to the field in a lossless cavity. Thus, the dominant term in the sum will be for $(mpq) = (m'p'q')$, and we can rewrite the equations for power energy and ohmic power loss as:

$$P_{mpq} = \operatorname{Re} [Z_S] |I_{mpq}|^2 \iint |\mathbf{h}_{mpq}|^2 dS \quad (3.52)$$

$$U_{mpq} = \mu/2 |I_{mpq}|^2. \quad (3.53)$$

Thus, we can write expressions for the Q of the cavity due to losses on the curved mirror and on the sample as

$$\frac{1}{Q_{Sample}} = \operatorname{Re}[Z_{S_{sample}}] \frac{2}{\omega\mu} \iint_S |\mathbf{h}_{mpq}|^2 dS \quad (3.54)$$

$$\frac{1}{Q_{Mirror}} = \operatorname{Re}[Z_{S_{mirror}}] \frac{2}{\omega\mu} \iint_M |\mathbf{h}_{mpq}|^2 dS. \quad (3.55)$$

As written, this assumes that \mathbf{h}_{mpq} is parallel to both mirror surfaces — which is not true for the curved mirror. This is another instance where the paraxial approximation has been invoked.

The fourth integral in equation 3.47 deals with the losses due to diffraction. This term can be dealt with by assuming that the field is an outgoing locally-plane wave, so

that

$$\hat{\mathbf{n}} \times \mathbf{E} = \zeta_0 \hat{\mathbf{n}} \times \mathbf{H} \times \hat{\mathbf{n}} \quad (3.56)$$

where the surface of integration is to simply extend the mirror surfaces until they intersect [8] and ζ_0 is the impedance of free space. This solution would be very rough, since the approximations and assumptions made are quite extravagant. However, this term should be small for the fundamental mode if the mirror and sample have a diameter greater than twice the spot size. This follows from an empirical discussion by Cullen [44] based on analytic results by Weinstein [46] for the confocal geometry. Weinstein expresses the loss due to diffraction as

$$Q = kD/\Lambda \quad (3.57)$$

where Λ is the loss per pass, given empirically by

$$\Lambda \simeq 200 \exp(-4a^2/w^2) \quad (3.58)$$

where a is the radius of the mirror (*not* radius of curvature) and w is the spot size of the beam at the mirror. For the geometry of the experiment, this gives Q 's on the order of 10^8 — much higher than the Q 's due to ohmic losses.

The area of the coupling apertures is small, and can be neglected in many cases. However by using the boundary condition that the fields must be continuous with the feeding waveguides, one can determine the amount of energy coupled into the resonant mode [8] [47]. It is likely, however, that any coupling determined theoretically will disagree with the actual values, due to the cumulative effect of approximations and non-idealities in the geometry (*eg.* non-circular coupling holes, finite thickness of the coupling holes, etc). A more empirical approach to the coupling will be discussed in the following chapter (*cf.* experimental data).

The resonant frequency of the cavity, including losses, can be found by a variational formula [41]

$$k^2 = \frac{\iiint [(\nabla \times \mathbf{E})^2 + (\nabla \cdot \mathbf{E})^2] dv - 2 \iint \hat{\mathbf{n}} \times \mathbf{E} \cdot \nabla \times \mathbf{E} dS}{\iiint \mathbf{E} \cdot \mathbf{E} dv}. \quad (3.59)$$

The shift in frequency due to the change of the penetration depth of the superconductor with frequency is an important quantity measured in this laboratory [20] [15], however it is inaccessible to measurement in this apparatus since the resonant frequency is not stable enough in general.

3.5 Beyond the Beam-Wave Theory

The beam-wave theory, as developed in the preceding section, depends upon the validity of the parabolic approximation

$$\frac{\partial^2 \psi}{\partial z^2} \ll 2k \frac{\partial \psi}{\partial z} \quad (3.60)$$

which can be shown to be equivalent to saying

$$\alpha^2 \equiv \frac{k^2 w_0^2}{2} \gg 1. \quad (3.61)$$

This constraint is definitely satisfied for the laser resonators for which this theory was developed and for which the resonator dimensions are much greater than the wavelength of the light, however its validity is less obvious for millimeter-wave systems. The approximation is even less valid in the experiment described here, since the objective is to have a spot size of the same order of magnitude as the wavelength of the radiation. Although Cullen has shown that the theory is actually more accurate than this in terms of the resonant frequency (to approximately $O(\alpha^{-4})$ [42]), the expressions for the fields are not accurate to this order and a more accurate theory is desirable.

A second problem with the theory is that, as can be seen from equations 3.21 and 3.14, the surfaces of equal phase are not spherical, but have a parabolic shape. This difference will be small near the axis, however, and can be treated with perturbation techniques [42] [48]. A third remaining defect with the theory lies in the fact that it was developed using a scalar method. Thus the boundary condition that $u = 0$ on the mirror surfaces is not true for all cartesian components of \mathbf{e} . What actually is involved is \mathbf{e}_{tan} , the tangential component of the electric field. This will be close to a combination of e_x and e_y for large radius of curvature, but will strictly involve e_z as well. A vector theory, incorporating the relative intensities of the components, but satisfying the actual boundary conditions, is important for improved accuracy.

A vector field theory of the fundamental mode of open resonators has been developed by Cullen and Yu [43]. The derivation of this theory will be sketched here, and behaviour of the fields outlined, though most of the calculations from the preceding section will not be repeated.

The starting point of this theory is to consider an infinitesimal electric dipole located at the origin and directed along the x -axis. The vector potential of such a system is

$$\mathbf{A} = \hat{i}(1/r) \exp(-jkr) \quad (3.62)$$

where

$$r = \sqrt{x^2 + y^2 + z^2}. \quad (3.63)$$

If this dipole is shifted along the z axis a distance z_0 the change in the field is trivial. If, however, one considers a shift of the field $-jz_0$, the interpretation is less obvious, but the mathematics still simple (since Maxwell's equations will be satisfied in the same way).

Thus

$$r = \sqrt{x^2 + y^2 + (z + jz_0)^2}. \quad (3.64)$$

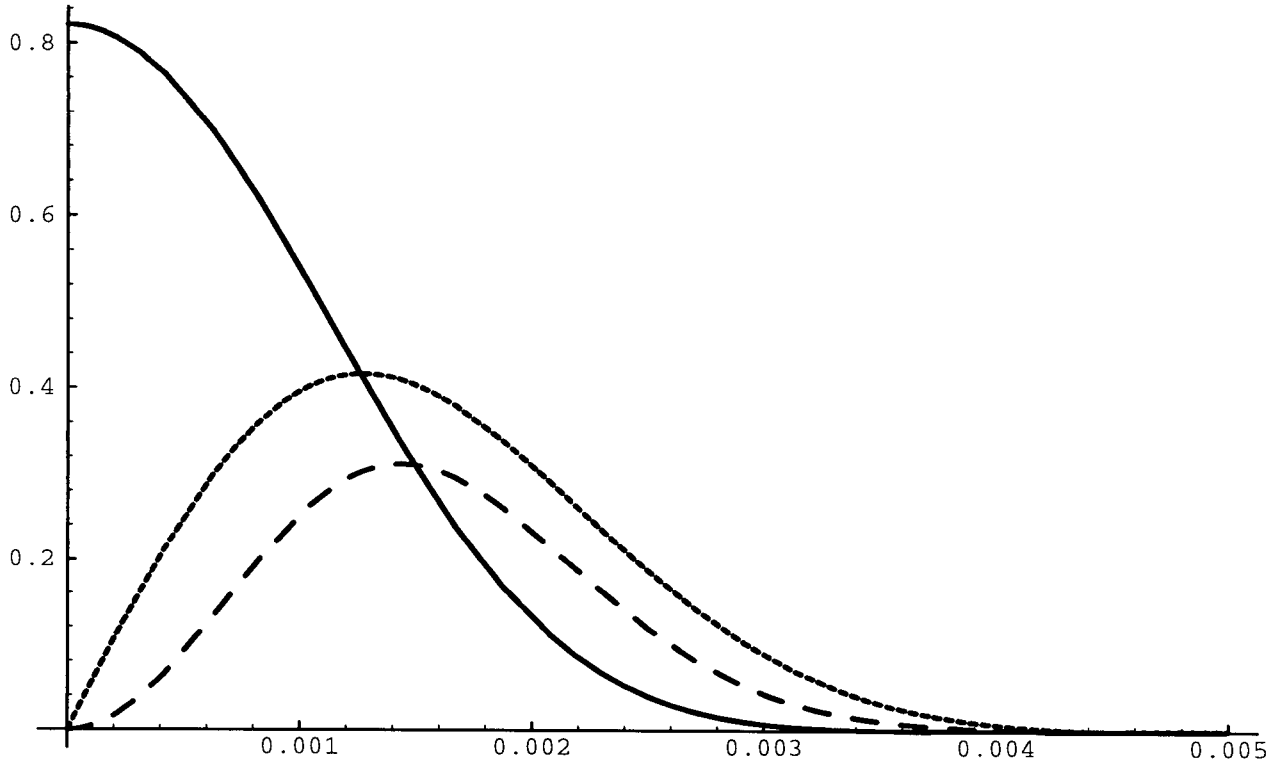


Figure 3.4: Relative intensities of the cartesian components of the field along the $y = x$ line using the complex point-source theory. Solid: $|e_y|$, Dashed: $k^2 w_0^2 |e_x|$, Dotted: $k w_0 |e_z|$. The parameters were chosen for the geometry used in the experiments of this thesis.

If we now assume that z_0 is large and expand equation 3.62 binomially, we find, except for a constant factor

$$\mathbf{A} = \hat{i} \frac{j z_0}{z + z_0} \exp \left[-j k z - j k \frac{x^2 + y^2}{2(z + j z_0)} \right] \quad (3.65)$$

which is identical to equation 3.18 for $m = p = 0$ and the substitutions for R and w_0 [44]. The physical interpretation is now more clear, in that the solution to Maxwell's equations in the paraxial approximation, corresponds to a Gaussian beam. However, without making the paraxial approximation, we have a solution that satisfies Maxwell's equations exactly, and that is an inherently vector solution (all six components of the fields can be found explicitly). These fields can be written down exactly[43], although they are quite complicated. Using a consistent order of approximation, $O(\alpha^{-4})$, Cullen

and Yu give tractable equations for the fields in an open resonator of even mode number q :

$$e_x = \frac{2xy}{k^2 w_0 w^3} \exp\left(-\frac{\rho^2}{w^2}\right) \sin\left(kz - 3\Phi + \frac{k\rho^2}{2R}\right) \quad (3.66)$$

$$e_y = \frac{w_0}{w} \exp\left(-\frac{\rho^2}{w^2}\right) \left[\sin\left(kz - \Phi + \frac{k\rho^2}{2R}\right) - \frac{2}{k^2 w_0 w} \sin\left(kz - 2\Phi + \frac{k\rho^2}{2R}\right) + \frac{5x^2 + 3y^2}{k^2 w_0^2 w^2} \sin\left(kz - 3\Phi + \frac{k\rho^2}{2R}\right) - \frac{\rho^4}{k^2 w_0^3 w^3} \sin\left(kz - 4\Phi + \frac{k\rho^2}{2R}\right) \right] \quad (3.67)$$

$$e_z = \frac{2x}{kw^2} \exp\left(-\frac{\rho^2}{w^2}\right) \sin\left(kz - 2\Phi + \frac{k\rho^2}{2R}\right). \quad (3.68)$$

And the \mathbf{h} field can be derived from this. Again, this theory does not take spherically shaped mirrors for boundary conditions, but this can be corrected through perturbation theory, and the correction to the resonant frequency is $O(\alpha^{-4})$, and can be ignored [43].

These equations can be used in the same way that the beam-wave theory equations are used in the development of Q , but the extra accuracy obtained is not useful in most applications. This is because the $1/Q$ contribution from the loading of the resonator by the waveguide circuit is likely to mask any deviation from the simple beam-wave picture.

The complex-point source theory does give some idea of the relative intensities of the components of the field. It shows that the approximation that both the electric and magnetic fields are transverse is only good to order $1/\alpha$ (since $e_x \sim \alpha e_z$).

Chapter 4

Millimeter-Wave System

4.1 Introduction

One of the important results from the preceding chapter is the expression for the spot size on the sample (equation 3.24):

$$w_0^2 = \frac{2}{k} \sqrt{D(R_0 - D)}.$$

To measure small samples, a small w_0 is required. This quantity scales inversely with the frequency, of course, so we will want to work with high frequencies for good spatial resolution. The highest frequency millimeter-wave source and detector pair available in the lab is at ~ 117 GHz, which is the frequency used in our experiments. As well, the decision to work with a flow cryostat, and the final design of this cryostat, impose restrictions on the size of the resonator to be used. In this chapter, the design of the resonator and the millimeter-wave detector/source pair are outlined.

4.2 Millimeter-Wave System

The source and detector for the experiment are a modification of a 115 GHz spectrometer previously used for experiments on atomic hydrogen and deuterium [49]. The millimeter-wave source is a klystron (Varian VRT2123A7) which operates nominally at 114.5 GHz. The klystron is actually quite old, and the lowest operable frequency has increased with age. It is currently operated at about 115.6 GHz. This frequency is stabilized by locking to the 8th harmonic of a reference signal provided by the HP 83620A synthesizer ($f_{REF} =$

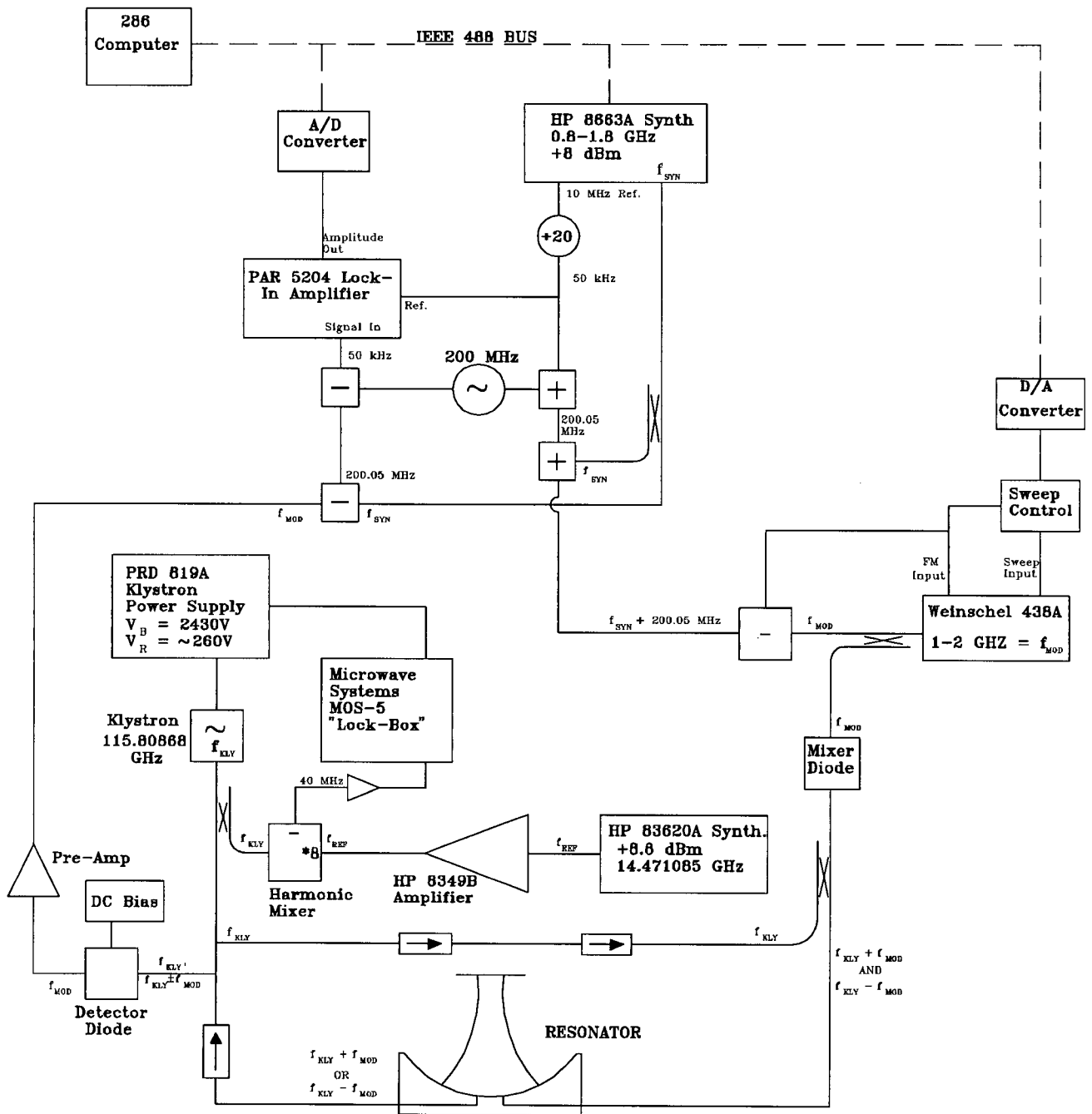


Figure 4.1: Block diagram of the millimeter-wave system

14.471085 GHz for all work described here). This locking is accomplished by controlling the reflector voltage using a Microwave Systems MOS-5 frequency stabilizer (or “lock-box”) which keeps the klystron operating at 40 MHz from f_{REF} :

$$f_{KLY} = 8 * f_{REF} \pm 40\text{MHz} = 115.80868\text{GHz}. \quad (4.1)$$

This is a stable baseline frequency from which the measurements are based, however it is desirable to have a swept frequency source for accurate measurements of Q [50]. The original spectrometer operated at a fixed frequency, mixing the stabilized klystron signal with 1480 MHz from a SSB generator, and using a heterodyne system [49]. Since there is no easy way to sweep the klystron frequency, we have used a modification of this system, the main difference being that we scan the intermediate frequency, providing a limited sweep capability.

A swept frequency from the HP 8663A synthesizer ($f_{SYN} = 0.8$ to 1.8 GHz) is mixed with both a 50 kHz source and a 200 MHz source (figure 4.1) giving a number of harmonics. In the original spectrometer, the unwanted sidebands were filtered out. In the current design, because f_{SYN} is swept, such filtering is impractical. To obtain a clean single frequency to mix with the klystron, a separate 1-2 GHz source (Weinschel 438A) is locked to the desired sideband. This locking is accomplished by setting the frequency of the oscillator roughly to the desired point through the sweep input of the Weinschel, and fine, fast adjustments through the FM input. A sweep control circuit has been designed so that if lock is lost, the frequency is swept rapidly until lock is regained. By keeping the locking time shorter than the frequency step rate, erroneous measurements are avoided.

This clean, variable frequency f_{MOD} , is fed to a millimeter-wave diode which also receives a large signal from the klystron. The diode operates in the non-linear region, so it mixes the two signals, sending a combination of f_{KLY} , $f_{KLY} + f_{MOD}$ and $f_{KLY} - f_{MOD}$ to the experimental resonator. The open resonator acts as a narrowband filter, so essentially

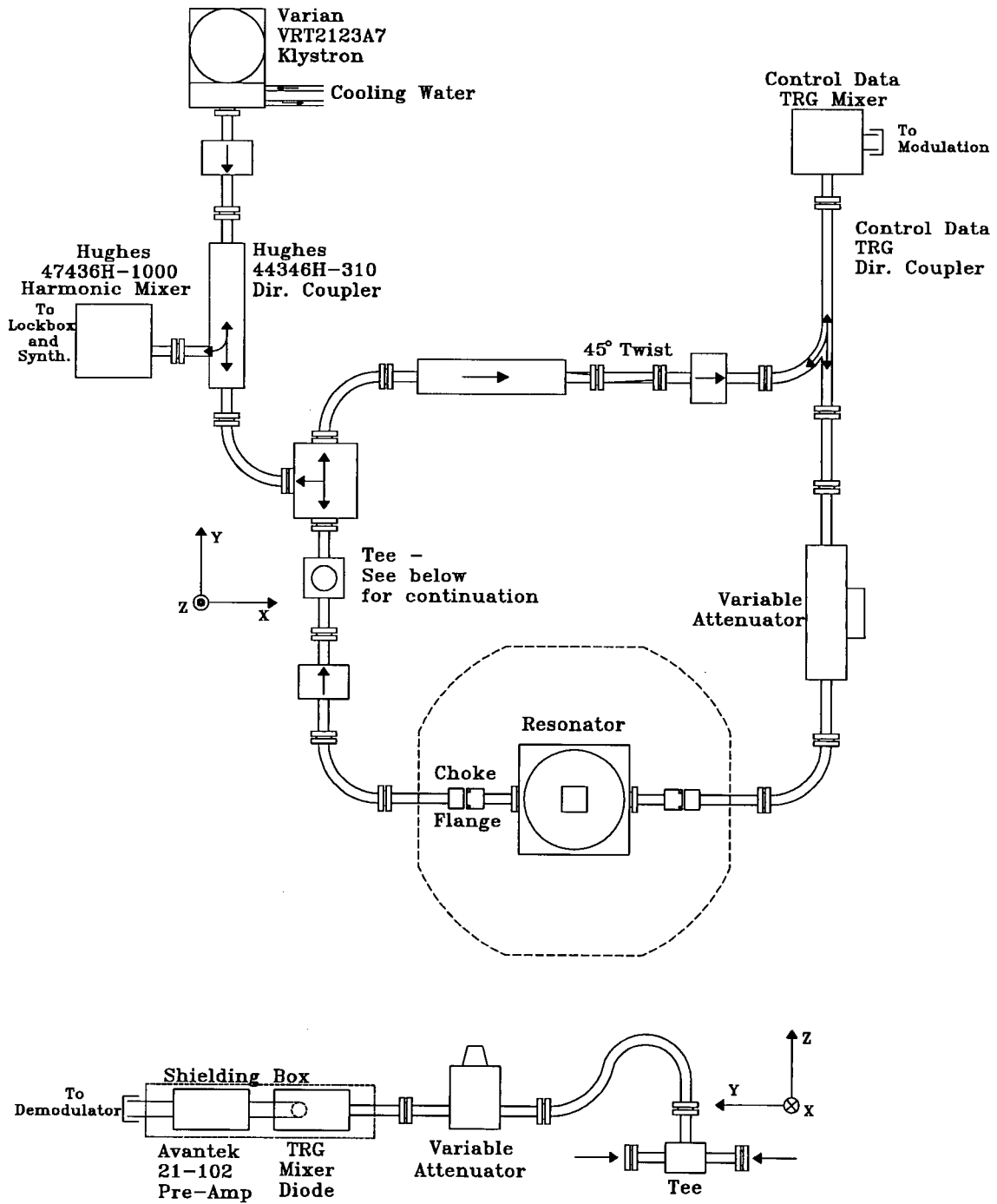


Figure 4.2: Schematic diagram of waveguide circuit

only one of these sidebands will be near the resonant frequency f_{RES} , the others will be filtered out. This signal is detected through the reverse of the input heterodyne system, finally giving a 50 kHz signal which is detected with a PAR 5204 two-phase lock-in amplifier.

This complicated heterodyne system is used because the signal to noise ratio is quite low, and coherent phase sensitive detection must be used. As the experiment currently stands, the phase information is not used in determining the Q of the resonator, however the modifications to do so would certainly be possible. It turned out to be difficult to convert the fixed frequency SSB spectrometer to a swept source, but the final configuration yields an adequately level signal over the range of 116.8 GHz to 117.6 GHz (see the following chapter). This frequency is obtained by taking the positive polarity for all mixing frequencies, the mode used for all measurements described here.

4.3 Resonator Design

Once the frequency of the source and the size of the experimental chamber have been set, it remains to determine the actual design of the resonator. The criteria are essentially as follows:

1. spot size w_0 as small as possible (limited by number 3 below).
2. diffraction minimized: keep the diameter of the mirror $a \geq 2w_1$, the spot size on the curved mirror.
3. keep the assumption of $k^2w_0^2 \gg 1$ satisfied.

To satisfy these constraints we would like to operate in the regime where $D \sim R$ — the hemispherical geometry. Other researchers using open resonators for R_S measurements are split on which geometry to use: either half-confocal or hemispherical [26] [27].

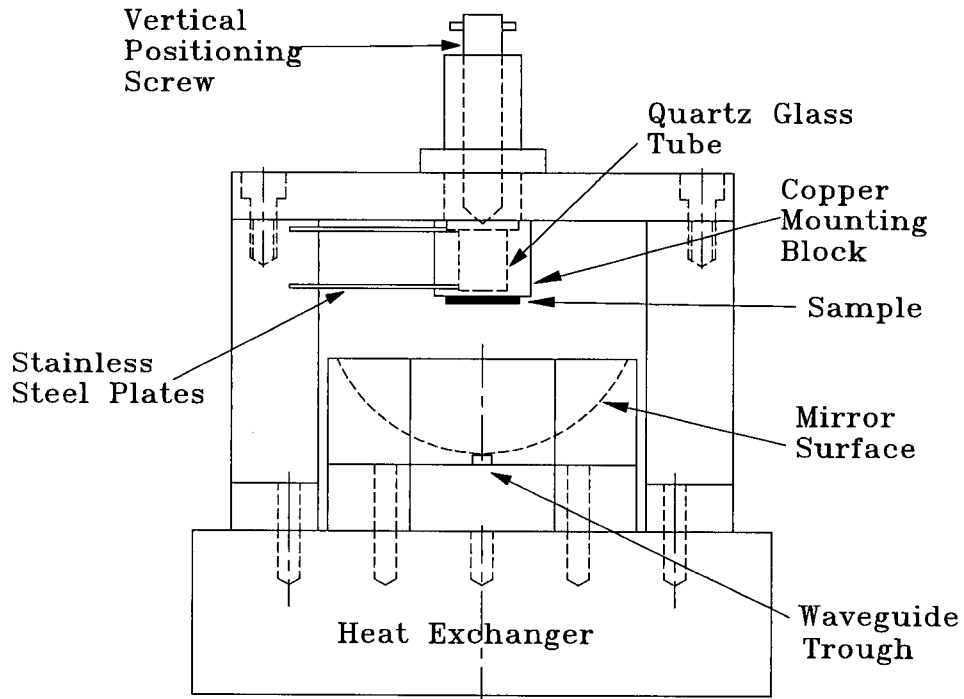


Figure 4.3: The design of the resonator and sample positioning apparatus. See also 2.2 for a photograph.

For large samples or very high frequency, the semi-confocal setup is preferable, since diffraction losses are minimized. In this experiment, the total size of the resonator, and the size of the sample make the hemispherical resonator the ideal choice.

The mirror to sample separation in the apparatus, D , must be variable for two reasons. Firstly, samples are attached to a support facing the curved mirror (see figure 4.3), so any variation of substrate or sample thickness will change the effective resonator dimensions, and thus its electromagnetic characteristics. In moving this block vertically D can be kept constant. Secondly, because of the limited frequency sweep range, and the fact that theoretical calculations of the resonant frequency are approximate, the mirror separation must be variable to ensure that the f_{RES} lies within this accessible range.

Additionally, as the cryostat cools, the mirror separation distance changes due to thermal contraction which changes f_{RES} . Thus D must be variable at low temperature.

This is accomplished by having the sample-mounting block attached to two parallel flexible stainless steel plates which allow vertical travel. The height is set by pushing down from above with a finely threaded screw. A retractable rod engages this screw so that there is no heat conduction when disengaged (figure 4.3).

The sample mounting block is formed of copper (about 1 cm^3) and is cooled via conduction down the stainless steel plates. To this block is attached a thermometer and heater, to control the temperature of the sample. In early versions of the apparatus, the block was solid copper, but temperature changes were found to cause changes in D due to thermal expansion and thus f_{RES} . By inserting a quartz glass tube in the main part of the block (see figure 4.3), problems with thermal expansion were reduced to a more acceptable level. The actual frequency drift with temperature will be discussed in the following chapter, but is now stable to within 5 MHz over the course of an experiment.

The resonator as fabricated has radius of curvature of $R = 2.08 \text{ cm}$ and radius of the mirror aperture of $a = 1.91 \text{ cm}$ (see figure 2.2). The theoretical performance of a resonator with these characteristics is shown in the accompanying figures. These calculations neglect all losses other than the ohmic resistance of the sample and mirror.

4.4 Coupling

The microwave energy used for the experiment must be coupled both into and out of the resonator, in order that measurements be made. We have decided to work with a transmission mode cavity (in which energy is coupled in at one spot, and out another) since this configuration is better suited to situations where the loss has a wide variation with temperature and sample. Coupling is accomplished by connecting waveguides to small apertures near the axis of the resonator on the curved mirror. Because there must be two holes, slightly off center, the transmission method does have some disadvantages

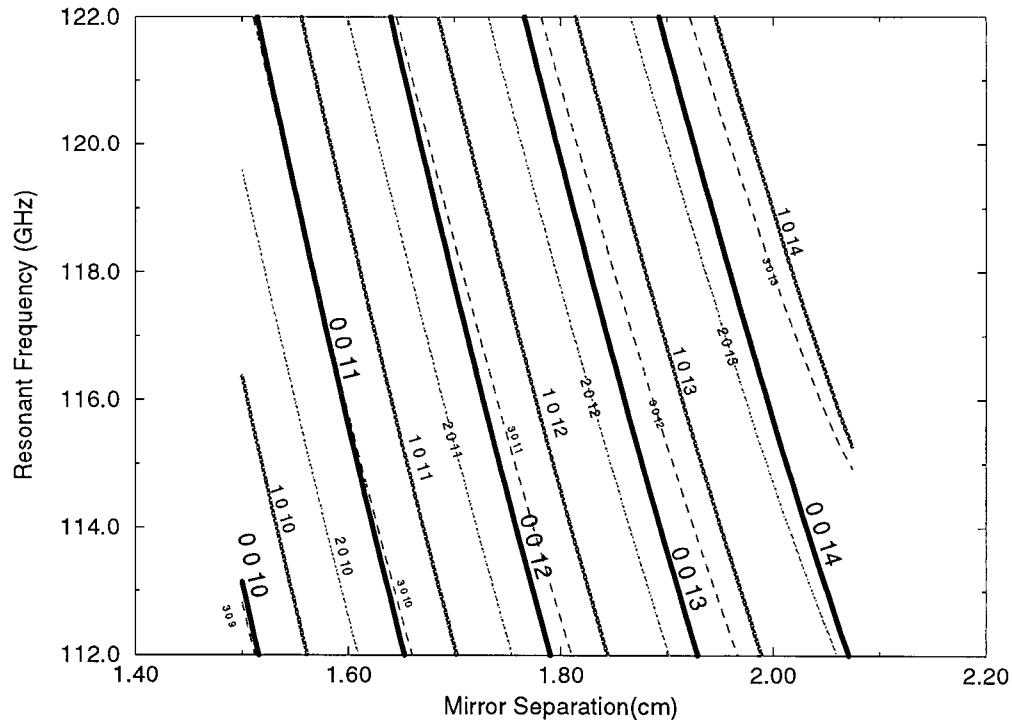


Figure 4.4: Mode chart of the resonator as built. These modes depend on the beam-wave theory and are approximate. As well losses are ignored. Hence, this chart is only a guide as to the behaviour of f_{RES} with mode number and D .

compared to reflection methods. These two imperfections in the curved mirror cause scattering and lower the Q of the resonator.

It is difficult to determine *a priori* what size of holes are needed to give adequate signal strength. There are theoretical and phenomenological models [47] [8], however the assumptions made often negate their utility in this problem. In this apparatus, the size of the coupling holes was determined empirically, by starting with small holes and increasing their size until an adequate signal strength was observed. The final size of the holes is $\sim 0.025''$ diameter, which is not negligible in comparison to the wavelength of radiation, and thus will lower the Q of the resonator.

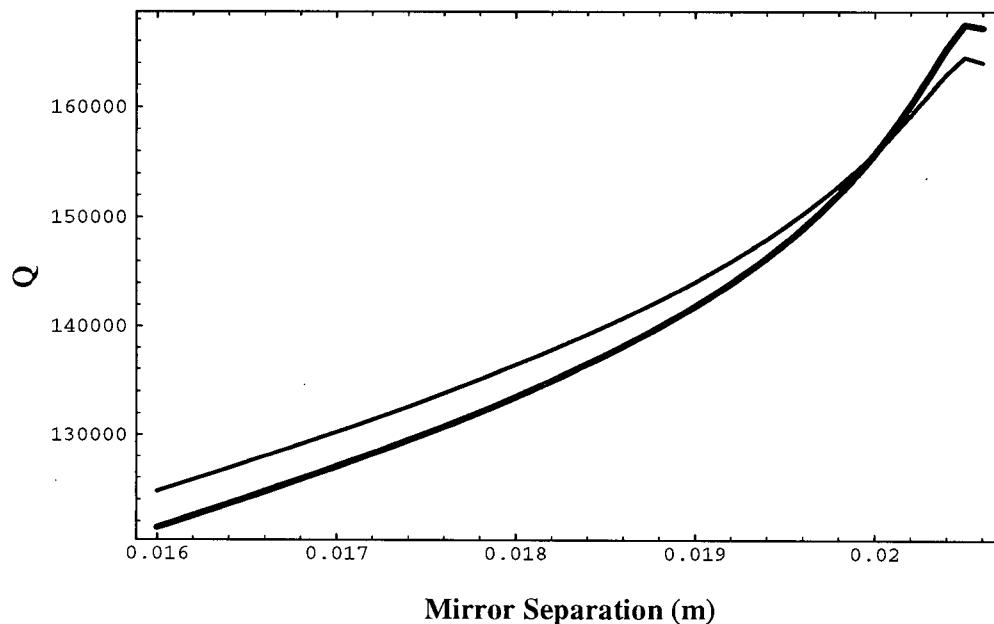


Figure 4.5: Numerical simulation of the resonator Q for copper at 77 K as a function of the mirror separation in the complex-point-source model (*cf.* Chapter 3). The thick line corresponds to the mode TEM_{0013} and the thin line to TEM_{0014} . The data on this graph becomes increasingly inaccurate as D approaches $R = 2.08\text{cm}$, due to neglect of diffraction losses which dominate in this regime.

A related matter concerns the problem of bringing the microwave power to the resonator without a large heat load. This is accomplished by having low thermal conductivity stainless steel waveguides, as well as non-contacting choke flanges. These flanges have been used in microwave work for years for other reasons ([51] and other volumes of the *M.I.T. Radiation Laboratory series*), and also have been exploited in low temperature work [52]. By having a $\lambda/4$ shorted stub around the waveguide, the gap between waveguide sections is minimized as a discontinuity for the fields. Radiation from the joint, as well as reflection down the waveguides are minimized. In the experiment, these flanges are used on both the input and output waveguides. Their performance will be discussed in the following chapter.

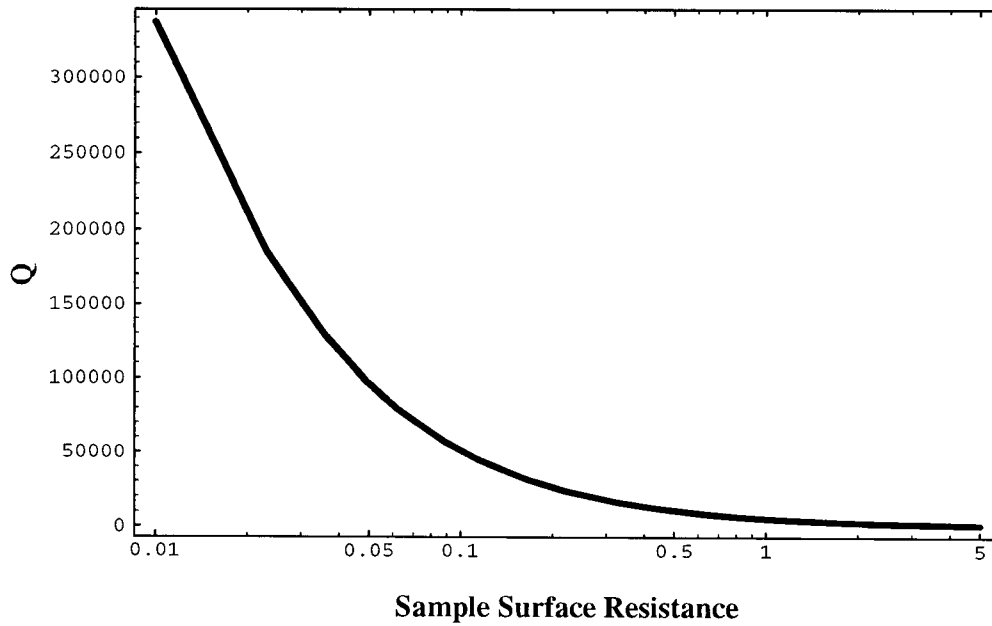


Figure 4.6: Numerical simulation of the resonator Q at 117 GHz and 77K, as a function of R_S of the sample in the complex-point-source model. This corresponds to a mirror separation of 1.986 cm.

4.5 Microwave measurements

Following the derivations of the previous chapter, the basic relation in the measurement of a microwave resonator is:

$$\frac{1}{Q} \propto \sum \text{All Losses.} \quad (4.2)$$

When measuring the Q of a resonator, one must have some method of coupling energy into and out of the resonator, with a circuit including source and detector. This contributes to the losses for the resonator.

Near a particular resonant mode of the resonator, it is possible to represent the energy stored in the fields of the resonator by the energy stored in the lumped parameters of an equivalent circuit [53]. The equivalent circuit of a resonator can be described by three parameters:

$$\omega_0^2 = \frac{1}{LC} \quad (4.3)$$

$$Q_0 = \frac{\omega_0 L}{R} \quad (4.4)$$

$$R_0 = \omega_0 L Q_0 \quad (4.5)$$

where ω_0 is the resonant frequency, Q_0 is the unloaded quality factor of the resonator (called simply Q until this point) and R_0 is the shunt resistance of the resonator. When joined to the rest of the system through coupling, the equivalent circuit can be represented as shown in figure 4.7 [50].

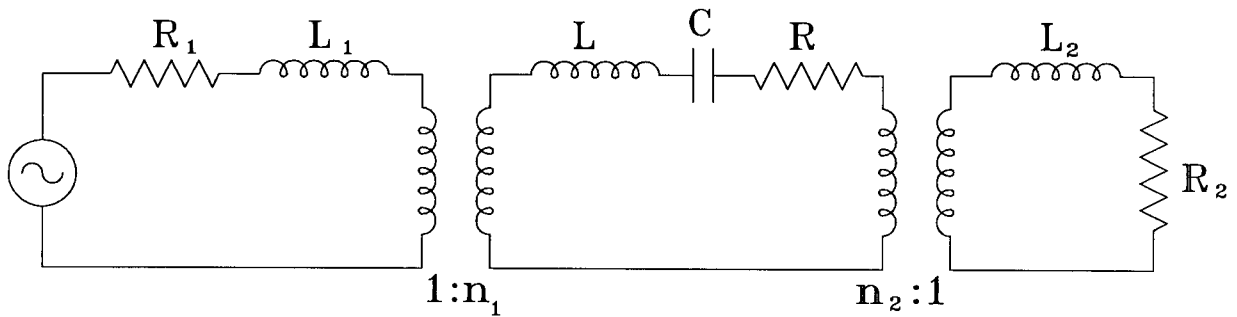


Figure 4.7: Lumped-element equivalent circuit of a resonator connected between a generator and a detector.

The method in which the coupling is represented can be shown to have no effect on the final result, and is shown here as two ideal transformers. The *loaded* Q of the system, Q_L , can be found by examining this circuit, giving:

$$Q_L = \frac{\omega_0 L}{R + n_1^2 Z_1 + n_2^2 Z_2} \quad (4.6)$$

where Z_1 and Z_2 are the characteristic impedances of the input and output transmission lines respectively [50]. Defining the coupling constants

$$\beta_1 = n_1^2 \frac{Z_1}{R} \quad (4.7)$$

and similarly for β_2 , the relation between the unloaded Q and the loaded Q of the system can be written

$$\frac{1}{Q_L} = \frac{1 + \beta_1 + \beta_2}{Q_0}$$

$$\begin{aligned}
&= \frac{1}{Q_0} + \frac{\beta_1}{Q_0} + \frac{\beta_2}{Q_0} \\
&= \frac{1}{Q_0} + \frac{1}{Q_1} + \frac{1}{Q_2}
\end{aligned} \tag{4.8}$$

where Q_1 and Q_2 are the coupling Q 's. These two terms are simply two additional terms to equation 4.2.

Thus the measured Q of a resonator will be lower than the Q if it were isolated from the circuit. To make good measurements of the Q of the resonator, it is desirable to work with very weak coupling (small β 's). There is no way of modifying the coupling of the system as it is currently constructed, and hence no method of determining Q_0 on its own.

The loss due to coupling, as well as due to all factors except the sample, should be constant between experiments and during an experiment at different temperatures. Thus the relation between the Q of the cavity and the surface resistance of the sample can be written, using equations 4.2 and 3.55 as:

$$\frac{1}{Q_L} = R_{S_{sample}} \frac{2}{\omega\mu} \iint_{Sample} |\mathbf{h}|^2 dS + \text{constant} \times (\text{Other Losses}). \tag{4.9}$$

In this equation the relationship between the surface resistance and the measured quantity of the Q of the resonator is clearly noted. The main idea of the experiment is that this equation can be rewritten simply as (writing Q instead of Q_L again)

$$\frac{1}{Q} = \alpha R_{S_{sample}} + \beta \tag{4.10}$$

where α and β are two constants, independent of the sample. Though both of these constants are related to values from the theory (in the case of α the theoretical value is shown above), the approximations made in their derivation would make the final result suspect. In the following chapter the values of these constants are found experimentally.

Chapter 5

Experimental Method

5.1 Introduction

In this chapter, I will describe the techniques used in taking, calibrating and analyzing the surface resistance data as measured by the apparatus previously described. Measurement of the surface resistance of normal metals will be described here, although the techniques would be identical for superconducting thin films.

The basic formula used in analyzing the data is the relation

$$Q = \frac{1}{\alpha R_S + \beta} \quad (5.1)$$

where Q , the resonator quality factor, is the measured quantity, and R_S , the surface resistance of the sample, is the desired quantity. This equation comes from the theoretical discussion in chapter 3, as well as the section on microwave measurements in chapter 4. The losses of the resonator each contribute independently to $1/Q$, allowing a simplification of the form of equation 5.1. The parameter α relates the fraction of the loss of the resonator due to the surface resistance of the sample. The parameter β encompasses all other losses in the resonator (surface resistance of the curved mirror, scattering losses, etc.). It is hoped that the product αR_S is not small in comparison with β for accurate measurement.

Although it is possible to make estimates for the values of α and β from theory (chapters 3 and 4), such values are only approximations, and ignore such losses as the finite size of the mirrors and the effect of coupling holes. Therefore, the parameters will

be determined empirically by measuring the surface resistance of known samples.

5.2 Metallic Samples

Since the surface resistance of high T_C superconductors at 117 GHz and $\sim 77\text{K}$ is not much different from that of metals (such as copper) at similar temperatures, it is convenient to use good metals as references for calibration of the resonator. It is, however, important to realize that the simple relation for the surface resistance of a conventional metal given in the introduction (equation 1.19) does not necessarily apply for a good metal at cryogenic temperatures and high frequencies. This is due to the *anomalous skin effect*, where the mean free path in the material is comparable to the classical skin depth. Hence conduction is no longer a local phenomenon, and more complicated effects are introduced [54].

The criterion for these effects to be important is given by the product $\omega\tau$, the frequency of the radiation times the scattering time for electrons in the metal. When $\omega\tau \ll 1$, then the standard formula applies, $R_S = \frac{1}{\sigma\delta}$. In Dingle's two papers [55] [56], the quantitative theory of Reuter and Sondheimer [54] is evaluated numerically, and the results for various metals are tabulated. The surface resistance for copper as a function of temperature at 117 GHz is shown in figure 5.2.

The surface resistance of brass is used as a calibration as well. Here, the literature is not very much help when finding the resistivity, since there are many different alloys, all given the name brass. The d.c. resistivity of a small sliver of the same material used in the open resonator experiment was measured directly [58]. From this the surface resistance was calculated as $R_S = \frac{\rho}{\delta}$. Both the copper and brass samples used for surface resistance measurements were $1 \times 1\text{cm}^2$. They were mechanically polished to $\sim 5\mu\text{m}$ grit, then chemically polished (using a solution of 1/3 each of nitric acid, orthophosphoric acid and

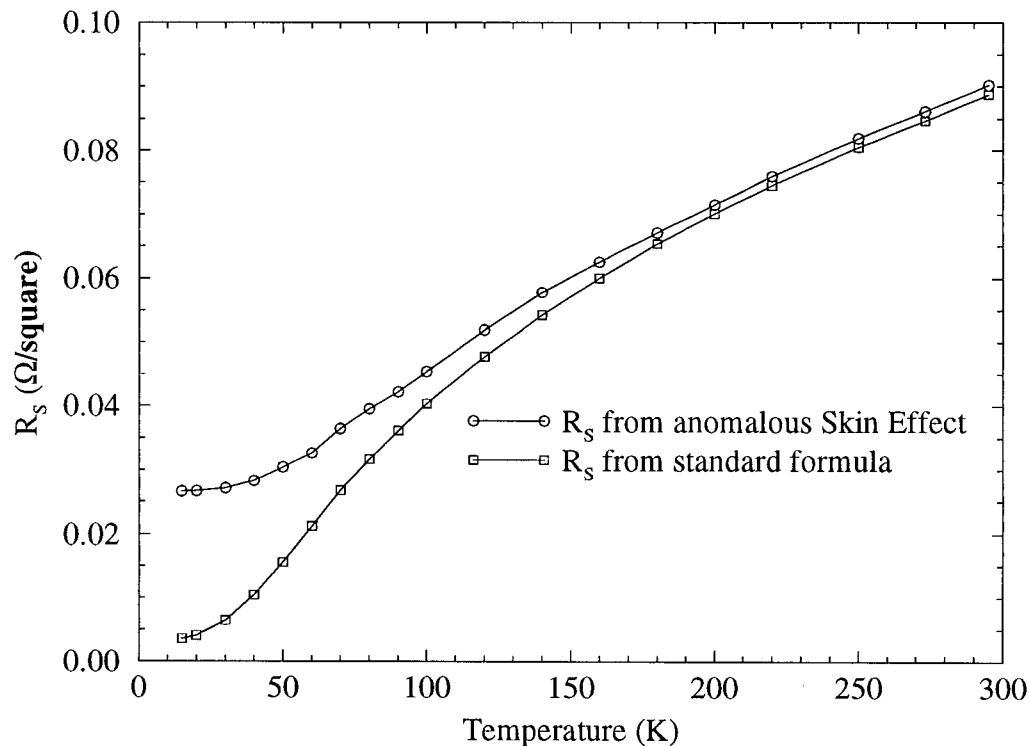


Figure 5.1: Surface resistance of copper at 117 GHz calculated from d.c. resistivity data from the literature [57], using the standard skin depth formula (squares); and using a numerical solution of the full integral equations accounting for the anomalous skin effect [56].

glacial acetic acid at 70 deg C [59]) to remove damage from the mechanical polishing. The brass surface became noticeably shinier after the chemical polish, though results were only mediocre with copper, despite repeated trials with various methods (including electrochemical polishing [59] [60]).

5.3 Measurement Procedure

The general procedure followed for all measurements will be described here. The procedure was the same whether the sample was superconducting or metallic.

The sample was attached to the underside of the mounting block of the sample gantry in the cryostat (see figure 4.3) with a small amount of vacuum grease. The cryostat was pumped to $\sim 10^{-6}$ torr and mounted onto a liquid nitrogen storage dewar. The cryostat

was cooled initially by opening the needle valve and drawing liquid nitrogen through the heat exchangers rapidly by pumping with a large mechanical pump. After about 45 minutes, when the cryostat had reached approximately 77 K, the flow of the nitrogen was reduced by closing the needle valve and regulating the pressure of the escaping nitrogen gas. This controlled the temperature of the upper exchanger (and hence the curved mirror of the resonator) to within 69–69.6 K (for all measurements used here). Having three independent controls on the temperature (pressure of the exit gas, throttle valve outside the cryostat, and needle valve inside the cryostat) meant that there were more controls than actually needed, and the same temperature could be reached for various flow rates. In most runs, the minimum flow rate was used.

The temperature of the sample was measured and controlled using a resistance bridge (made by the U.B.C. physics electronics shop) connected to a Lakeshore CERNOX resistance temperature sensor. The thermometer, and another resistor used as a heater, were attached to the sides of the sample mounting block. The temperature gradient between this block and the rest of the experiment was maintained across the two stainless steel plates supporting the block. There were no noticeable temperature gradients between the sample and the block, which was verified by mounting a diode on the sample block in the same manner as a sample. The temperature as measured by the diode corresponded closely to the temperature of the Lakeshore thermometer.

Once the apparatus had cooled, the frequency of the source was set to a constant value (normally $f_{MOD} \sim 1200$ MHz) and the vertical position of the sample was varied until a resonant mode was found (by noting both a rapid change in phase and an increase in the amplitude of the received signal by the lock-in amplifier). It was difficult to determine in advance what setting of the sample–mirror separation would give a resonant frequency within the bandwidth of the apparatus. This is due to the samples having varying thicknesses, and due to the thermal contraction of the gantry. Once a resonant mode was

found, the choke flanges were adjusted to give the best signal. In the current apparatus, it is difficult to do this prior to cooling, since the transmitted signal for a high temperature superconductor sample at room temperature was undetectable (the Q was so low). The procedure was repeated, scanning for other modes of the cavity, once the choke flanges have been adjusted to give good transmission.

The same mode of the resonator has been used for all the experiments described here. It is identified by various methods: its “distance” from other modes (both in frequency and mirror separation), its peak signal strength (largest of any mode observed), and the behaviour with respect to changing the frequency components making up the feeding signal (since I use the sideband where $f_{RES} = 8 \times f_{SYN} + f_{MOD}$, then increasing f_{SYN} should lower f_{MOD} at resonance, and vice versa). It is, nevertheless, difficult to make a precise identification with the modes shown in figure 4.4 for two reasons: firstly, because the measurement of the separation between the sample and the curved mirror is relatively imprecise; secondly, the equations defining the resonant frequency do not take into account such perturbations as the finite size of the surfaces, the effect of the coupling holes or ohmic losses of the mirrors on the resonant frequency. The result is that one usually doesn’t know the exact resonator mode. Using the resonator at room temperature and probing the field with a point dielectric perturbation (a small drop of epoxy on a monofilament thread), we were able to show that there were no nodes in the transverse field profile for the mode used. From the evidence, we judge that the resonator is most likely operating in the TEM_{0014} or TEM_{0015} mode. A more conclusive study of the mode pattern could be accomplished by scanning the resonator across the surface of an object with a clearly defined transition in surface resistance, such as a bi-metallic (brass / copper) surface. This was attempted early on, but the results were inconclusive due to limited resolution (the resonator was at room temperature, and the experimental techniques not yet refined).

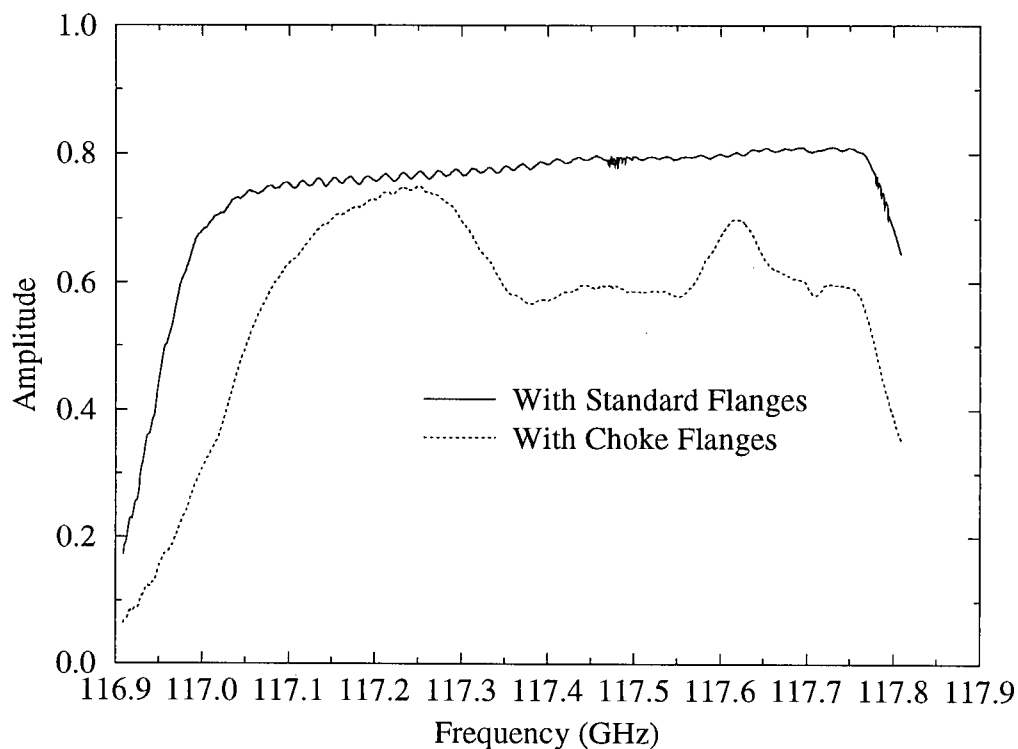


Figure 5.2: Comparison of the detected signal amplitude for direct transmission (*ie.* no resonator) for standard flanges and choke flanges.

A comparison of the signal obtained with no resonator or choke flanges (direct waveguide connection) against the signal obtained with no resonator but with choke flanges is shown in figure 5.3. As can be seen, the transmission amplitude is quite flat, with only small ripples as a function of frequency. The choke flange transmission is considerably poorer, and is very sensitive to misalignment. This is something that must be remedied in future versions of the apparatus.

Once the proper mode of the resonator was found and the flanges aligned, the Q of the resonator is found as a function of sample temperature. The vertical adjustment is set so that, at the lowest temperature (~ 70 K), the resonant frequency f_{MOD} is 1210 to 1215 MHz. The same approximate frequency was used to avoid any systematic errors which may occur when operating at different regions within the bandwidth of the

millimeter-wave system.

The source frequency is swept over the resonant frequency under computer control in 50 to 100 steps with the amplitude signal from the lock-in amplifier being recorded at each point. It was found that the sweep time (how long the computer paused with each data point) affected the value received for the Q . Fast sweeps gave low Q 's, which increased as the sweep time lengthened. The experiment was operated in the regime where the Q 's received were asymptotically close to the limiting value. This effect was due to the slow response time of the lock-in amplifier. Though a slow scan of frequency as performed here will be more susceptible to drift in the apparatus (due to changing temperature etc.), this effect was not noticeable within one scan of the frequency when the nitrogen pressure was regulated (though there is a significant drift in the frequency over the course of an experiment - see later). The data was collected on an Intel 286 computer (as described in chapter 4) and transferred to a Sun Sparc workstation for analysis.

The Q of the resonator was found by fitting the amplitude vs. frequency data to an appropriate function through a least-squares method. If we were measuring the power transmitted through the resonator, we would expect a Lorentzian relation between power and frequency about the resonant frequency. In this experiment, however, one is measuring the amplitude of the microwave signals which are proportional to $\sqrt{\text{Power}}$. There was a significant background noise associated with the signal; including random fluctuations, as well as directly transmitted signal (leakage through isolators, direct transmission between coupling holes in the cavity, and/or leakage from lower frequency portions of the circuit). In addition, the gain of the source/detection circuit was not necessarily uniform over the frequency range. Thus the amplitude vs. frequency was fitted to a function of

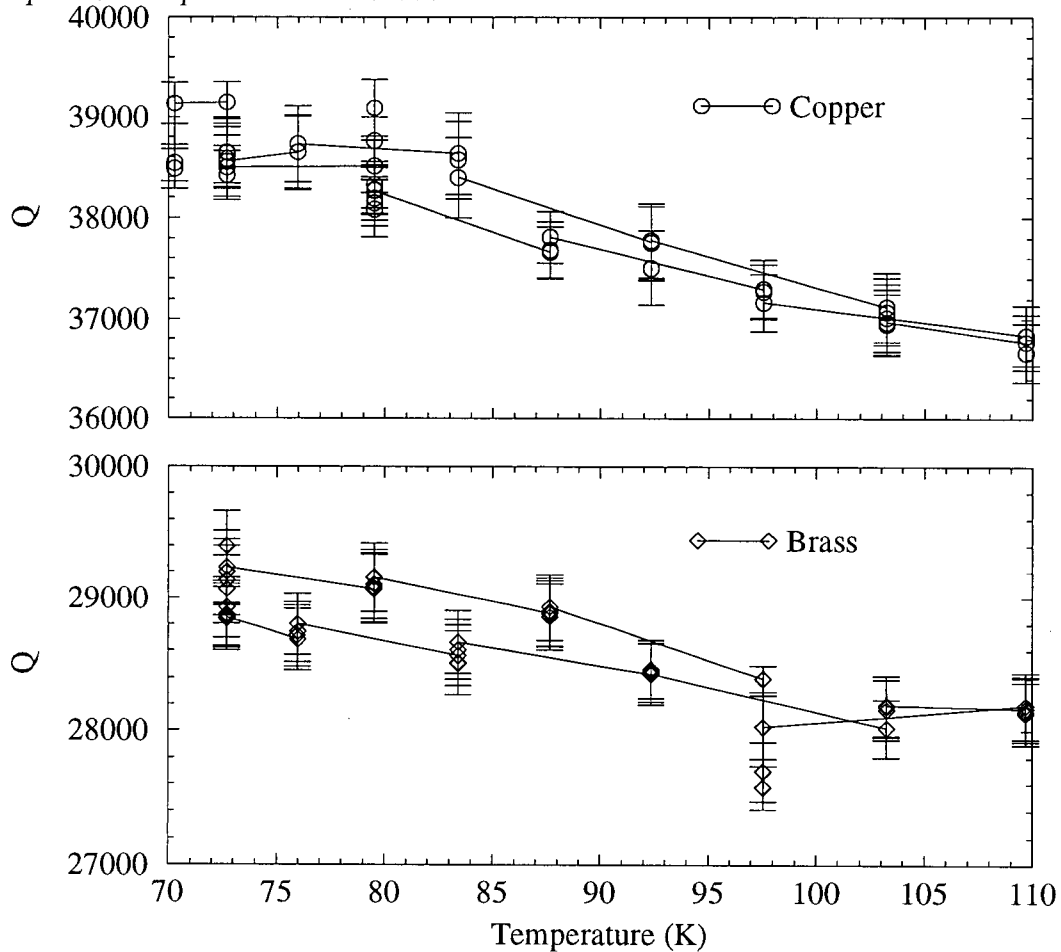


Figure 5.3: Q vs. temperature for brass and copper. The lines join the points in the order the data was taken.

the form:

$$V = \frac{A + B\nu}{\sqrt{1 + \left(\frac{\nu - \nu_0}{\Gamma}\right)^2}} + D + E\nu. \quad (5.2)$$

This was intended to account for both the background (linear) as well as variation in the gain source/detector pair with frequency (linear as well).

The fitted results for the resonant frequency and Q of the resonator with copper and brass as a function of temperature are shown in figures 5.3 and 5.4. In both cases, the lines join points taken in chronological order. Thus one can follow the drift in frequency over time in figure 5.4, although there is a much smaller corresponding drift in Q . The error bars shown are from the least-squares fitting, assuming equal error for each data

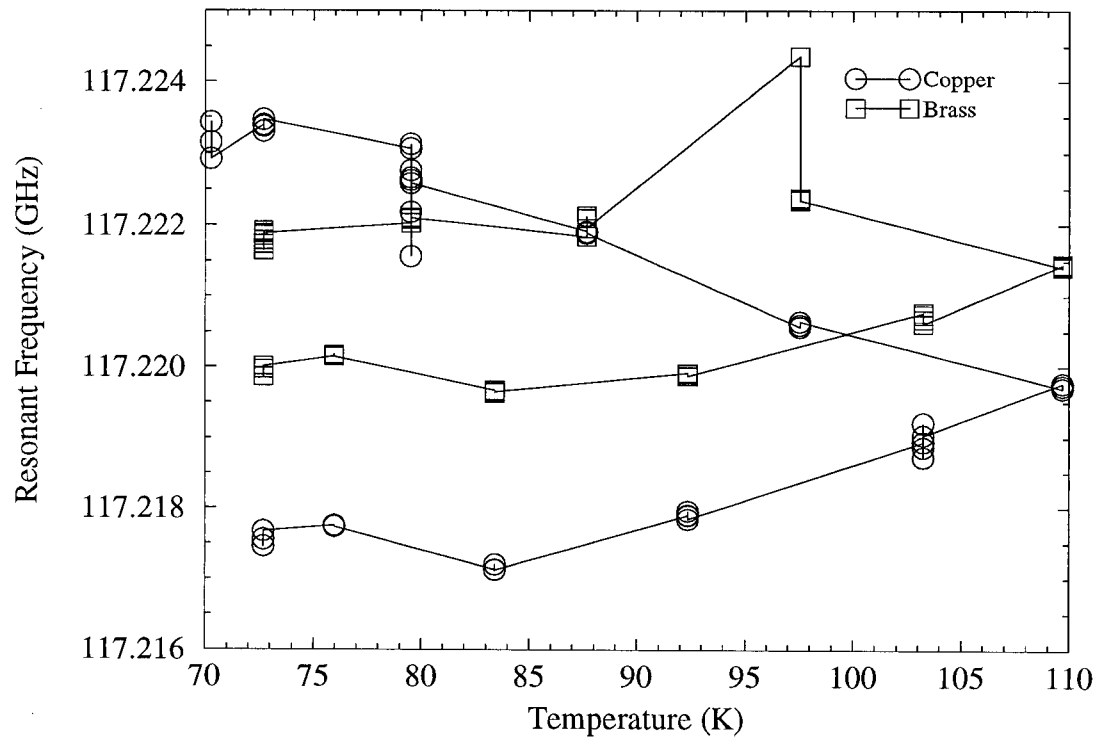


Figure 5.4: Resonant frequency as a function of temperature for brass and copper. Again, lines join points chronologically, and show clearly the drift in frequency with time of about 5 MHz. Error bars from the fits are smaller than the symbols on this graph.

point [36].

Various functional forms were compared in the fitting both for a single resonant peak, and also over a full experiment (see figures 5.5, 5.6, 5.7 and table 5.1). The final function chosen has the lowest χ^2 in most cases. Perhaps even more importantly, the Q displays little change with frequency (drifting over time), unlike the other functions (see figure 5.7). This is due to the asymmetric gain in the fitting function corresponding more closely to the actual behaviour of the experiment. Clearly, it would be better to have a flat gain over the bandwidth of the system, but modeling the asymmetry of the gain is an interim solution. The earlier version of the experiment where thermal expansion effects were rather large produced results of dubious validity.

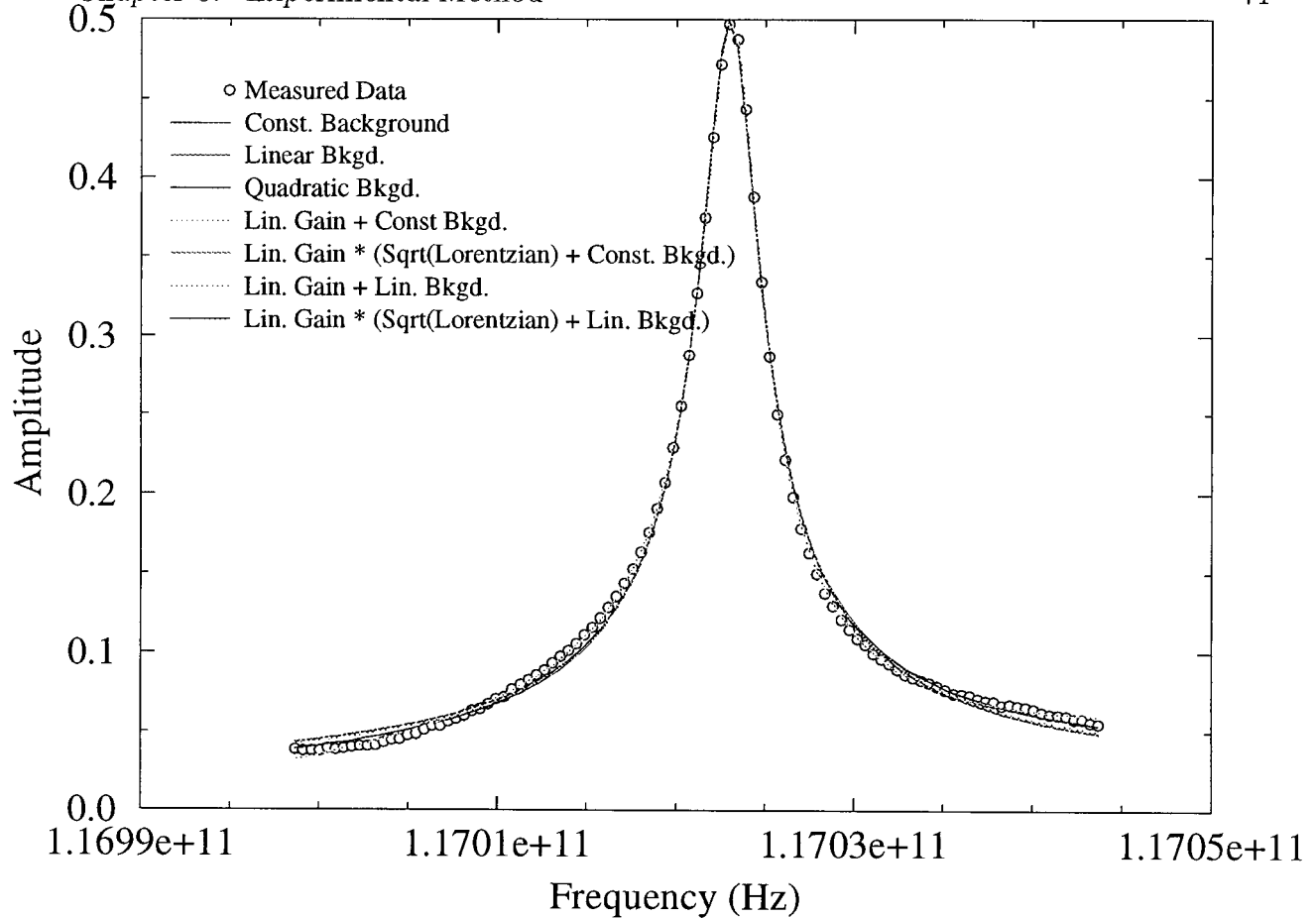


Figure 5.5: Comparison of the various fitting functions with the measured data. The data in question is for copper at 70 K and represents a “good” peak — where the amplitude and Q are both quite high. The functions are described in more detail in table 5.1.

The data in figure 5.3 are fit to the equation

$$\frac{1}{Q_{Brass}} - \frac{1}{Q_{Copper}} = \alpha(R_{S_{Brass}} - R_{S_{Copper}}) \quad (5.3)$$

to get the proportionality constant α . The result is then inserted into equation 5.1 to find the sample-independent loss β . The result of the fit is shown in figure 5.8. The values of the fitting constants received are

$$\alpha = (7.45 \pm 0.32) \times 10^{-5} \Omega^{-1} \quad (5.4)$$

and,

$$\beta = (2.334 \pm 0.024) \times 10^{-5}. \quad (5.5)$$

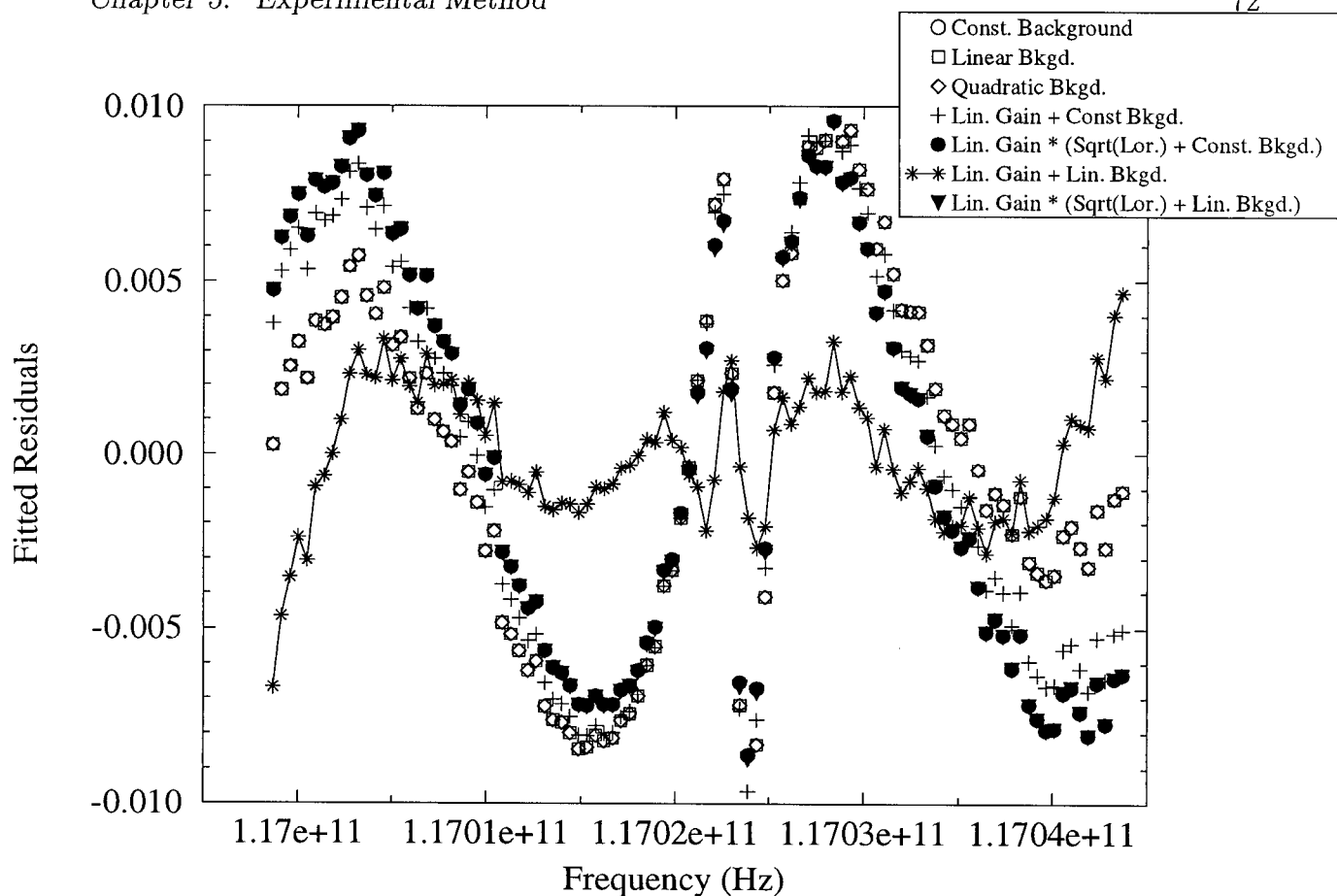


Figure 5.6: Residuals of the fitted peak for the various functions used. The curve used for data analysis is shown with the points joined.

The uncertainty in these values includes both the uncertainty in the measurement of Q for each point, and the uncertainty in fitting the two experiments to the d. c. data. No systematic error is included in the uncertainties.

Function	ν_0	χ^2	Q
$\frac{A+D\nu}{1+(\nu-\nu_0)^2/\Gamma^2} + B + C\nu$	$117.0231090 * 10^9$	0.0003902	38481 ± 194
$\frac{A}{1+(\nu-\nu_0)^2/\Gamma^2} + B$	$117.0229941 * 10^9$	0.003456	37759 ± 560
$\frac{A}{1+(\nu-\nu_0)^2/\Gamma^2} + B + C\nu$	$117.0229815 * 10^9$	0.002665	37759 ± 499
$\frac{A}{1+(\nu-\nu_0)^2/\Gamma^2} + B + C\nu + D\nu^2$	$117.0229815 * 10^9$	0.002665	37999 ± 496
$\frac{A+D\nu}{1+(\nu-\nu_0)^2/\Gamma^2} + B$	$117.0229809 * 10^9$	0.003364	37792 ± 554
$(1 + C\nu) \left(\frac{A}{1+(\nu-\nu_0)^2/\Gamma^2} + B \right)$	$117.0229941 * 10^9$	0.003456	37758 ± 554
$(1 + D\nu) \left(\frac{A}{1+(\nu-\nu_0)^2/\Gamma^2} + B + C\nu \right)$	$117.0229941 * 10^9$	0.003456	37759 ± 564

Table 5.1: Comparison of (some of) the fitting parameters for various functions, as shown in the accompanying figures. This is for a particular scan of copper at 71 K. The first line of the table shows the function used in all subsequent work.

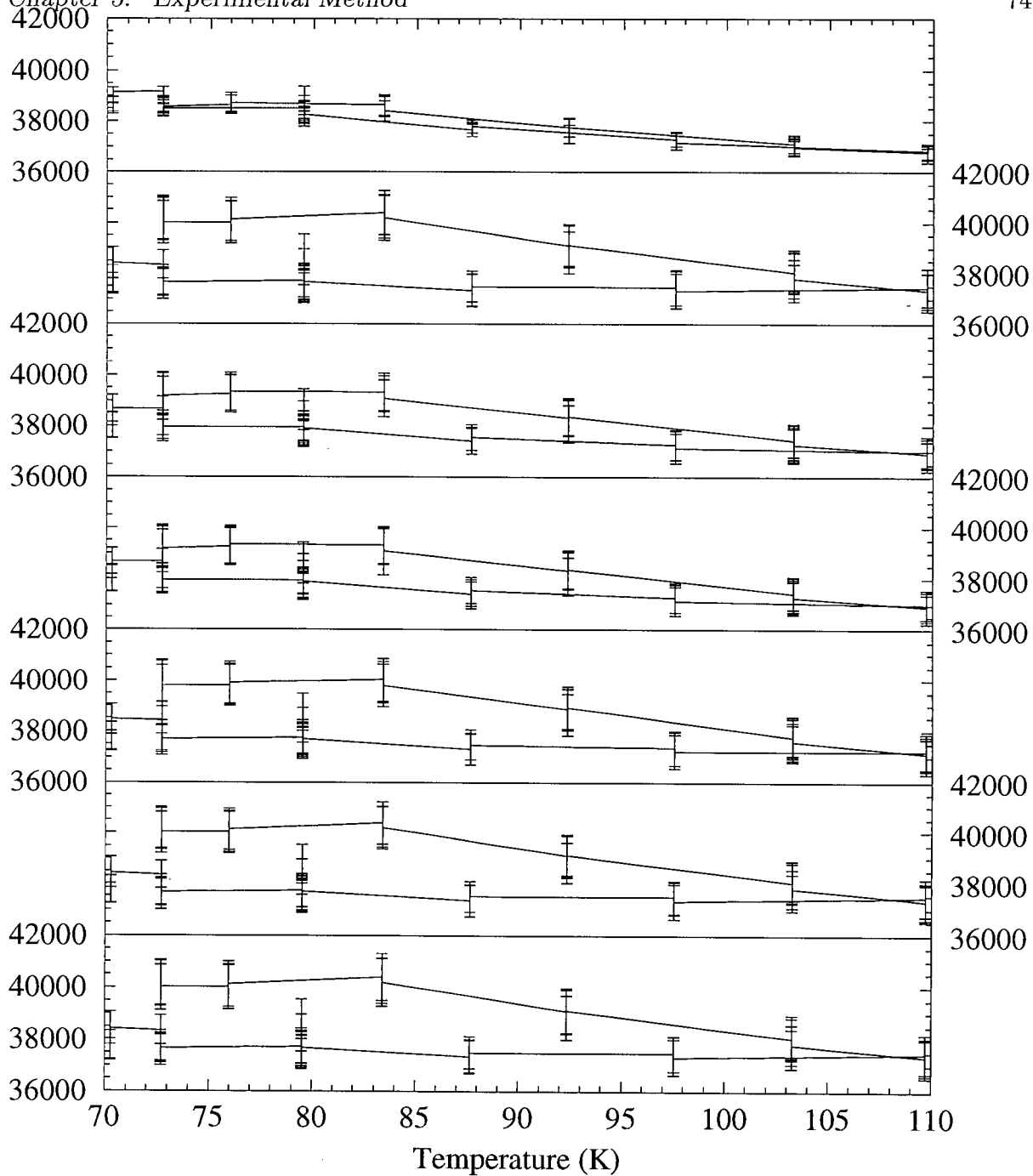


Figure 5.7: Comparison of Q vs. temperature for copper using various fitting functions, with the points connected in the order the data was measured. The functional form used is in the top graph, the other graphs use the functions in the same order as table 5.1. Note how the uncertainty is much smaller, and the drift with time is reduced in the first graph.

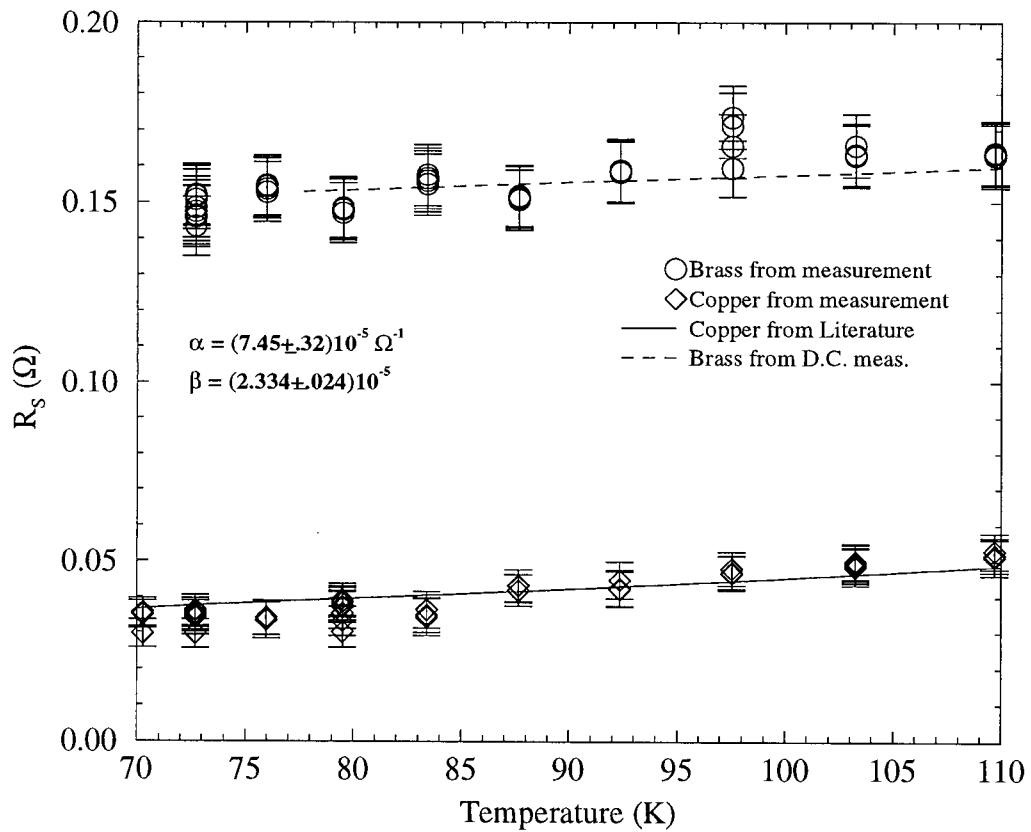


Figure 5.8: The cavity perturbation data measurements of R_S of copper and brass at 117 GHz fitted to values obtained from the literature and d.c. measurements. The fitted values of the constants α and β as determined from this data are shown in the figure, and their uncertainty has been added to the error bars as shown.

Chapter 6

Data

6.1 Introduction

In this chapter the measurements of surface resistance performed to date using the open resonator will be presented. These samples were available to our lab in November and December 1994, and are actually a good survey of the capabilities of the apparatus. There are, however, no “state of the art” thin films yet available in the group, which might push the limits of the resolution of the apparatus. In fact the problem is the opposite: the surface resistances of the films are high enough that the Q of the resonator is quite low, and the transmission through the resonator very small.

Measurements above the transition temperature are lacking for two reasons: first of all the loss of a high temperature superconducting thin film in the normal state is quite large, which reduces the Q of the resonator, and the transmitted signal becomes too small to measure. A related problem, of the enhancement of loss when the skin depth is large, will be discussed later in the chapter. The second reason is that the sample thermometer had been calibrated incorrectly, and when the sample was thought to be above T_C , it was in fact 4 K lower. This problem has since been corrected, and the existing data re-analysed, however no new data has been taken.

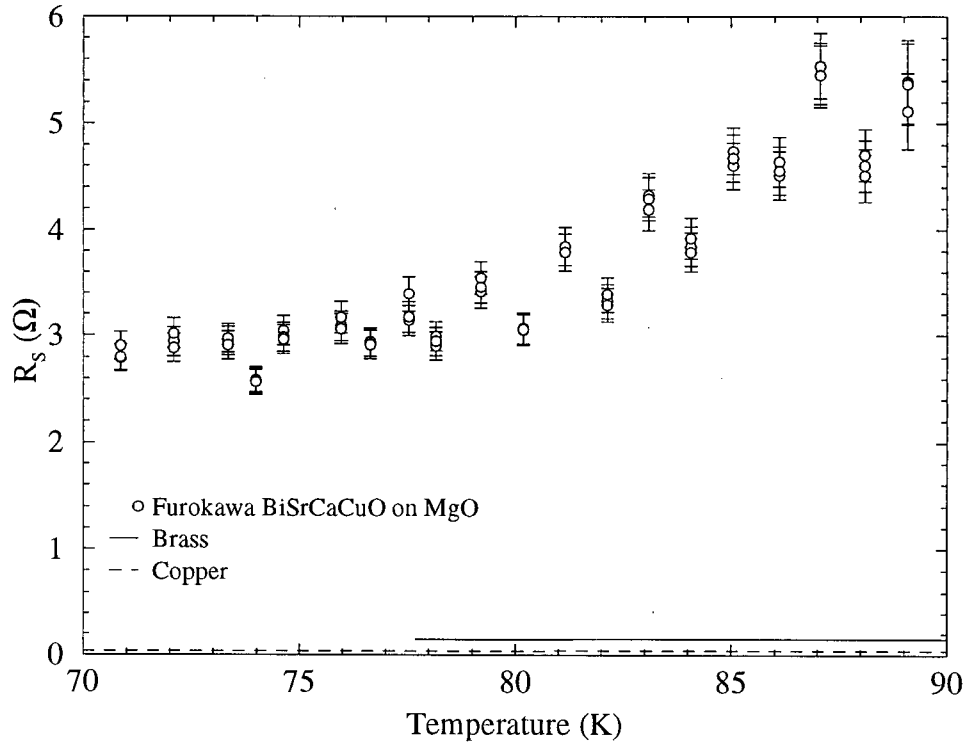


Figure 6.1: The temperature dependence of the surface resistance of a $6 \mu\text{m}$ thick BSCCO thick film on an MgO substrate. The surface resistance of copper and brass are included for comparison.

6.2 Data

6.2.1 Furukawa Electric $\text{Bi}_2\text{Sr}_2\text{Ca}_1\text{Cu}_2\text{O}_8$ Thick Film

Figure 6.1 shows the surface resistance *vs.* temperature of a thick film of $\text{Bi}_2\text{Sr}_2\text{Ca}_1\text{Cu}_2\text{O}_8$. The film is deposited through a silk-screen-like method on an MgO substrate by the Furukawa Electric Company. Unlike the other films studied here, this film is not of YBCO, but of BSCCO, a material which hasn't been studied as extensively in the microwave/millimeter-wave region. The film is also quite thick, at $6 \mu\text{m}$, and has visible patterns on the surface, suggesting multiple grains as well as roughness. To avoid measuring this very rough layer, which would scatter the radiation and lower the resolution,

the sample was placed with the film side towards the mounting block (*ie.* away from the curved mirror). As a consequence the fields must penetrate through the substrate. This change will have a number of effects:

- the dielectric constant of the MgO ($\epsilon_r = 16$ at 10GHz [6]) will cause the effective size of the resonator to be larger, possibly shifting modes.
- the dielectric loss of the substrate ($\tan \delta = 6.2 \times 10^{-6}$ [6]) will lower the Q of the resonator.
- reflection will occur from the substrate-air interface as well as from the substrate-film interface. The effective resonator length for the substrate-air surface will not be resonant, and so will scatter the energy and lower the measured Q .
- any change of these parameters with temperature will give a contribution to the Q which will be indistinguishable from properties of the superconductor itself.

To avoid, or at least account for, these problems the substrate should be measured with a known surface below (such as copper). This has not yet been done.

The surface resistance as measured is very high. This may be due to the substrate, but it is very likely due to the properties of the film itself. To have low surface resistance, the crystallinity of the superconductor needs to be very high. This measurement is a non-local probe of the material, so a film which shows zero d.c. resistivity may only have small connected superconducting sections, and show high surface resistance. The appearance of the film, and the manner in which it was fabricated, suggest problems of this sort.

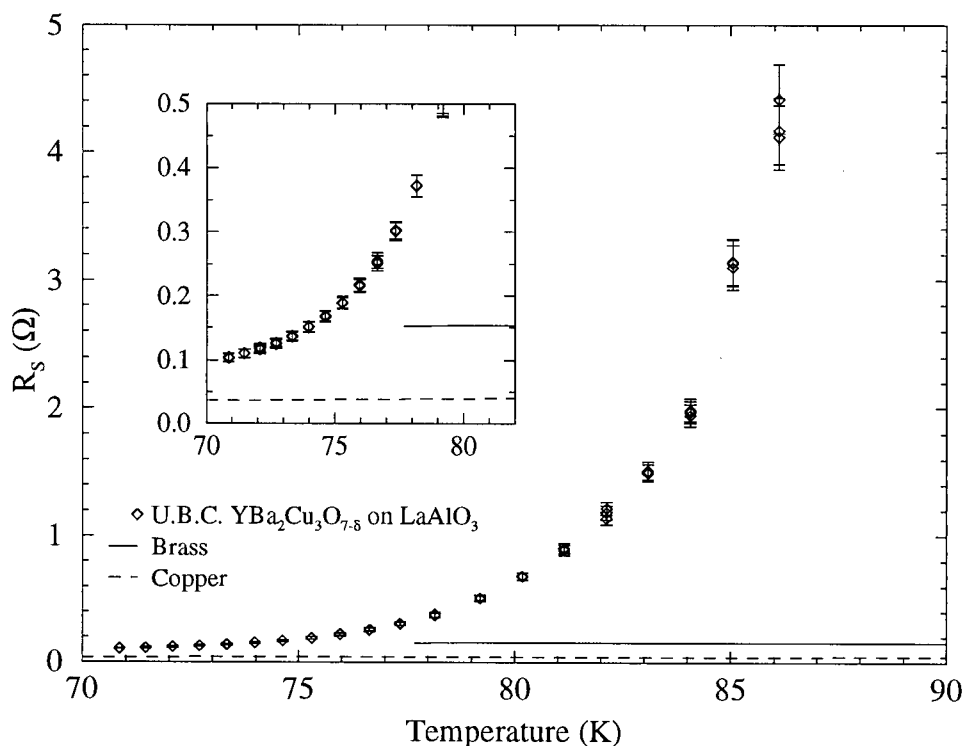


Figure 6.2: The temperature dependence of the surface resistance of a thin film of $\text{YBa}_2\text{Cu}_3\text{O}_{7-\delta}$ on an LaAlO_3 substrate.

6.2.2 U.B.C. $\text{YBa}_2\text{Cu}_3\text{O}_7$ film on LaAlO_3

This $\text{YBa}_2\text{Cu}_3\text{O}_{7-\delta}$ film was grown by André Wong in the U.B.C. physics department using pulsed laser ablation [61] (film AW1107). This technique produces highly epitaxial films on a number of substrates, in this case on LaAlO_3 . There are a large number of variables and procedures which must be optimized to give this good epitaxy and crystallinity of the film. The films measured here which were grown at U.B.C. have not reached optimal properties, and show a T_C of approximately 85–88 K.

This film shows a rapid decrease in the surface resistance with temperature, reaching 0.1Ω surface resistance at 71 K. This is the lowest surface resistance of the four films measured here, though it is still about twice the loss of copper at the same temperature. As mentioned before, this film was not measured over a wide enough temperature range

to find the transition temperature — though the resolution of the apparatus was very poor at ~ 86 K where the measurements stopped. It is encouraging that the surface resistance was still decreasing when the lowest temperature was reached, but its high value and the low transition temperature suggest further work must be done to improve the film growth procedure. The thickness of this film has not been measured, but the growth time and conditions used give a value of about 3500\AA . This thickness is comparable to the penetration depth of the superconductor in the temperature range of the experiment. The derivation of the surface resistance in chapter 1 assumed that the thickness superconductor was much greater than the penetration depth, and thus is not appropriate in this case. The effective surface resistance of such thin films will be discussed in section 6.3.

6.2.3 U.B.C. $\text{YBa}_2\text{Cu}_3\text{O}_7$ film on SrTiO_3

This sample is another thin film of $\text{YBa}_2\text{Cu}_3\text{O}_{7-\delta}$ (figure 6.3) grown by André Wong at U.B.C. using pulsed laser ablation. This sample, however, was grown on a substrate of SrTiO_3 , which probably accounts for the unusual behaviour observed for the temperature dependence of the surface resistance.

Strontium Titanate (SrTiO_3), is a ferroelectric material, which exhibits change in the relative permittivity between 300 at room temperature and 20000 at 4.2 K [62]. If any radiation is transmitted through the film then resonances can be established between the film and the copper mounting block. This will be discussed in section 6.3. It is, therefore, difficult to estimate the actual surface resistance of this sample. For this reason superconducting films on SrTiO_3 are not often used for high frequency applications. This is unfortunate, since SrTiO_3 is a substrate with very good lattice match to YBCO, and does not exhibit twinning (unlike LaAlO_3)[6].

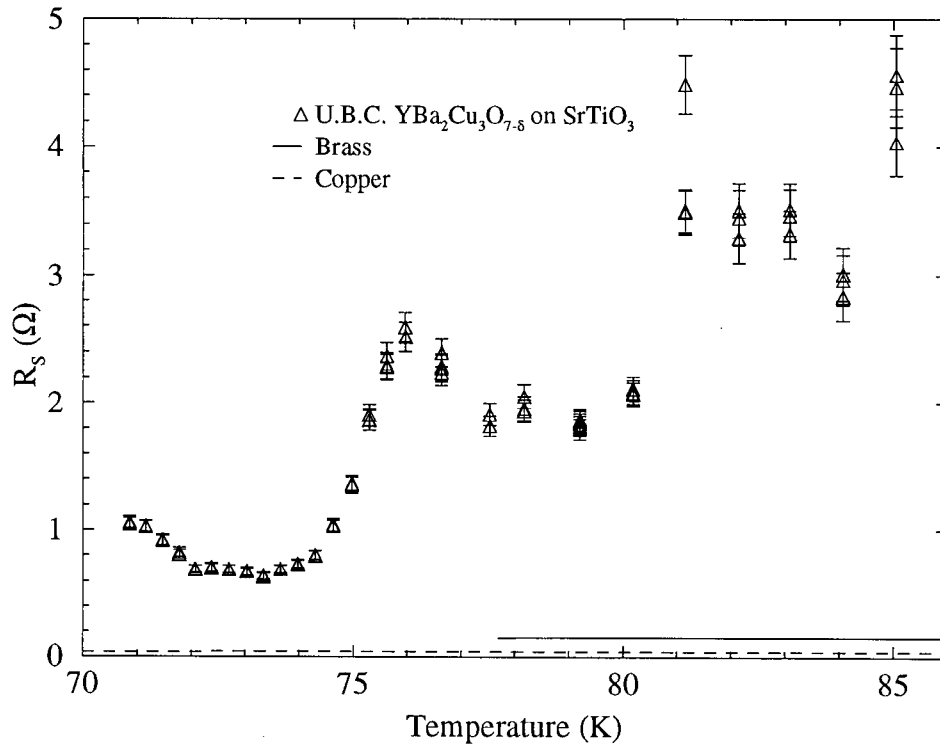


Figure 6.3: The temperature dependence of the surface resistance of a thin film of $\text{YBa}_2\text{Cu}_3\text{O}_{7-\delta}$ on an SrTiO_3 substrate.

6.2.4 McMaster $\text{YBa}_2\text{Cu}_3\text{O}_{7-\delta}$ 10000Å film on LaAlO_3

This is another film of $\text{YBa}_2\text{Cu}_3\text{O}_{7-\delta}$ grown by pulsed laser ablation on LaAlO_3 (see figure 6.4). This film was grown at McMaster University through a process which has been well optimized to produce films of high epitaxy and crystallinity. This film, however was quite thick ($1 \mu\text{m}$), and there were problems associated with this. This film shows a sharp drop in R_s below T_C , but levels out before 80K at a level of about 0.15Ω .

The growth of thicker films is currently the subject of substantial research, since thicker films are able to carry a larger amount of current, useful for high power applications. All substrates currently in use have a lattice parameter that is slightly different from that of $\text{YBa}_2\text{Cu}_3\text{O}_{7-\delta}$. As the film thickness is increased, the strain that is induced by this lattice mismatch causes dislocations, grain boundaries and other defects in the

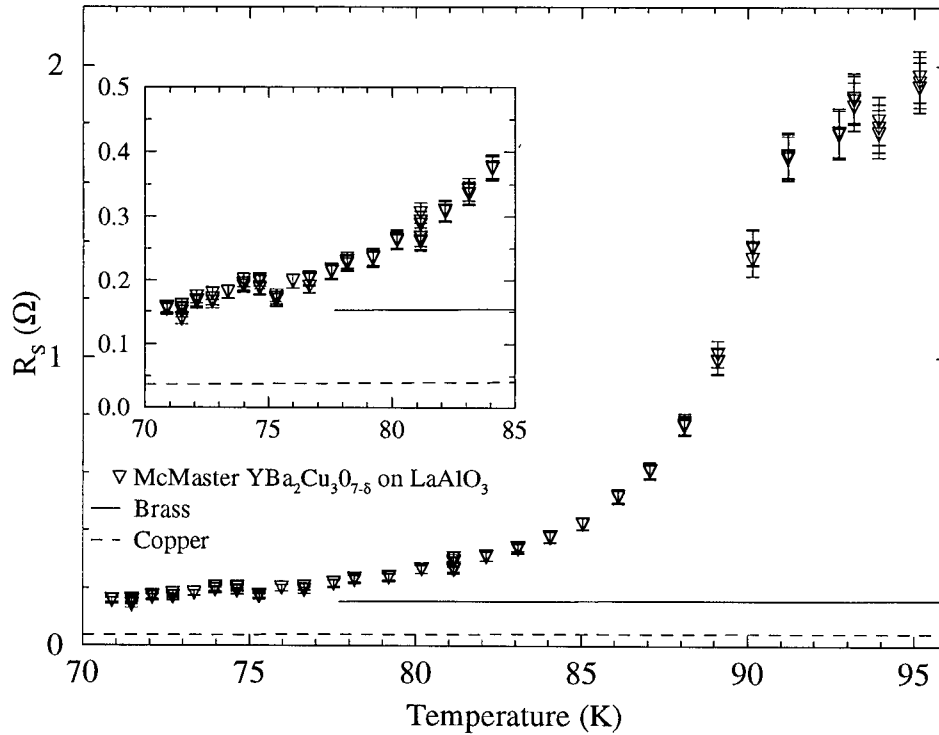


Figure 6.4: The temperature dependence of the surface resistance of a 10000\AA thick film of $\text{YBa}_2\text{Cu}_3\text{O}_{7-\delta}$ grown at McMaster University on an SrTiO_3 substrate.

film. These defects tend to increase the surface resistance. Work is progressing both in the development of new substrates with a reduced lattice mismatch, as well as in the techniques needed to grow films of a thickness of about $1\ \mu\text{m}$.

The surface resistance of this film was measured by Dr. Doug Bonn at U.B.C. as well, using a 3.7 GHz resonant cavity method [14]. Unfortunately, the surface resistance showed a strong dependence on the power of the excitation, suggesting weak links in the sample and precluding further measurements. The presence of weak links is consistent with current problems in growing thick films, as described above. Unfortunately, the open resonator described here does not have the capability of examining the power dependence of the surface resistance, in order to determine if such weak links exist.

Another film grown at McMaster University by the same process was measured by

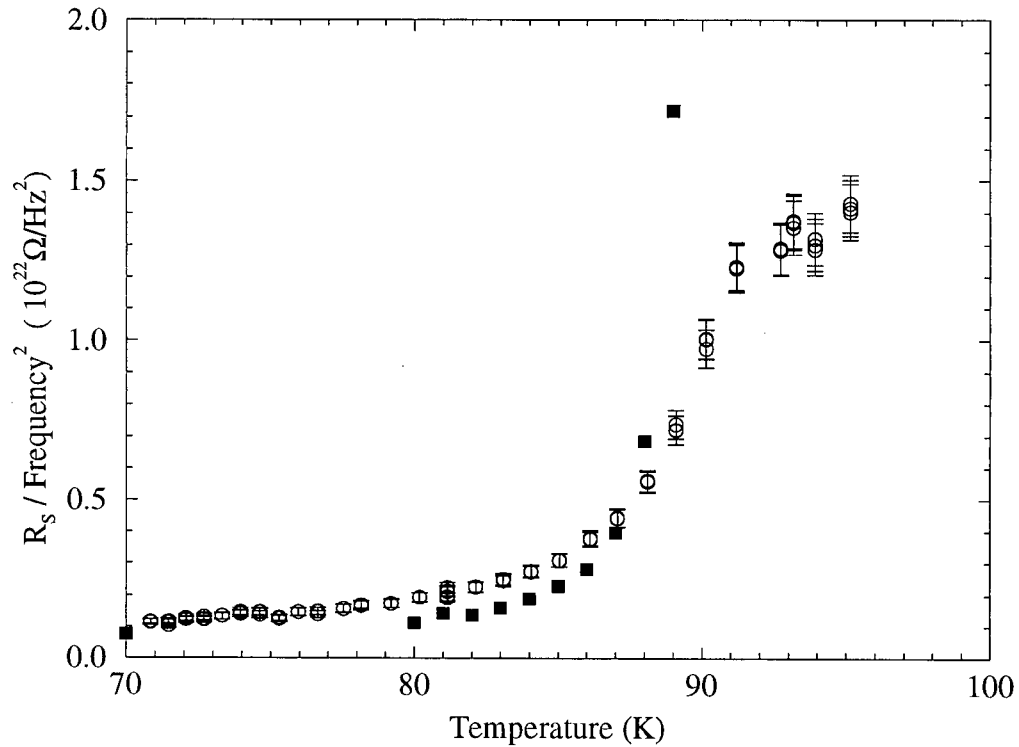


Figure 6.5: The temperature dependence of the surface resistance of two McMaster films (solid squares: 3000Å thick, open circles: 10000Å thick). The thinner film was measured at 3.7 GHz and the thicker at 117 GHz using the open resonator. The data are scaled by the frequency squared, according to the two-fluid model. This scaling is not appropriate for the normal state, which accounts for the discrepancy near T_C .

Dr. Bonn. This film had a thickness of 3000 Å, and showed a very low surface resistance (approximately 10^{-4} Ω below 70K at 3710 MHz). A comparison of this film with the data in figure 6.4 is shown in figure 6.5. The data are scaled by the frequency squared, to account for the dependence of R_S on frequency. The data are quite comparable, with the (scaled) R_S of the thin film only slightly lower than that of the 10000Å film. The frequency scaling may actually be weaker than ω^2 , since the two-fluid model used to derive it is only approximate. Further study is needed to determine the frequency response of both films and crystals.

The McMaster film measured by the open resonator, does however show a clear T_C ,

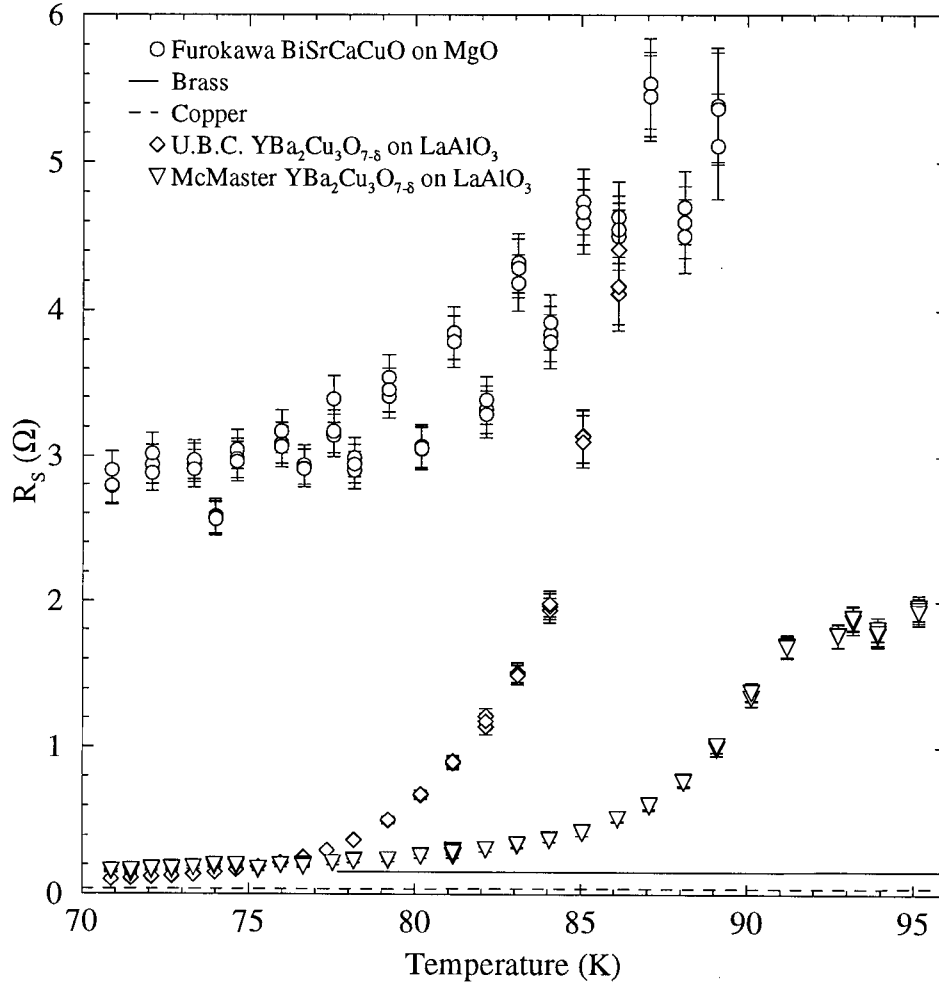


Figure 6.6: The surface resistance of the superconducting films described earlier shown on the same plot for comparison. The surface resistance of the film grown on SrTiO₃ is not included, both for clarity and because of the systematic substrate problem.

unlike the others. This is most likely due to the fact that the film is thick, thicker in fact than the skin depth of the material in the normal state. This allows measurements above the transition temperature to be made with acceptable accuracy. In fact, it was the initial measurement of a transition at 96K that alerted us to the mis-calibration of the sample thermometer.

6.2.5 Comparison

As mentioned earlier, the limited data obtained so far cannot be considered to be the basis of an exhaustive study. Trends in the data can be seen quite clearly, however:

- The surface resistance of the thick BSCCO film is very high, and this film is not suitable for microwave work.
- The films grown on LaAlO_3 show the best microwave performance.
- The effect of the changing dielectric constant of SrTiO_3 makes its use as a substrate for high-frequency superconducting circuits limited.
- The surface resistance of the McMaster film is lowest at high temperature, but reaches a limiting value that is quite high ($.15 \Omega$) at about 75 K.
- The surface resistance of the U.B.C. film grown on LaAlO_3 drops rapidly around 85K, and continues to drop below the temperature range accessible in the measurement.

The continuing decrease in the surface resistance of the U.B.C. film on LaAlO_3 suggests that there are less defects present than in the McMaster film, though its low T_C may be due to reduced oxygen concentration. It is for measuring properties such as these that this apparatus has been designed, and a systematic study would be fruitful. The work done by many researchers in improving the crystallinity of thin films in order to reduce the surface resistance contrasts with the studies done in this lab suggesting a certain level of defects reduce the surface resistance [63]. The cause of this discrepancy, that the lowest R_S is obtained in films by striving to remove all defects, while in crystals by adding defects, is currently unknown. It is possibly due to the nature of the defects; that dislocations and twins increase the surface resistance, while substitutional disorder can lower it.

Included here for comparison is a graph showing the surface resistance of thin films of YBCO at 77K *vs.* frequency (figure 6.7). This graph was taken from a paper published in 1992 [6], with much of the data older than this, however data from more recent publications is quite similar.

6.3 Finite Thickness Effects

The surface resistance of the films as measured is likely to be dominated by extrinsic effects such as defects. There is, however, an extrinsic effect for which we can correct: the effect of the finite thickness of the film. Thin films of superconductors are grown to a few thousand angstroms thick — about the same size as the penetration depth in the material. Thus the assumption of infinite thickness in the derivation of the surface resistance in chapter 1 is not justified. Thus the effect of the reflection of the electromagnetic energy off the backside of the film, as well as of transmission completely through the film, can no longer be ignored.

The effective surface impedance of a film of thickness d for penetration depth λ on a substrate of infinite thickness of relative permittivity ϵ_r is given by [62]:

$$R_{\text{eff}} = R_S f(d/\lambda) + R_{\text{trans}} \quad (6.1)$$

$$X_{\text{eff}} = X_S \coth(d/\lambda) \quad (6.2)$$

where

$$f(d/\lambda) = \coth(d/\lambda) + \frac{d/\lambda}{\sinh^2(d/\lambda)}$$

$$R_{\text{trans}} = \epsilon_r^{1/2} \frac{(\omega\mu\lambda)^2}{Z_0} \frac{1}{\sinh^2(d/\lambda)}$$

where Z_0 is the impedance of free space (377 Ω). These equations are derived by considering both the reflection and transmission from both the top and bottom of the film. This is done conveniently through impedance transformations, as described thoroughly

in the reference [62]. The function $f(d/\lambda)$ is the enhancement of the loss in the film. This occurs because the current density excited in a film of finite thickness are greater than for an infinitely thick superconductor. The transmitted energy is described by the term R_{trans} . This term, in most cases, is smaller than the enhancement due to increased current. The situation is actually improved significantly by having the substrate backed by metal, as is the case in this apparatus (see figure 6.9). Here, almost almost all of the transmitted energy is reflected back by the metallic backing, rendering the R_{trans} term negligible.

When the thickness of the substrate (in between the film and the metallic support) resonates, the transmission which is normally negligible can have a significant effect. Such a resonance occurs when the thickness of the substrate D satisfies [62]:

$$D = n \frac{\lambda_0}{2\epsilon_r^{1/2}(T)}, \quad n = 1, 2, 3... \quad (6.3)$$

where λ_0 is the free-space wavelength of the radiation, and $\epsilon_r(T)$ is the relative permittivity of the substrate at temperature T . For most substrates, this would be a problem at only isolated frequency/thickness combinations. However, for SrTiO_3 the temperature dependence of the permittivity is dramatic. Here a series of resonances can occur within a temperature sweep. Off resonance, the transmitted radiation is reflected back into the resonator, as described above. At resonance, the radiation will bounce back and forth between the conducting surfaces until it is dissipated. This explains the peaks and valleys observed in the temperature dependence of R_S of the YBCO film grown on strontium titanate (see figure 6.3). Klein *et. al.* [62] calculate the relative permittivity of SrTiO_3 using the positions of the minima of these resonances. This is only really possible at temperatures above T_C of the film, since the rapid change in R_S below T_C will distort the curve.

Near, and above T_C , where the penetration depth becomes large (and is replaced by

the skin depth), the finite thickness effect becomes more pronounced. The skin depth for a high temperature superconductor in its normal state is given by

$$\delta = \sqrt{\frac{2}{\omega\mu\sigma}} \quad (6.4)$$

as shown in equation 1.13. A typical d.c. resistivity in the normal state just above T_C of $\rho = 100\mu\Omega\text{cm}$ gives a skin depth of about 15000 Å. This is thicker than most thin films, causing the spurious increase in surface resistance noted before. It is for this reason that the apparent surface resistance becomes unmeasurably high in thin films of superconductor above T_C . This limitation is inherent in the measurement, and precludes accurate normal state measurements on thin films in this apparatus.

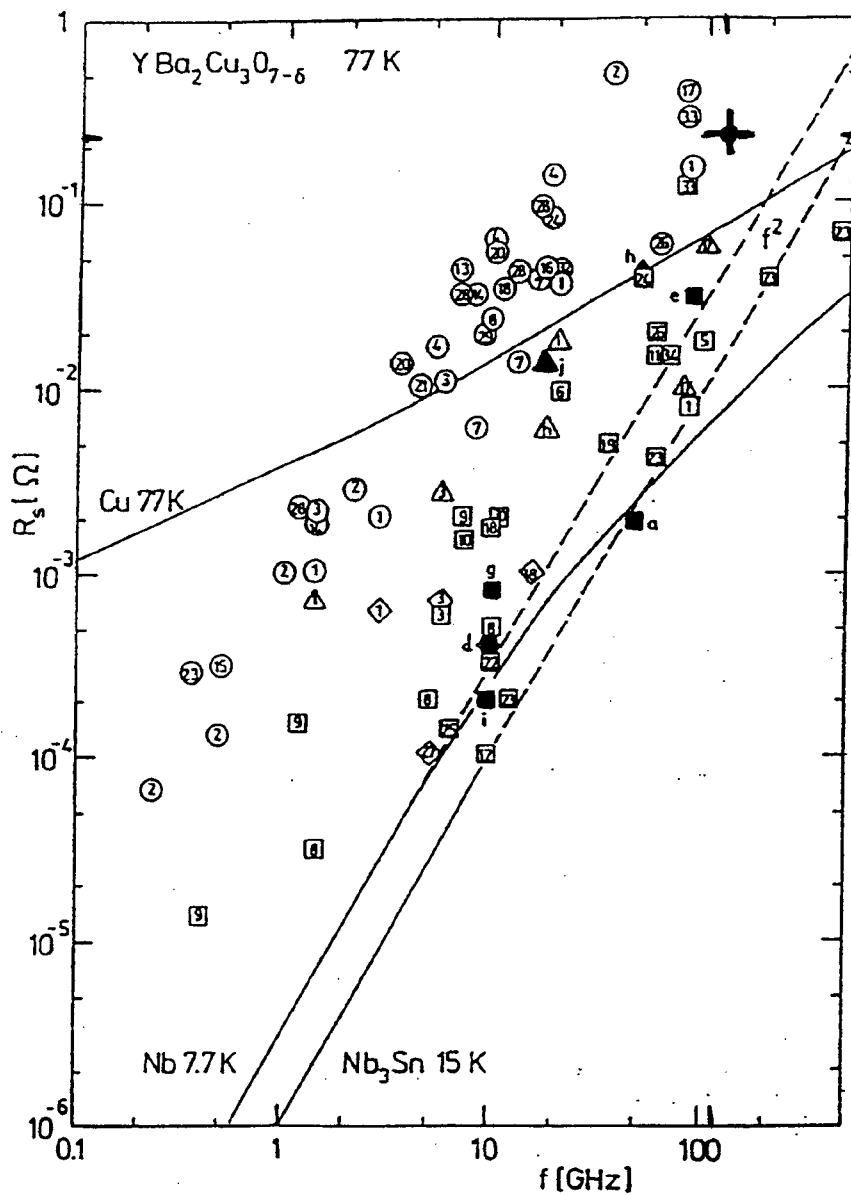


Figure 6.7: The frequency dependence of R_s of untextured (circles) and c-axis textured (triangles) polycrystalline bulk or thick film samples, as well as for epitaxial thin films (squares) and single crystals (rhombuses) of $\text{YBa}_2\text{Cu}_3\text{O}_7$ at 77K. This plot is taken from reference [6]. The cross in the upper right corner is the data for the McMaster film from this thesis.

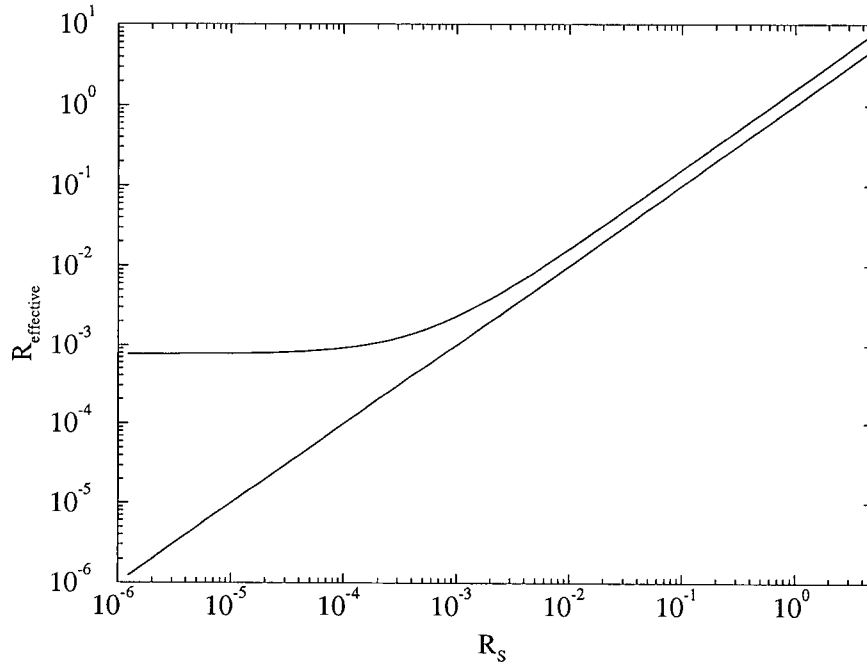


Figure 6.8: The effective surface resistance as a function of the intrinsic surface resistance for a film 3500\AA thick at 117 GHz assuming $\lambda = 2600\text{\AA}$ and $\epsilon_r = 16$ [62].

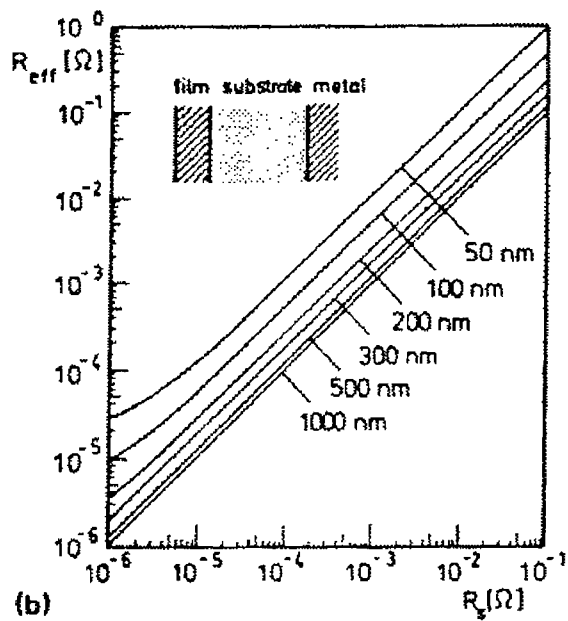


Figure 6.9: The calculated effective surface resistance for various thicknesses of film. This figure is reproduced from [62], and assumes $f = 87$ GHz, $\lambda = 2600\text{\AA}$ and the substrate with $\epsilon_r = 16$ is 1mm thick, backed by copper.

Chapter 7

Conclusions and Discussion

7.1 Introduction

The project described in this thesis has been successful in creating an apparatus to routinely evaluate the surface resistance of superconducting films. These measurements can be used as feedback to those involved in the deposition of these films, with the goal of lowering the microwave loss of the materials.

7.2 Equipment Performance

The apparatus as constructed, consisting of the cryostat, the millimeter-wave source / detector pair, and the resonator assembly, has been tested under a variety of conditions.

The cryostat's performance has been numerically modeled thoroughly for liquid helium cooling, and was designed based on this data. The cryostat has been operated numerous times using liquid nitrogen cooling, with good control of both the sample and base temperature from 70 to 120 K. This control was achieved using pressure regulation on the exit gas, as well as active control of the sample temperature using electronic regulation.

A swept millimeter-wave source and detector have been assembled using a previously built fixed-frequency spectrometer. The resulting system has a flat transmitted power over a 500 MHz frequency range around 117 GHz, with a peak detected signal of 200 mV, and a background noise level (due to leakage or random noise) of < 1 mV.

The resonator as designed has an unloaded Q with copper at 70K of 39000, and the system can handle a minimum Q of ~ 2000 . The resonant frequency is stable to within 4 MHz over 50 K changes in the temperature; this stability has required minimization of the effect of thermal contraction. With a data acquisition and analysis system that accounts for much of the asymmetry present in the gain of the millimeter-wave system, the Q and resonant frequency are fitted with good precision.

7.3 Surface Resistance Data

The apparatus has been used to measure the surface resistance of superconducting films as well as normal metals. The surface resistance of these normal metals has been used as a calibration of the geometrical factors and of the parasitic losses of the resonator. The fitted results show scatter, but well within the error bars as given by the χ^2 from the fit done to extract the Q .

The measurements on superconducting thin films give the variation of surface resistance *vs.* temperature from 70K to T_C of the film. Measurement of the normal state properties is only possible for thick films where the skin depth of the material in the normal state is less than the thickness of the film.

The films measured show a steep drop in R_S with temperature below the superconducting transition. This drop levels out in all the films below 80K, though R_S does continue to decrease slowly. None of the films measured have surface resistance lower than copper at the same temperature, as is expected at this frequency. None of the films measured show outstanding performance in comparison with the best of the literature data, indicating that further development work is needed.

The films grown on LaAlO_3 show the lowest surface resistance of those measured. The $\text{YBa}_2\text{Cu}_3\text{O}_{7-\delta}$ films, which were epitaxially grown, show much better microwave

performance than the thick $\text{Bi}_2\text{Sr}_2\text{Ca}_1\text{Cu}_2\text{O}_8$ film. The film grown on SrTiO_3 shows a complicated effect due to the temperature dependence of the permittivity of the substrate causing resonances in between the film and the copper mount. This dependence makes such films difficult to use for high frequency applications.

The effect of the finite thickness of the films is to increase the effective surface resistance depending on the ratio d/λ (the thickness of the film divided by the penetration depth). This effect is due to reflection off the rear surface of the film increasing the loss in the film. This effect is magnified near T_C where the penetration depth increases, and can lead to an effectively broadened transition. There is a small amount of transmission through the film, but it is negligible unless resonance occurs (as above for SrTiO_3).

The thickness of the film is also an important quantity in terms of growth: since thinner films seem to have better crystallinity and thus lower microwave loss. Thicker films have an inherently higher current carrying ability, and thus are desirable for high power applications. The improvement of film growth techniques to have thick films with low R_S is a goal of many researchers. Currently, the surface resistance of films has a minimum as a function of thickness, with the R_S enhancement limiting the utility of the thinnest films, and non-epitaxy limiting the utility of the thickest films.

7.4 Future Work

Future work on this apparatus will be greatly affected by a new millimeter-wave vector network analyzer which is expected to be delivered to the lab very soon. This network analyzer will allow more accurate measurements over a much wider range of frequencies. This should avoid any systematic shift in the Q with frequency due to asymmetry of the gain of the source/detector pair. However, many of the problems with the current

apparatus are due to the poor performance of the choke flanges, these should be re-designed for better uniformity of transmission over frequency, as well as for greater ease of use.

A new sample-mounting gantry should be built to provide:

- A smaller thermal conduction to the base, so that higher temperatures can be reached simply. This could also incorporate active sample cooling to reach the lowest temperatures (using liquid helium) without this large conduction currently present.
- A carrousel, so that multiple samples can be measured during the same run. This will allow both reference samples, and multiple unknown samples to be measured rapidly. This is important for routine measurements.
- Very small thermal contraction effects. This property of the resonator was an after-thought in the current design, and hasn't been fully perfected. With very small thermal contraction, systematic errors in measurement can be reduced.

The current apparatus has not been used at liquid helium temperatures, due to the unsuitability of the current sample gantry. Such measurements are not expected to be done very often, since the high temperature (70–90 K) properties are most important for applications of films. Studies of fundamental properties, however, will require a greater temperature range than currently used. The use of a conventional superconducting spherical mirror could increase the sensitivity of measurements made at all temperatures (at 4.2 K and 117 GHz, the surface resistance of Nb is about 0.001Ω , while for copper it is 0.04Ω) [64]. The flow cryostat will never be as efficient as a standard cryostat, though improvements to the current design can be made (chiefly in the addition of more radiation shielding). These changes may be made in the interest of using less helium.

Since the new network analyzer will be capable of working over a number of modes of the resonator, a study of the frequency dependence of R_S will be possible. Such a study can probe how well the prediction of $R_S \propto \omega^2$ holds, as predicted by the simple two-fluid model. As well, a device to allow the study of the spatial dependence surface resistance of large area films at 77K can be constructed. A simple version of this was built previously, but suffered from instability due to temperature drifts. This will allow the routine measurement of the homogeneity of large-area films, which is required for many applications such as microwave filters.

It is hoped that studies of fundamental properties of superconductors will be possible with the new millimeter-wave network analyzer. Since higher frequencies and greater resolution will be possible, a goal of measuring single crystals is feasible. Currently single crystals of $\text{YBa}_2\text{Cu}_3\text{O}_{7-\delta}$ are too small for measurement, but the limitation due to the spot size approaching the wavelength of the radiation becomes more forgiving at higher frequencies. Comparison of the behaviour of single crystals of $\text{YBa}_2\text{Cu}_3\text{O}_{7-\delta}$, and other materials, with films is important work for both practical, as well as fundamental reasons. The effect of defects on the electromagnetic properties of these materials gives insight into the still-unknown mechanism for the superconductivity. Defects are currently suspected to give the electromagnetic properties of thin films their strikingly different behaviour from single crystals. Investigation of these differences could aid in improving the films for practical purposes.

There are a number of materials which currently show the promise of becoming useful for microwave work, though most work has focussed in the past on $\text{YBa}_2\text{Cu}_3\text{O}_{7-\delta}$. Studies of the mercury, thalium and bismuth copper oxides will help in the development of these for commercial purposes, as well as in the understanding of the whole family of high temperature cuprate superconductors. These materials will require the same systematic study as has been done in $\text{YBa}_2\text{Cu}_3\text{O}_{7-\delta}$ both for optimization, as well as to determine

any similarities and differences in their properties.

Bibliography

- [1] J. G. Bednorz and K. A. Muller. *Z. Phys.*, B64, 1986.
- [2] H. Kamerlingh Onnes. *Leiden Comm.*, (120b, 122b, 124c), 1911.
- [3] J. Bardeen, L. N. Cooper, and J. R. Schrieffer. *Physical Review*, 108, 1957.
- [4] Ruixing Liang, P. Dosanjh, D. A. Bonn, D. J. Baar, J. F. Carolan, and W. N. Hardy. *Physica C*, 195, 1992.
- [5] Gloria B. Lubkin. Applications of high-temperature superconductors approach the marketplace. *Physics Today*, March 1995.
- [6] N. Klein. Electrodynamic properties of high temperature superconductor films. In J. J. Pouch, S. A. Alterowitz, and R. R. Romanofsky, editors, *Synthesis and Characterization of High-Temperature Superconductors*, volume 130-132. Materials Science Forum, 1993.
- [7] Simon Ramo, John R. Whinnery, and Theodore Van Duzer. *Field and Waves in Communication Electronics*. John Wiley and Sons, New York, 1965.
- [8] O. M. Bucci and B. Di Massa. Open resonators powered by a rectangular waveguide. *IEE Proceedings H*, 139(4):323–329, August 1992.
- [9] Michael Tinkham. *Introduction to Superconductivity*. McGraw-Hill, New York, 1975.
- [10] J. R. Waldram. The surface impedance of superconductors. *Advances in Physics*, 13(49), 1964.
- [11] J. Halbritter. On surface resistance of superconductors. *Z. Phys.*, 266:209–217, 1974.
- [12] D. C. Mattis and J. Bardeen. Theory of the anomalous skin effect in normal and superconducting metals. *Physical Review*, 111(2), July 1958.
- [13] J. P. Turneaure, J. Halbritter, and H. A. Schwettman. The surface impedance of superconductors and normal conductors: the Mattis-Bardeen theory. *Journal of Superconductivity*, 4(5):342, 1991.

- [14] D. A. Bonn, Ruixing Liang, T. M. Riseman, D. J. Baar, D. C. Morgan, Kuan Zhang, P. Dosanjh, T. L. Duty, A. MacFarlane, G. D. Morris, J. H. Brewer, W. N. Hardy, C. Kallin, and A. J. Berlinsky. Microwave determination of the quasiparticle scattering time in $\text{YBa}_2\text{Cu}_3\text{O}_{6.95}$. *Physical Review B*, 47, 1993.
- [15] W. N. Hardy, D. A. Bonn, D. C. Morgan, R. Liang, and K. Zhang. *Physical Review Letters*, 70:3999, 1993.
- [16] C. J. Gorter and H. B. G. Casimir. *Phys. Z.*, 35, 1934.
- [17] H. London. *Nature*, 133:497, 1934.
- [18] Kuan Zhang. *Studies of the Microwave Surface Resistance of Pure, Zinc and Nickel Doped YBCO single crystals*. PhD thesis, University of British Columbia, 1995.
- [19] T. Kuhlemann and J. H. Hinken. Measurement of the surface resistance R_S of structured Y-Ba-Cu-O films on different substrates in the lower gigahertz range. *Superconductor Science and Technology*, 5:37–40, 1992.
- [20] S. Kamal, D. A. Bonn, N. Goldenfeld, R. Liang, and W. N. Hardy. Penetration depth measurements of 3D XY critical behavior in $\text{YBa}_2\text{Cu}_3\text{O}_{6.95}$. *Physical Review Letters*, 73(13):1845–1848, September 1994.
- [21] N. McN. Alford, T.W. Button, M. J. Adams, S. Hedges, B. Nicholson, and W. A. Phillips. Low surface resistance in $\text{YBa}_2\text{Cu}_3\text{O}_x$ melt-processed thick films. *Nature*, 349, February 1991.
- [22] S. Sridhar. Microwave response of thin-film superconductors. *Journal of Applied Physics*, 63(1):159–166, 1988.
- [23] R. C. Taber. A parallel plate resonator technique for microwave loss measurements on superconductors. *Reviews of Scientific Instruments*, 61(8):2200, August 1990.
- [24] O. Llopis and J. Graffeuil. Microwave characterization of high T_C superconductors with a dielectric resonator. *Journal of the Less-Common Metals*, 164 and 165:1248–1251, 1990.
- [25] C. J. Edgcombe. Measurement of surface resistance of high- T_C superconductor by use of dielectric resonator. *Electronics Letters*, 27(10), May 1991.
- [26] J. S. Martens, V. M. Hietela, D. S. Ginley, T. E. Zipperian, and G. K. G. Hohenwarter. Confocal resonators for measuring the surface resistance of high-temperature superconducting films. *Applied Physics Letters*, 58(22):2543–2545, June 1991.

- [27] Bao Jia-shan, Zhou Shi-ping, Wu Ke-qing, Lou Wei-gen, Ding Ai-lei, and Wang Shu-hong. Microwave properties of highly oriented $\text{YBa}_2\text{Cu}_3\text{O}_{7-\delta}$ superconducting thin films. *Journal of Superconductivity*, 4(4), 1991.
- [28] W. L. Holstein, L. A. Parisi, Z.-Y. Shen, C. Wilker, M. S. Brenner, and J. S. Martens. Surface resistance of large-area $\text{Tl}_2\text{Ba}_2\text{CaCu}_2\text{O}_8$ thin films at microwave and millimeter wave frequencies measured by three noncavity techniques. *Journal of Superconductivity*, 6(3):191–200, 1993.
- [29] Conductus, Inc. 969 West Maude Avenue, Sunnyvale Ca 94086.
- [30] *The Microwave Engineers' Handbook and Buyers' Guide*. Horizon House Inc., 1964.
- [31] *Low Temperature Techniques*. Materials Science Center, Cornell University, Ithaca, New York, Spring 1981.
- [32] Russell B. Scott. *Cryogenic Engineering*. D. Van Nostrand Company, Inc., Princeton New Jersey.
- [33] F. E. Hoare, L. C. Jackson, and N. Kurti. *Experimental Cryophysics*. Butterworths, London, 1961.
- [34] Octave Levenspiel. *Engineering Flow and Heat Exchange*. Plenum Press, New York, 1984.
- [35] Guy Kendall White. *Experimental Techniques in Low-Temperature Physics*. Clarendon Press, Oxford.
- [36] W. H. Press, B. P. Flannery, S. A. Teukolsky, and W. T. Vetterling. *Numerical Recipes in C, The art of Scientific Computing*. Cambridge University Press, 1989.
- [37] A. G. Fox and Tingye Li. Resonant modes in a maser interferometer. *Bell System Technical Journal*, 40, 1961.
- [38] G. Goubau and F. Schwing. On the guided propagation of electromagnetic wave beams. *IRE Transactions on Antennas and Propagation*, pages 248–256, May 1961.
- [39] G. D. Boyd and J. P. Gordon. Confocal multimode resonator for millimeter through optical wavelength masers. *Bell System Technical Journal*, pages 489–508, March 1961.
- [40] H. Kogelnik and T. Li. Laser Beams and Resonators. *Proceedings of the IEEE*, 54(10), October 1966.
- [41] K. Kurokawa. *An Introduction to the Theory of Microwave Circuits*. Academic Press, 1969.

- [42] A. L. Cullen, P. Nagenthiram, and A. D. Williams. A variational approach to the theory of the open resonator. *Proceedings of the Royal Society of London, A.*, 329:153–169, 1972.
- [43] A. L. Cullen and P. K. Yu. Complex source-point theory of the electromagnetic open resonator. *Proceedings of the Royal Society of London, A.*, 366:155–171, 1979.
- [44] A. L. Cullen. *Millimeter-Wave Open-Resonator Techniques*, volume 10, pages 233–280. Academic Press Inc., 1983.
- [45] P. M. Morse and H. Feshbach. *Methods of Theoretical Physics*, volume 1. McGraw-Hill, 1953.
- [46] L. A. Weinstein. *Open Resonators and Open Waveguides*. The Golem Press, 1969.
- [47] R. K. Mongia and R. K. Arora. Equivalent circuit parameters of an aperture coupled open resonator cavity. *IEEE Transactions on Microwave Theory and Techniques*, 41(8):1245–1250, August 1993.
- [48] C. W. Erickson. High order modes in a spherical Fabry-Perot resonator. *IEEE Transactions on Microwave Theory and Techniques*, MTT-23:208, 1975.
- [49] Ichiro Shinkoda. *Studies of Spin-Polarized Hydrogen and Deuterium at Temperatures Below 1 K using E.S.R.* PhD thesis, University of British Columbia, July 1990.
- [50] E. L. Ginzton. *Microwave Measurements*. McGraw-Hill, New York, 1957.
- [51] G. L. Ragan. *Microwave Transmission Circuits*, volume 9 of *M.I.T. Radiation Laboratory Series*. McGraw-Hill, 1948.
- [52] H. Abe and K. Koga. *Japanese Journal of Applied Physics*, 13:1145, 1974.
- [53] C. G. Montgomery, R. H. Dicke, and E. M. Purcell. *Principles of Microwave Circuits*, volume 8 of *M.I.T. Radiation Laboratory Series*. Dover Publications Inc., New York, 1965.
- [54] G. E. H. Reuter and E. H. Sondheimer. The theory of the anomalous skin effect in metals. *Proceedings of the Royal Society of London, A.*, 195:336, 1948.
- [55] R. B. Dingle. The anomalous skin effect and the reflectivity of metals I. *Physica*, XIX:311–347, 1953.
- [56] R. B. Dingle. The anomalous skin effect and the reflectivity of metals II. *Physica*, XIX:348–364, 1953.

- [57] L. A. Hall. *Survey of Electrical Resistivity on 16 Pure Metals in the Temperature Range 0 to 273 K*. N.B.S. Technical Note 365, February 1968.
- [58] Levi Waldron and Pinder Dosanjh. Private communication.
- [59] W. J. McG. Tegart. *The Electrolytic and Chemical Polishing of Metals in research and industry*. Pergamon Press, London, 1959.
- [60] P. V. Shigolev. *Electrolytic and Chemical Polishing of Metals*. Freund Publishing House, Tel Aviv Israel, 1974.
- [61] Q. Y. Ma, P. Dosanjh, J. F. Carolan, and W. N. Hardy. Inhibition of superconductivity in Y-Ba-Cu-O films by Si ion implantation. *Applied Physics Letters*, 63(26):3633–3635, 1993.
- [62] N. Klein, H. Chaloupka, G. Müller, S. Orbach, H. Piel, B. Roas, L. Schultz, U. Klein, and M. Peiniger. The effective microwave surface impedance of high- T_C thin films. *Journal of Applied Physics*, 67(11):6940–6945, June 1990.
- [63] D.A. Bonn, S. Kamal, Kuan Zhang, Ruixing Liang, D. J. Baar, E. Klein, and W. N. Hardy. A comparison of the influence of Ni and Zn impurities on the electromagnetic properties of $\text{YBa}_2\text{Cu}_3\text{O}_{6.95}$.
- [64] H. Piel and G. Muller. The microwave surface impedance of high- T_C superconductors. *IEEE Transactions on Magnetics*, 27(2), March 1991.